UNIVERSITY OF CALIFORNIA SAN DIEGO

ENERGETICS OF SURFACE MELT IN WEST ANTARCTICA

A thesis submitted in partial satisfaction of the
requirements for the degree Master of Science

in

Earth Sciences

by

Madison Ghiz

Committee in charge:

Dan Lubin, Chair
Helen Amanda Fricker
Joel Norris

2020

The thesis of Madison Ghiz is approved, and it is acceptable in quality and form for publication on microfilm and electronically:

_____

_____

_____

Chair

University of California San Diego

2020

TABLE OF CONTENTS

Signature Page iii

Table of Contents iv

List of Figures vi

Acknowledgements ix

Abstract of Thesis x

Chapter 1 Introduction and Background 1
1.1 Sea Level Rise 1
1.2 West Antarctic Ice Sheet Loss 2
1.3 Surface Melting in Antarctica 3
1.4 Physics of Surface Melt 4
1.5 Recent Observations of Surface Melting 5
1.6 Scientific Questions for this Study 9
1.7 Study Locations 11
1.7.1 Siple Dome 12
1.7.2 Pine Island and Thwaites Glaciers 13
1.7.3 Ross Ice Shelf 15
1.7.4 Larsen C Ice Shelf 16

Chapter 2 Data and Methods 18
2.1 Data 18
2.1.1 Passive Microwave Brightness Temperature 18
2.1.2 Satellite SW + LW Spectral Measurements 19
2.1.3 Meteorological Reanalysis Data 20
2.1.4 Radiative and Surface Observations from AWARE 20
2.2 Methods 20
2.2.1 Passive Microwave Brightness Temperature Time Series 21
2.2.2 Using AWARE Measurements to Analyze Accuracy of Reanalysis and Satellite Data 22
2.2.3 Radiative and Cloud Property Time Series from Reanalysis and Satellite Data 27

Chapter 3 Results 28
3.1 Meteorological Synopses 28
3.1.1 January 2016 28
3.1.2 January 2015 29
3.1.3 February 2013 31
3.1.5 January 2012 33
3.1.5 December 2011 35

3.2 Siple Dome 37
3.2.1 January 2016 37
3.2.2 January 2015 41
3.2.3 December 2011 45
3.3 Pine Island and Thwaites Glaciers 49
3.3.1 December 2011 49
3.3.2 January 2012 53
3.3.3 February 2013 57
3.4 Ross Ice Shelf 61
3.4.1 December 2011 61
3.5 Larsen C Ice Shelf 67
3.5.1 December 2000 67

Chapter 4 Discussion 73
4.1 Thermal Blanketing from Optically Thick Clouds 73
4.2 Thin, Low-Level Liquid Clouds 74
4.3 Surface Melt Preconditioning from Sensible Heat Flux 75
4.4 Föhn Winds 76

Chapter 5 Conclusion 78

Bibliography 81

LIST OF FIGURES

Figure 1.1: Ice shelf and ice sheet dynamics diagram 3
Figure 1.2: Map of West Antarctica with study locations identified 11
Figure 1.3: Map of Siple Dome region with the AWS. 13
Figure 1.4: Map of Pine Island Glacier and Thwaites Glacier region with the AWS 14
Figure 1.5: Map of Ross Ice Shelf with the AWSs 15
Figure 1.6: Map of the Larsen C Ice Shelf with the AWS 16
Figure 2.1: Skin temperature and radiation measurements from AWARE campaign compared with ERA5 reanalysis model for the month of January 2016 . 22
Figure 2.2: Skin temperature and radiation measurements from AWARE campaign compared with CERES SYN1deg satellite data for the month of January 2016 23
Figure 2.3: Hourly surface radiation components spatially averaged over Siple Dome during January 2016: (a) individual net surface radiation terms from ERA5 and CERES, (b) total surface radiation from ERA5 and CERES, (c) shows the total ME using entirely ERA5 fluxes and using CERES for the radiation while retaining ERA5 for turbulent fluxes 25
Figure 3.1: 700 mb Geopotential Height synoptic weather map spanning 4 – 8 January 2015 29
Figure 3.2: 700 mb Geopotential Height synoptic weather map spanning 18 – 23 February 2013 31
Figure 3.3: 700 mb Geopotential Height synoptic weather map spanning 3 – 7 January 2012 33
Figure 3.4: 700 mb Geopotential Height synoptic weather map spanning 18 – 24 December 2011 35
Figure 3.5: Box-and-whisker plot of 19 GHz-H brightness temperature over the Siple Dome region in January 2016 36
Figure 3.6: Surface emissivity calculated using ERA5 skin temperature for several individual grid cells corresponding to various individual brightness temperature percentiles for Siple Dome January 2016 38
Figure 3.7: CERES retrievals and ERA5 model estimates of cloud liquid water path (a) and cloud ice water path (b) over Siple Dome in January 2016 38
Figure 3.8: Spatially averaged time series of surface energy budget components and total melt energy for Siple Dome in January 2016 39
Figure 3.9: Box-and-whisker plot of 19 GHz-H brightness temperature over the Siple Dome region in January 2015 40
Figure 3.10: Surface emissivity calculated using ERA5 skin temperature for several individual grid cells corresponding to various individual brightness temperature percentiles for Siple Dome January 2015 42
Figure 3.11: CERES retrievals and ERA5 model estimates of cloud liquid water path (a) and cloud ice water path (b) over Siple Dome in January 2015 42
Figure 3.12: Spatially averaged time series of surface energy budget components and total melt energy for Siple Dome in January 2015 43
Figure 3.13: Box-and-whisker plot of 19 GHz-H brightness temperature over the Siple Dome region in December 2011 44

Figure 3.14: Surface emissivity calculated using ERA5 skin temperature for several individual grid cells corresponding to various individual brightness temperature percentiles for Siple Dome December 2011 46
Figure 3.15: CERES retrievals and ERA5 model estimates of cloud liquid water path (a) and cloud ice water path (b) over Siple Dome in December 2011 . . . 46
Figure 3.16: Spatially averaged time series of surface energy budget components and total melt energy for Siple Dome in December 2011 47
Figure 3.17: Box-and-whisker plot of 19 GHz-H brightness temperature over the Pine Island Glacier and Thwaites Glacier region in December 2011 . . . 48
Figure 3.18: Surface emissivity calculated using ERA5 skin temperature for several individual grid cells corresponding to various individual brightness temperature percentiles for Pine Island and Thwaites Glaciers in December 2011 50
Figure 3.19: CERES retrievals and ERA5 model estimates of cloud liquid water path (a) and cloud ice water path (b) over Pine Island Glacier and Thwaites Glacier in January 2012 50
Figure 3.20: Spatially averaged time series of surface energy budget components and total melt energy for Pine Island Glacier and Thwaites Glacier in December 2011 51
Figure 3.21: Box-and-whisker plot of 19 GHz-H brightness temperature over the Pine Island Glacier and Thwaites Glacier region in January 2012. 52
Figure 3.22: Surface emissivity calculated using ERA5 skin temperature for several individual grid cells corresponding to various individual brightness temperature percentiles for Pine Island and Thwaites Glaciers in January 2012 54
Figure 3.23: CERES retrievals and ERA5 model estimates of cloud liquid water path (a) and cloud ice water path (b) over Pine Island Glacier and Thwaites Glacier in January 2012 54
Figure 3.24: Spatially averaged time series of surface energy budget components and total melt energy for Pine Island Glacier and Thwaites Glacier in January 2012 55
Figure 3.25: Box-and-whisker plot of 19 GHz-H brightness temperature over the Pine Island Glacier and Thwaites Glacier region in February 2013 56
Figure 3.26: Surface emissivity calculated using ERA5 skin temperature for several individual grid cells corresponding to various individual brightness temperature percentiles for Pine Island and Thwaites Glaciers in February 2013 58
Figure 3.27: CERES retrievals and ERA5 model estimates of cloud liquid water path (a) and cloud ice water path (b) over Pine Island Glacier and Thwaites Glacier in February 2013 58
Figure 3.28: Spatially averaged time series of surface energy budget components and total melt energy for Pine Island Glacier and Thwaites Glacier in February 2013 59
Figure 3.29: Box-and-whisker plot of 19 GHz-H brightness temperature over the Ross Ice Shelf region in December 2011 60
Figure 3.30: Surface emissivity calculated using ERA5 skin temperature for several

individual grid cells corresponding to various individual brightness temperature percentiles for the Ross Ice Shelf in December 2011 62
Figure 3.31: Surface wind speed (a), surface wind direction (b), 850 hPa wind speed (c), and 850 hPa wind direction (d) over the Ross Ice Shelf in December 2011 62
Figure 3.32: Spatially averaged time series of surface energy budget components and total melt energy for the Ross Ice Shelf in December 2011. 63
Figure 3.33: CERES retrievals and ERA5 model estimates of cloud liquid water path (a) and cloud ice water path (b) over the Ross Ice Shelf in December 2011 64
Figure 3.34: Sabrina AWS measurements of 2 m temperature (a), wind speed (b), and wind direction (c) for December 2011 64
Figure 3.35: Tom AWS measurements of 2 m temperature (a), wind speed (b), and wind direction (c) for December 2011 65
Figure 3.36: Box-and-whisker plot of 19 GHz-H brightness temperature over the Larsen C Ice Shelf region in December 2000 66
Figure 3.37: Heat map of brightness temperature on the Larsen C Ice Shelf from 16 December to 20 December 2000 68
Figure 3.38: Surface emissivity calculated using ERA5 skin temperature for several individual grid cells corresponding to various individual brightness temperature percentiles for the Larsen C Ice Shelf in December 2000 . . 69
Figure 3.39: Surface wind speed (a), surface wind direction (b), 850 hPa wind speed (c), and 850 hPa wind direction (d) over the Larsen C Ice Shelf in December 2000. 69
Figure 3.40: Spatially averaged time series of surface energy budget components and total melt energy for the Larsen C Ice Shelf in December 2000 70
Figure 3.41: CERES retrievals and ERA5 model estimates of cloud liquid water path (a) and cloud ice water path (b) over the Larsen C Ice Shelf in December 2000 71
Figure 3.42: AWS-14 measurements of 2 m temperature (a), wind speed (b), and wind direction (c) for December 2000. 71

ACKNOWLEDGEMENTS

I would first like to acknowledge my advisor, Dan Lubin, for his guidance, mentorship, and patience. Dan provided me with the opportunity of a lifetime to work on this kind of research in the field at Siple Dome, Antarctica, and I cannot thank him enough for this. I would also like to thank my thesis committee members, Helen Amanda Fricker and Joel Norris, for their time put into this thesis and for all of the helpful feedback. Thank you to Ryan Scott for helping with any questions I had along the way, as well as his contributions to the meteorological analyses in this paper. Also, thank you to Andy Vogelmann from Brookhaven National Laboratory for providing the AWARE data files used for analysis and in several of the figures. Lastly, I would like to thank my family, friends, and the Scripps community for the constant support and motivation.

ABSTRACT OF THESIS

ENERGETICS OF SURFACE MELT IN WEST ANTARCTICA

by

Madison Ghiz

Master of Science in Earth Sciences

University of California San Diego, 2020

Dr. Dan Lubin, Chair

Surface melting is an important mass loss process from ice sheets. In West Antarctica, the lack of direct surface observations poses difficulties in studying surface melt and loss of ice mass. This thesis presents seven contrasting cases in which surface melt was detected by satellite passive microwave sensors and analyzed using both reanalysis data and satellite data. During these melt events meteorological conditions caused the total melt energy to elevate for anywhere between 3 – 8 days, compared with the rest of the month. This elevated melt energy can be induced by four main mechanisms typical of the austral summer climate described in this study.

These mechanisms are thermal blanketing from optically thick clouds; thin clouds enhancing all-wave radiation at the surface; sensible heat flux preconditioning the surface to melt; and föhn wind presence on the lee side of mountains. The study locations are Siple Dome, Pine Island and Thwaites Glaciers, the southern portion of the Ross Ice Shelf, and the Larsen C Ice Shelf. Through assessing the surface energy budget, total melt energy, temperature and wind components, and cloud microphysics with regards to both 25-km resolution and small-scale spatial variability, the importance of using the highest resolution data available is demonstrated. This study not only defines drivers of West Antarctic melt, but identifies improvements that could be made to the methods and data sets used to quantify the climatology of surface melt.

Chapter 1

Introduction and Background

1.1 Sea Level Rise

To properly predict sea level rise, ice sheet mass loss processes must be quantified and understood. Addition of ice mass into the global oceans from Greenland and Antarctica is a significant contributor to sea level rise. The major Southern Hemisphere contributor to these changes comes from the West Antarctic Ice Sheet (WAIS), a critical region prone to accelerated mass loss from ocean-driven melting. Although surface melting in Antarctica currently does not contribute directly in sea level rise, its occurrence is increasing with trends of a warming atmosphere and poses concerns about rapid ice retreat scenarios following hydrofracturing events [DeConto and Pollard, 2016]. About half of ice loss in Antarctica is a result of iceberg calving [Smith et al., 2020]; a process which can be influenced by surface melt triggering hydrofracturing of the ice shelf. Hydrofracturing has the potential to disrupt the stability of the ice sheet by causing mass disintegration of the ice shelf which acts as a restraining force for grounded ice flow seaward. Though melting of the floating ice shelves has a marginal impact on sea level rise, this decrease in stability and consequent loss of these buttressing ice shelves affects the mass balance of the ice sheet and can alter the speed at which the grounded ice accelerates seaward [Hogg and Gudmundsson, 2017]. It is vital to improve the understanding of what is driving these mass surface melt events to fully comprehend ice sheet and ice shelf

dynamics, and therefore accurately predict and moderate the impact of future ice loss and global sea level rise.

1.2 West Antarctic Ice Sheet Loss

Approximately 75% of Antarctica's coastline is occupied by ice shelves [Rignot et al., 2013]. Increasing discharge of ice mass into the ocean is a result of internal, atmospheric, and oceanic mechanisms acting on the ice shelves and causing them to thin. Ice shelves are extensions of the ice sheets floating on the ocean's surface that reinforce the position of grounded ice and prevent its acceleration seaward. These ice shelves create a buttressing effect and stabilize the position of the grounded ice sheet. Buttressing potential from the ice shelves can be defined as the sum of vertical hydrostatic pressure from the ocean and horizontal force from the ice shelf on the upstream grounded ice [Thomas et al., 1979; Dupont et al., 2005]. This restraining force can be compromised as Circumpolar Deep Water (CDW) begins to infiltrate ocean cavities beneath the ice. This intrusion of CDW results in enhanced basal melting that causes the ice shelves to thin. Not only is CDW experiencing increases in temperature and salinity, but it is being increasingly pushed under ice shelves by strengthening polar westerly currents and lack of sea ice [Nakayama et al., 2018]. These progressions ultimately weaken the ice shelves and cause the grounding lines, the boundary between floating ice shelves and grounded ice, to thin and retreat.

The position of the grounding line influences the likelihood of marine ice sheet instability, which is largely a result of retrograde slopes as seen around the WAIS. Grounding line retreat along these retrograde slopes often results in accelerated ice flow because of the

strong dependency of ice flux increasing with increasing grounding line depth [Pollard et al., 2015]. This occurrence of instability could be worsened by increased surface melt percolating through crevasses, causing hydrofracturing and augmented ice sheet calving [Scambos et al., 2017], and ultimately the loss of ice shelves that buttress the ice sheets. The stability of the entire Antarctic Ice Sheet relies on the mass balance of these ice shelves, whose equilibrium is maintained by accumulating snowfall and ice flow from inland glaciers and surface melting that drives calving and ice-shelf collapse [Rignot et al., 2013]. This fragile balance is being increasingly skewed toward a greater amount of mass loss than mass gained [Paolo et al., 2015; Smith et al. 2020]. Accurate assessment of surface melt volume on the WAIS will be key to understanding ice shelf dynamics and thus overall mass ice loss on the continent.

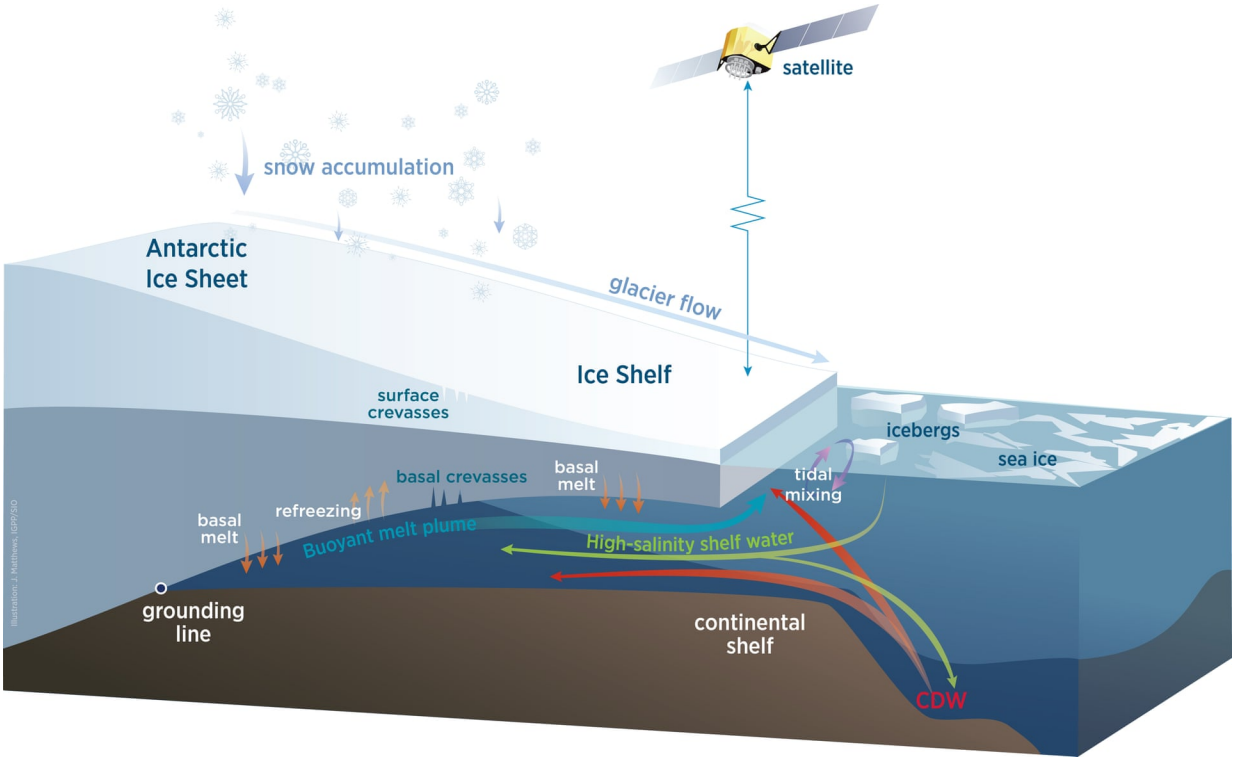

Figure 1: Ice shelf and ice sheet dynamics and interactions with oceanic, atmospheric, and internal mechanisms from Jennifer Matthews, SIO.

1.3 Surface Melting in Antarctica

Recent ice shelf collapses have been attributed to surface melt induced by warming air temperatures [e.g., Scambos et al., 2003; van den Broeke et al., 2005]. Ice shelf calving due to hydrofracturing by surface melt percolating into crevasses has been predicted to increase as shown in climate models simulating warm-climate scenarios [Pollard et al., 2015]. The disintegration of the Larsen B Ice Shelf was largely a result of mass surface pooling and surface melt resulting in the hydrofracturing of the ice shelf [Scambos et al., 2004]. Such ice shelf collapse events can lead to acceleration of tributary glaciers and grounded ice into the oceans [Scambos et al., 2004; Rignot et al., 2004]. Although surface melting is often observed on floating ice shelves [Phillips et al., 1998; Banwell et al., 2013; Kingslake et al., 2017], it can have an impact on grounded ice by triggering hydrofracturing and deepening crevasses close to the grounding line and thus weakening the ice column [Pollard et al., 2015]. As surface melt rates follow the trends of the warming atmosphere, meltwater drainage will begin to occur at a faster rate [Kingslake et al., 2017]. Studies of surface melt are essential in understanding how a warming atmosphere will impact processes such as hydrofracturing and calving of ice shelves, thus contributing to sea level rise.

1.4 Physics of Surface Melt

To fully diagnose and comprehend drivers of surface melt, the surface energy balance (SEB) must be evaluated. SEB is the exchange of energy from Earth's surface and the atmosphere, where the key components are shortwave (SW) and longwave (LW) radiation and turbulent surface fluxes. Turbulent flux is the sum of sensible heat flux, the heat generated by

temperature differences in the surface and air, and latent heat flux, the heat exchanged from water changing phase. Over snow and ice the SEB is usually expressed as a melt energy, *ME*:

$$ME = F_{SW}^{\downarrow} - F_{SW}^{\uparrow} + F_{LW}^{\downarrow} - F_{LW}^{\uparrow} + F_{SH} + F_{LH} - G \quad (1)$$

which is the sum of the downwelling and upwelling SW radiation, downwelling and upwelling LW radiation, sensible heat and latent heat fluxes, and a ground conduction term, respectively. In this expression the radiation terms are all positive, and for the turbulent fluxes the European Centre for Medium-Range Weather Forecasts (ECMWF) convention is used where a positive sign denotes energy into the surface [ECMWF-IFC]. *G* is usually very small compared to the radiative and turbulent fluxes [Fisher et al., 2015]. It is often convenient to represent the total radiative contribution to the SEB as a net radiative flux:

$$F_{NR} = F_{SW}^{\downarrow} - F_{SW}^{\uparrow} + F_{LW}^{\downarrow} - F_{LW}^{\uparrow} \quad (2)$$

If the surface temperature falls below freezing, a positive *ME* will cause gradual warming of the surface toward the melting point. A negative *ME* represents a cooling of the surface away from the melting point. If the surface temperature is at or above freezing, a positive *ME* maintains surface melting rate while a negative *ME* reduces the surface melt rate and surface temperature until the surface is below freezing (if negative *ME* is sustained long enough).

1.5 Recent Observations of Surface Melting

To enhance our understanding of surface melt, we can first review studies over Greenland that may offer insight into the response of glaciers and snowmelt in a warming Antarctic climate. Because both Antarctica and Greenland are difficult to access for direct continuous observations, ice cores can be sampled to quantify summer melting by tracing how water percolates through the surface and refreezes in the porous cavities of the firn layer [Graeter et al., 2018; Trusel et al., 2018]. A strong positive correlation between melt rate and volume and increasing surface temperatures based on the study of firn and core samples from central west Greenland was shown by Trusel et al. [2018]. As the surface begins to melt at higher rates and the firn layer temperature rises, glaciers will begin to experience a decrease in albedo due to a greater amount of melt pooling [Humphrey et al., 2012]. This will be followed by a greater amount of mass loss because of the generation of less permeable ice layers, promoting accelerated ice and meltwater across glaciers, consequently aiding to sea level rise [Machguth et al., 2016]. These characteristics of a warming climate's effect on melt onset over Greenland glaciers are transferable to glaciers found in the Antarctic, even if the overall mass loss mechanisms are different.

Additional observations in Greenland show surface melt enhanced and sustained by a cloud radiative effect. Optically thin, low-level liquid water clouds augment the downwelling LW radiation at the surface while simultaneously allowing enough downwelling SW radiation to help raise near-surface air temperatures. This has been demonstrated from surface observations, satellite remote sensing data, and SEB model studies by Bennartz et al. [2013]. Van Tricht et al. [2016] support this result and suggest that the clouds also prevent the meltwater from refreezing since radiative cooling is reduced in cloudy conditions. Nicolas et al. [2017] proposed that all-

wave (SW+LW) radiative enhancement induced by thin, low-level liquid water clouds could be occurring in Antarctica. This thin cloud all-wave radiative enhancement is a potential driver of enhanced surface melt in both polar environments and therefore accurate cloud microphysics must be represented in modern climate and reanalysis models to accurately predict future runoff and eventual sea level impacts.

In February and March of 2002, the Larsen B Ice Shelf, a 3,250 square kilometer section of the ice shelf on the eastern side of the Antarctic Peninsula (AP), collapsed. The rapid disintegration of the Larsen B Ice Shelf provides insight into the future of the Larsen C Ice Shelf (LCIS) as surface melt observations and mean summer surface temperatures continue to rise. It is generally believed that the main driver of ice shelf retreat on the AP is due to rising air temperatures [Scambos et al., 2000; van den Broeke et al., 2005]. This pattern of rising air temperatures is thought to be partly a result of an increase in föhn winds, which are warm, dry air masses that descent on the leeward side of mountains [Cape et al., 2015]. Originating from either the latent heat release as precipitation on the windward side of a mountain range or the radiative heating of sinking air, föhn winds are a phenomenon capable of temporarily raising near-surface air temperatures above freezing in Antarctic summer conditions, initiating or sustaining surface melt [Cape et al., 2015; Elvidge et al., 2016]. In addition to influencing the CDW, strengthening polar westerlies from a positive trend in the Southern Annual Mode (SAM) increase föhn frequency in regions such as the AP mountains just west of the Larsen Ice Shelf [Elvidge et al., 2015; Cape et al., 2015]. This change in westerlies allows a larger volume of air to be pushed over the ridge of the AP, often creating a linear flow regime and thus more targeted direct air on the LCIS. The LCIS can see föhn winds over a large spatial scale (tens of square km), and föhn

wind presence among the Siple Coast and Ross Ice Shelf has also been observed as well [Scott et al., 2019].

Spatial correlation between surface melt and increasing air temperatures on the LCIS are indicative of the occurrence of föhn winds [King et al., 2017]. As melt frequency on the Larsen Ice Shelf decreases from north to south and from west to east, so does air temperatures and föhn wind presence [King et al., 2017]. This reveals higher melting at the base of the AP mountains in the northern regions of the LCIS, indicating the possibility of föhn wind events strongly influencing the surface temperatures. Preceding the Larsen B Ice Shelf collapse, the WAIS experienced meltwater accumulation of extreme excess [van den Broeke, 2015], likely due to the sustained melt period from experiencing abnormally high air temperatures [Scambos et al., 2004]. In the days leading up to the collapse, the flexural stress on the ice shelf caused widespread fracturing, leading to mass drainage of these supraglacial lakes and ultimately to the disintegration of the Larsen B Ice Shelf [Scambos et al., 2000; Banwell et al., 2013].

In addition to the mass unloading of meltwater prior to the collapse, glaciers were observed to rapidly increase in outflow speed as shown by interferometric synthetic-aperture radar data [Rignot et al., 2004, Scambos et al., 2004]. This can be largely attributed to the loss of reinforcing ice shelves following the collapse. Although less direct observations were made during the collapse of the smaller Larsen A Ice Shelf in January 2005, Rott et al. [2002] showed that the Drygalski Glacier began accelerating just after this ice shelf loss [Rignot et al., 2004]. Glacier acceleration after the dissolution of both Larsen A and Larsen B ice shelves illustrates how sensitive a region the Larsen Ice Shelf is. The LCIS is approximately 44,200 km^2, roughly 9 times greater in size than both the Larsen A and Larsen B ice shelves combined. Given the ice

volume contained in the Larsen C Ice Shelf, the impacts from its dissolution and its subsequent advancement of glacial movement would be significant.

West Antarctica is subject to seasonal changes and interannual variability in regional atmospheric circulation [Bromwich et al., 2012; Ding et al., 2013]. The Atmospheric Radiation Measurement West Antarctic Radiation Experiment (AWARE) field campaign was taking place at WAIS Divide in January 2016 when a mass surface melt event occurred, which provided unique insight to prolonged West Antarctic surface melt influenced by the presence of a strong El Niño and a positive SAM [Nicolas et al., 2017]. Seasons experiencing a strong El Niño event often bring prolonged periods of warm, moist air advection to the WAIS [Bromwich et al., 2004; Scott et al., 2019],and one such warm and moist air intrusion was observed during the AWARE campaign. This occurrence can drive up surface temperatures, initiating and extending surface melt events. In a region where direct surface observations are scarce, AWARE was able to report on meteorological and surface conditions during the melt event. Both surface and NASA satellite observations confirmed the presence of optically thick, low-lying liquid water clouds [Scott and Lubin, 2016; Scott et al., 2019], known to increase downwelling LW radiation at the surface, therefore increasing the extent and timeline of melt [Nicolas et al., 2017]. This campaign contributed to the crucial need to understand how West Antarctica's melt season will be influenced by a changing climate whose El Niño seasons are predicted to increase in number and severity [Cai et al., 2014; Paolo et al., 2018]. The AWARE data allow us to analyze the accuracy of the datasets used in this study by comparing them with direct ground observations on an ice sheet surface, and also give us insight into the suitability of these types of data to understand and interpret the observed event.

1.6 Scientific Questions for This Study

The January 2016 melt event recorded by AWARE was unusually large and was driven by a warm, moist air mass descending upon the Ross Ice Shelf and deep into West Antarctica [Nicolas et al., 2017]. The January 2016 melt event can be described as a canonical example of an "atmospheric river" [Wille et al., 2019]. The direct ground observations from the AWARE campaign provided an opportunity to the datasets used in this thesis, highlighting discrepancies within the various types of data and regions where they could be improved. Many West Antarctic coastal regions, including Thwaites and Pine Island Glaciers which are both highly relevant to sea level rise considerations [Christianson et al., 2016; Hoffman et al., 2019], see many days of surface melt nearly every summer. The objective of this study is to assess the energetics of Antarctic surface melt under more typical climatological conditions than occurred during mid-January 2016 over the WAIS. We will evaluate the magnitude and timing of the related energy fluxes by examining seven case studies involving short episodes of surface melt (1 to 5 day duration), at four distinct locations of the WAIS. The observations include (i) satellite passive microwave data for surface properties and melt detection, (ii) satellite SW and LW spectral measurements for retrieving cloud properties and surface radiative fluxes, and (iii) meteorological reanalysis data as the primary source of flux terms in the above expression for *ME*. Most of the locations chosen for this study also have at least one automatic weather station [AWS; Lazzara et al., 2012] to provide a baseline time series to compare against the satellite and reanalysis data.

Our scientific questions:

(1) What meteorological conditions change the *ME* variability to create a surface susceptible to melting?

(2) At surface temperatures just below freezing, is there observational evidence of preconditioning the surface toward eventual melting?

(3) What is the role of horizontal inhomogeneity of surface properties in melt detection over an area comparable to an ice shelf?

(4) Does the thin cloud all-wave radiative effect discovered in Greenland [Bennartz et al., 2013; Van Tricht et al., 2016] occur over the WAIS, or is the WAIS surface melt under a greater influence from warm air advection with optically thick clouds?

(5) Can we identify and diagnose a föhn wind melting case using equation (1) for *ME*?

We first examine the AWARE January 2016 case at WAIS Divide with satellite and reanalysis data to better understand the strengths and limitations of these datasets. We then apply these datasets to seven other 1-5 day duration melt events from four locations across the WAIS: (i) Siple Dome, a WAIS site at lower elevation than WAIS Divide, to evaluate first the January 2016 melt event and then two smaller melt events from different years; (ii) Pine Island and Thwaites Glaciers, located in the Amundsen Sea region of the WAIS, a region currently contributing significantly to overall WAIS mass loss and sea level rise; (iii) a sector of the Ross Ice Shelf near the Transantarctic Mountains, and (iv) the LCIS, where föhn winds might play a role in driving and augmenting surface melt.

1.7 Study Locations

For each case study, we selected a region of approximately 15,000 km^2 (45,000 km^2 for the LCIS) for the acquisition and analysis of atmospheric reanalysis and satellite data sets. Each region contained at least one AWS for additional corroboration of surface observations.

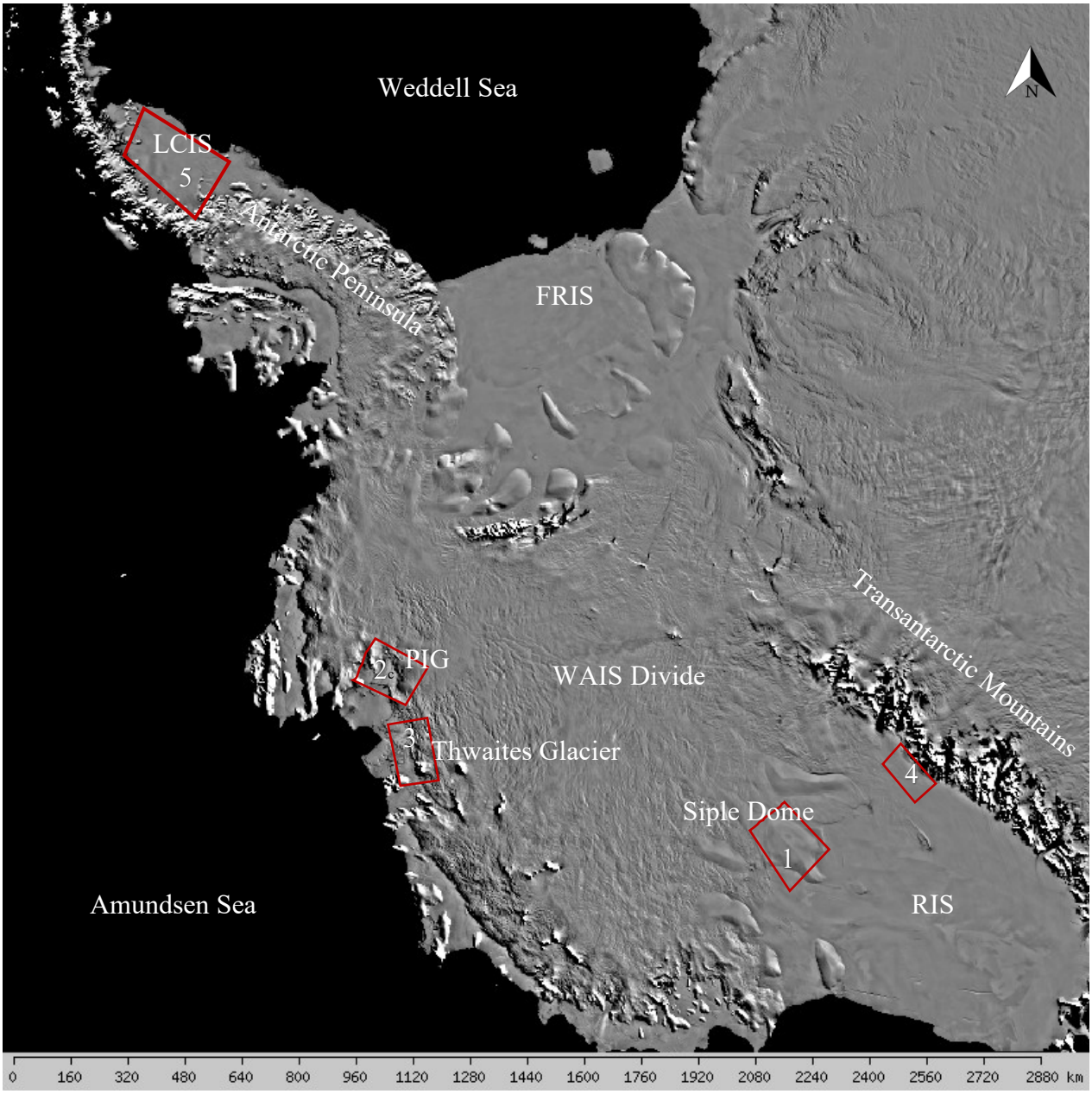

Figure 1.2: Map of West Antarctica. The red boxes indicate the bounds for each region: (1) Siple Dome; (2) Pine Island Glacier; (3) Thwaites Glacier; (4) Ross Ice Shelf; (5) Larsen C Ice Shelf. Background is the MODIS Mosaic of Antarctica [MOA; Scambos et al., 2007].

1.7.1 Siple Dome

Siple Dome lies in the middle of the Siple Coast on the eastern coast of the Ross Ice Shelf, WAIS. The region of interest for this study is bounded by latitude 81° S and 82.5° S, and longitude 144.914° W and 155° W (Figure 1.3). Maximum terrain elevation is approximately 670 m above sea level. Siple Dome AWS has a location of 81.653° S, 149° W.

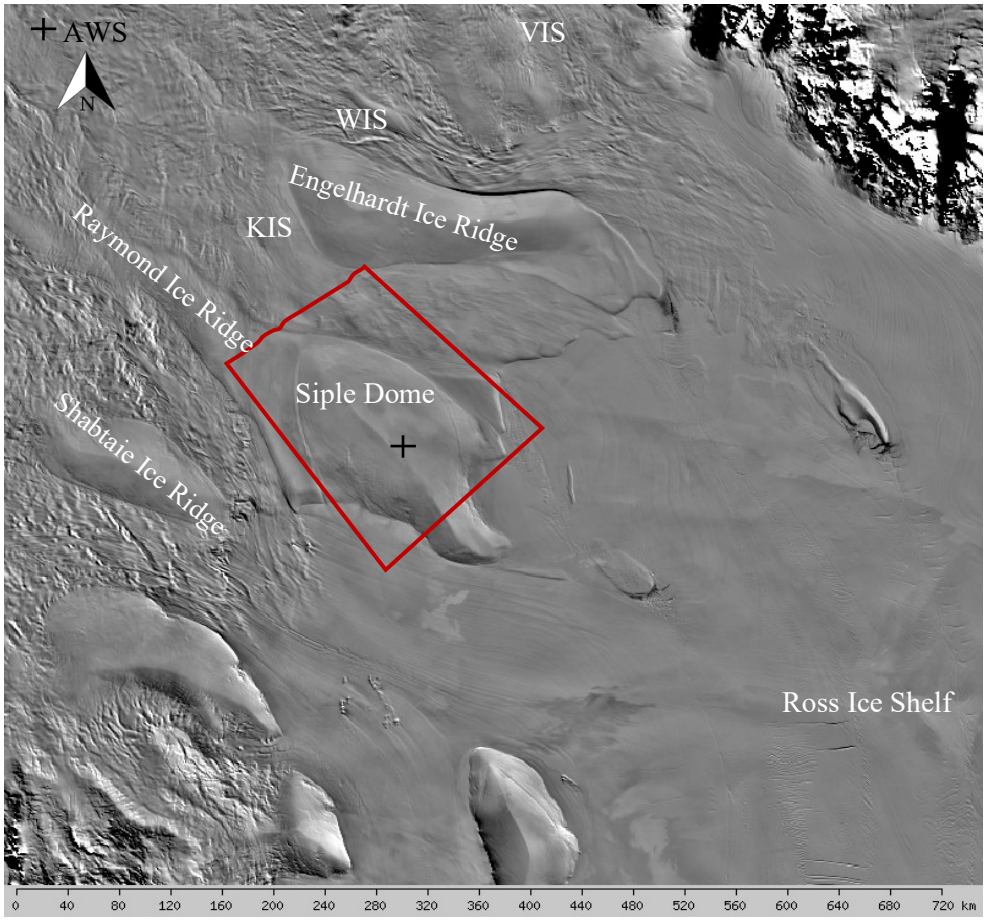

Figure 1.3: Map of the Siple Coast. The red box indicates the bounds for the region used in reanalysis and satellite data. The black plus sign indicates the Siple Dome AWS location. Background is the MODIS Mosaic of Antarctica [MOA; Scambos et al., 2007].

1.7.2 Pine Island and Thwaites Glaciers

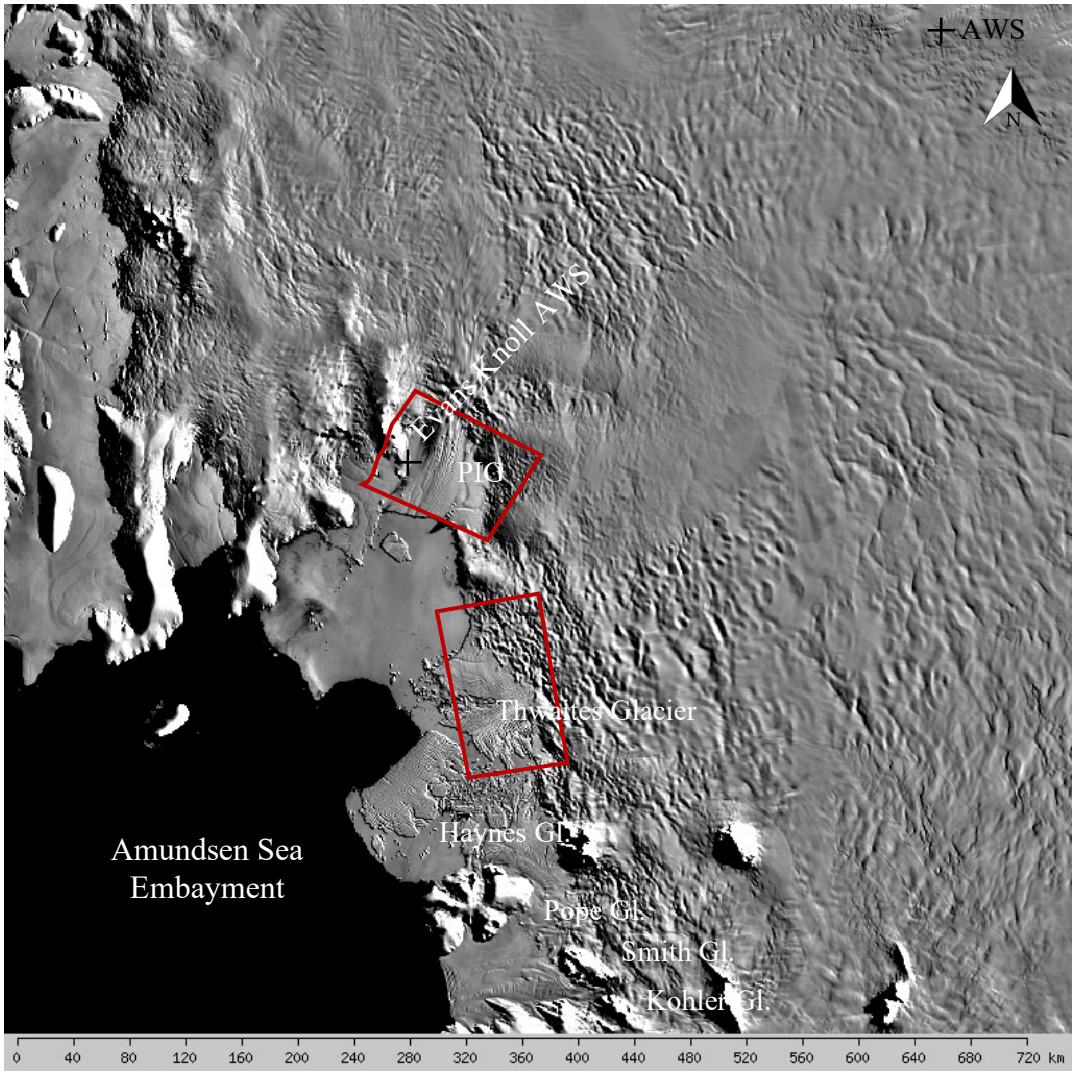

Figure 1.4: Map of Pine Island Glacier and Thwaites Glacier. The red box indicates the bounds for the region used in reanalysis and satellite data. The black plus sign indicates the Evans Knoll AWS location. Background is the MODIS Mosaic of Antarctica [MOA; Scambos et al., 2007].

On the WAIS, the Amundsen Sea Embayment meets Pine Island Glacier, Thwaites Glacier, and surrounding glaciers. The region representing Pine Island Glacier in this study is between latitude 74.833° S and 75.8° S, and longitude 97.7° W and 101.2° W. The latitude and longitude range selected for Thwaites Glacier observations was between 75° S and 76.5° S and

between 105° W and 110° W (Figure 1.4). We used satellite and reanalysis data from both of these regions to observe and diagnose melt conditions that were seen affecting both glaciers. The surface of Pine Island Glacier and Thwaites Glacier is significantly more spatially inhomogeneous than that of Siple Dome or WAIS Divide. It is believed that the disintegration of Thwaites Glacier would lead to an irreversible acceleration of the WAIS into the Amundsen Sea. Although Thwaites Glacier is experiencing a greater amount of mass loss and higher rates of glacier acceleration, no AWS is present for data corroboration. Pine Island Glacier represents a similar environment to that of Thwaites Glacier, for which we hoped to use the Evans Knoll AWS (75.14° S, 99.6° W) data for checking consistency with the reanalysis data, but the AWS data contains too many instrumental errors during the time periods of interest.

1.7.3 Ross Ice Shelf

A possible föhn event in December 2011 was observed by two AWSs, Tom and Sabrina, located at the base of the Transantarctic Mountains on the southernmost portion of the Ross Ice Shelf (Figure 1.5). The region encompassing these two AWSs is between 83.144° S and 84.5° S, and 160.343° W and 176.075° W. Tom AWS sits at 84.43° S, 171.46° W. Sabrina AWS is located slightly north at 84.237° S, 170.261° W. The elevation of the site on Ross Ice Shelf is 88 m above sea level, while the Transantarctic Mountains reach to an elevation of over 4,500 m.

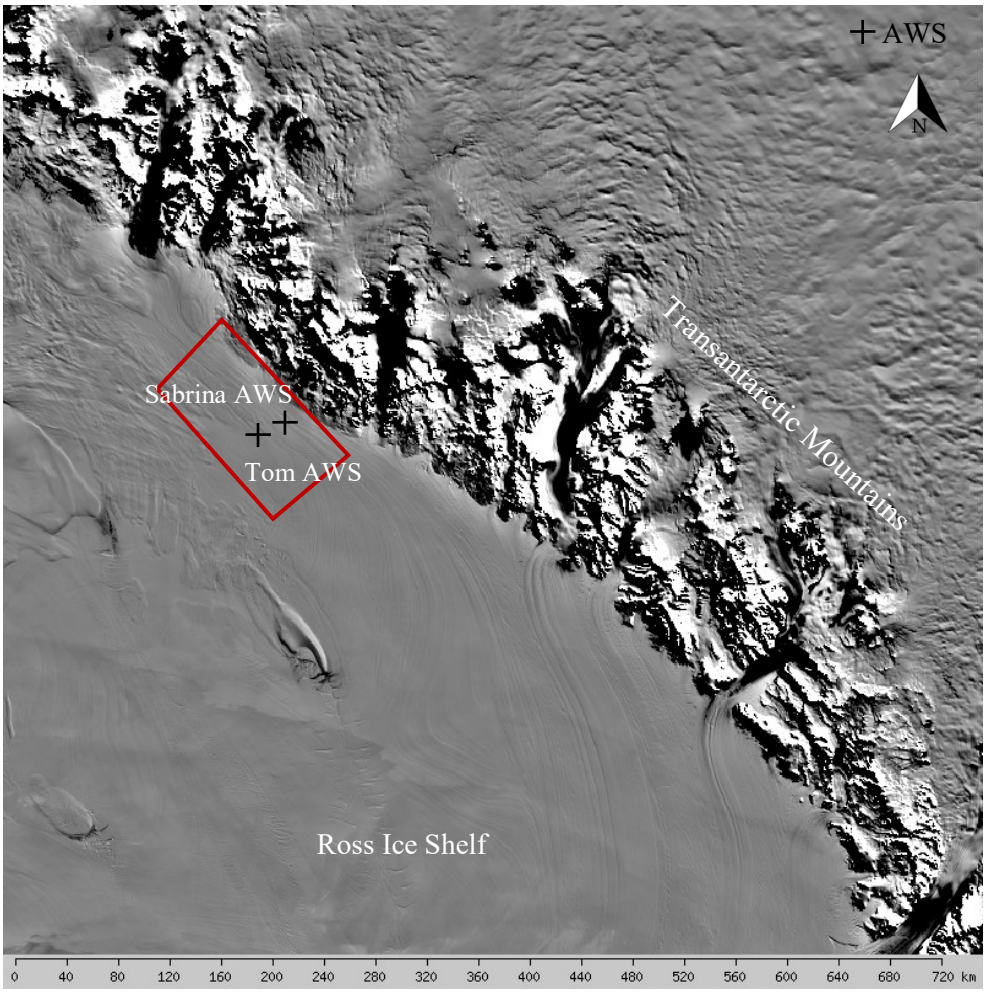

Figure 1.5: Map of Ross Ice Shelf and the Transantarctic Mountains. The red box indicates the bounds for the region used in reanalysis and satellite data. The black plus signs indicates the Tom and Sabrina AWS locations. Background is the MODIS Mosaic of Antarctica. [MOA; Scambos et al., 2007].

1.7.4 Larsen C Ice Shelf

The LCIS lies on the eastern side of the AP flanked by the AP mountains to the west, the Weddell Sea to the east and covers an area of about 45,000 km^2 (Figure 1.6). The data used for the LCIS stretches from 66.386° S to 69° S in latitude and 60.5° W to 65.431° W in longitude. While the elevation above sea level of the LCIS surface within this region has an average of ~50 m, the mountains of the AP rise to around 1,600 m, providing an effective barrier and lee

downslope for the formation of föhn winds. The AWS station used for the LCIS was AWS-14, located at 67.013° S, 61.48° W.

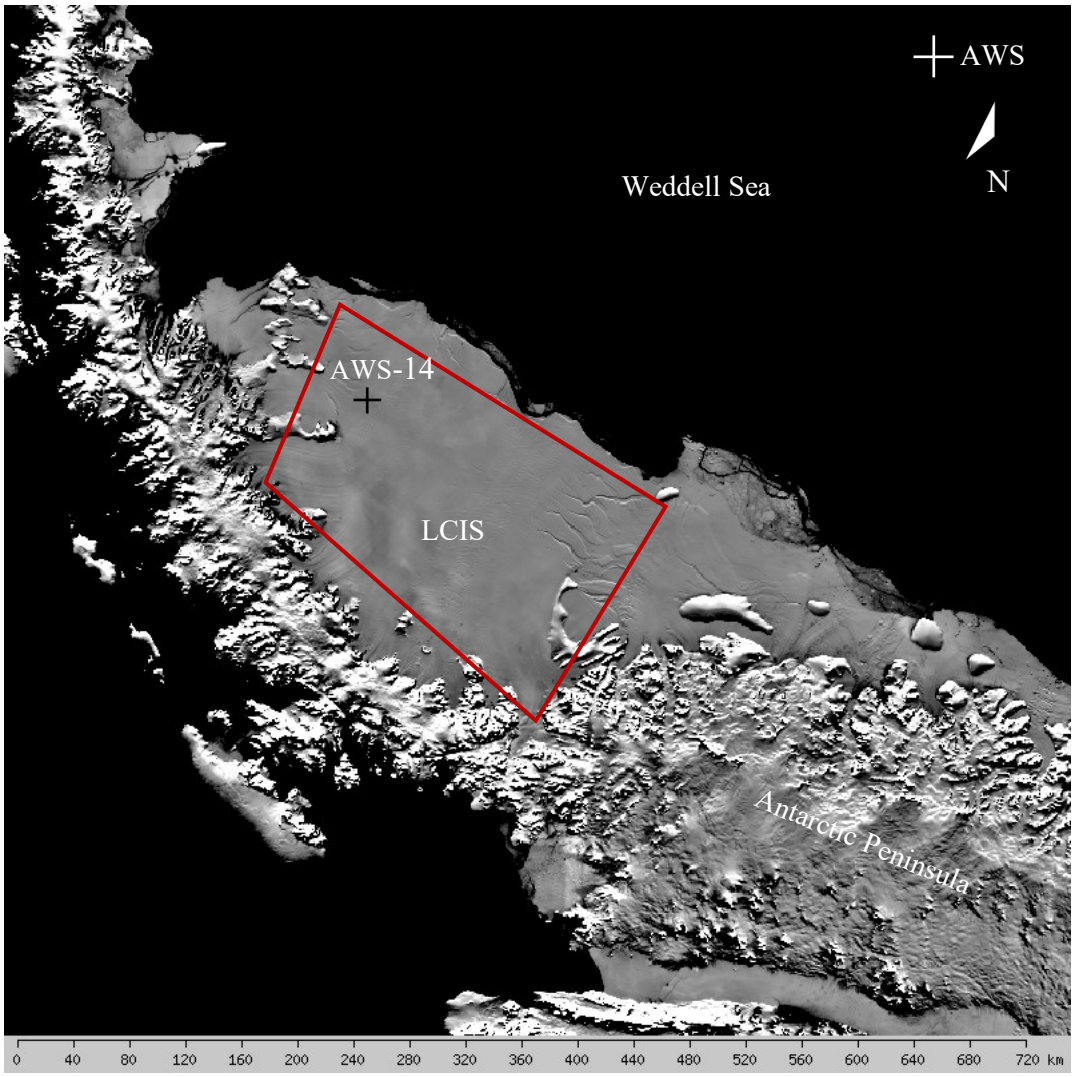

Figure 1.6: Map of the Larsen C Ice Shelf. The red box indicates the bounds for the region used in reanalysis and satellite data. The black plus sign indicates the AWS-14 location. Background is the MODIS Mosaic of Antarctica [MOA; Scambos et al., 2007].

The following is a brief description of the structure of this thesis. In Chapter 2, our data sources of satellite passive microwave data and atmospheric reanalysis models are described along with their algorithms and the methods used for this study. In Chapter 3, we detail the cases

in entirety, with all corresponding figures displayed in the Appendix. Chapter 4 categorizes each case study into individual melt drivers and summarizes the cases.

Chapter 2

Data and Methods

2.1 Data

Satellite passive microwave observations of surface brightness temperature were used to identify and diagnose surface melt. Satellite SW and LW spectral measurements and meteorological reanalysis data were used to investigate the SEB, cloud microphysics, and atmospheric properties. The AWARE case at WAIS Divide in January 2016 provides direct surface observations of radiative fluxes and skin temperature. Where available, AWSs were used to corroborate satellite and reanalysis datasets.

2.1.1 Passive Microwave Brightness Temperature

2.1.1.1 *Passive Microwave Data as a Proxy for Surface melt*

Satellite passive microwave (PMW) data can be used to detect surface ice melt by capturing rapid increases in microwave brightness temperature (T_b) due to liquid water presence in shallow firn layers [Zwally and Fiegles, 1994]. The T_b of an object is a measure of the intensity of the microwave radiation it emits. It is the product of the object's absolute physical temperature and its emissivity. The emissivity is dependent on the object's physical properties. For snow, it increases with moisture content and as grain-sizes decrease [Zwally and Gloersen, 1977]. Surface melting increases the moisture content of the snow, increasing its emissivity and

T_b. Large increases in T_b during the summer months indicate the onset of melting [Ridley, 1993]. T_b analysis used here follows Nicolas et al. [2017], and the methods proposed by Zwally and Fiegles [1994], allowing regions in the WAIS highly susceptible to a changing climate to be targeted for this study. When T_b increases more than 30 degrees above the average annual T_b, this is a proxy for melt presence [Zwally and Fiegles, 1994].

2.1.1.2 *Passive Microwave Data*

We used the daily Special Sensor Microwave Imager/Sounder (SSMIS) data from the Defense Meteorological Satellite Program (DMSP) polar orbiting spacecraft. The T_b dataset used from the SSMIS is the MEaSUREs Calibrated Enhanced-Resolution Passive Microwave Daily EASE-Grid 2.0 Brightness Temperature ESDR, Version 1 published by the National Snow and Ice Data Center (NSIDC). We use the Level-2 satellite passive microwave data of the evening pass and 19 GHz horizontally polarized (19 GHz-H) T_b at 25 km resolution. Because of discrepancies between wet and dry firn in vertical polarization, horizontal polarizations were used [Zwally and Fiegles, 1994]. The PMW data used here were verified by AWSs [Tedesco, 2009] as well as direct surface observations from the AWARE field campaign [Nicolas et al., 2017].

2.1.2 Satellite SW + LW Spectral Measurements

We used satellite data products from the NASA Cloud and Earth's Radiant Energy System (CERES) program; specifically, hourly CERES and geostationary (GEO) synoptic top-of-atmosphere (TOA) fluxes, surface fluxes, and clouds of temporal resolution 1°x1° latitude-longitude grid data (the SYN1deg data product) for corroboration of the accuracy of ERA5's

radiation components. The CERES program [Wielicki et al., 1996] analyzes high spectral and spatial resolution cloud imager data in three general steps applied to several spacecraft and sensors: (i) discriminate between cloud and cloud-free regions using reflectances at a few different wavelengths ("cloud masking"); (ii) use radiative-transfer-based retrieval algorithms with several different wavelengths to estimate cloud properties such as liquid and ice water content, optical depth, and effective droplet/particle size; and (iii) with these cloud properties, use a forward radiative transfer model to estimate the surface fluxes. In the SYN1deg product, observations from geostationary satellite sensors are used to interpolate the polar-orbiter-derived cloud properties and surface fluxes to hourly time resolution [Doelling et al., 2012; 2016]. The SYN1deg product also contains NASA A-Train retrievals of cloud liquid water path (*LWP*) and ice water path (*IWP*). A-Train represents Afternoon-Train, which is an orbital track of several satellites, including NASA's second Orbiting Carbon Observatory (OCO-2), the Japanese Global Change Observation Mission – Water (GCOM-W1), the NASA flagship Earth observatory spacecraft, Aqua and Aura, and the NASA CloudSat (radar) and Cloud-Aerosol Lidar and Infrared Pathfinder Satellite Observation (CALIPSO) spacecraft, which follow in close succession for near-simultaneous observations. For this study, we used retrievals based primarily on the Moderate-Resolution Imagine Spectroradiometer (MODIS) data from Aqua.

2.1.3 Meteorological Reanalysis Data

To assess atmospheric and surface conditions as well as compare radiative measurements, we used the European Centre for Medium-Range Weather Forecasts (ECMWF) reanalysis dataset ERA5 [ECMWF-IFS, 2008]. ERA5 uses the 4D variational data assimilation method to combine exact timing of observation with the reanalysis model output, and has data outputs of

hourly increments, an improvement compared to the three- and six-hour increments of its predecessor ERA-Interim [Dee et al., 2011]. The atmospheric state over each melt event in this study was analyzed with 10-m surface wind components, 850 hPa wind components at about 1500 m altitude skin temperature, 2 m air temperature, *LWP*, and *IWP* on a 0.5°x0.5° latitude-longitude grid. ERA5 surface radiation and turbulent fluxes are used to make the primary SEB estimate, with an additional check on the surface radiation from CERES.

2.1.4 Radiative and Surface Observations from AWARE

The AWARE campaign in January 2016 at WAIS Divide [Nicolas et al., 2017] collected direct surface observations of all radiative fluxes (SW + LW) as well as skin temperature and general atmospheric observations (notes of what kind of clouds were present). We were able to use these ground measurements to understand the strengths and limitations of the satellite SW and LW spectral measurements and the meteorological reanalysis model used in this case study.

2.2 Methods

PMW T_b data were first used to detect increases in T_b that can indicate the presence of surface melt presence. By creating time series of PMW T_b, we are able to analyze how melt changes on smaller, several-day long melt events. Looking at short duration single melt events allows us to observe the basic physics and develop an understanding of what is driving these surface melt events at a local spatial scale. The AWARE data provides direct surface observations, allowing us to determine the reliability of the datasets used for each subsequent case study at a different time and location. We then look at the radiative and turbulent fluxes, surface properties, and cloud properties to diagnose each melt event and try to determine if melt

events in Antarctica require extreme atmospheric events (similar to the conditions during the AWARE campaign) or if more typical climatological regimes can produce them.

2.2.1 Passive Microwave Brightness Temperature Time Series

For each case study, we calculated the T_b annual cold season mean for each grid cell in a region by averaging the T_b over the time period 1 April through the following 31 March. We further processed this average to filter out any values of T_b that exceeded the 30 K threshold, then repeated the averaging. We iterated on this process three times to get the most accurate T_b cold season mean for each study location, following Tedesco [2009].

We used the 19 GHz horizontal polarization (T_b) SSM/I PMW data to create a time series for each case study. First we examine the time series for the entire region using a box-and-whisker plot of the daily T_b distributions. From this, the day of highest average melt indicated by the highest average T_b was identified to choose individual grid cells within the specified region. On this day of highest average T_b, several grid cells are chosen corresponding to various percentiles across that day's overall range of T_b variability. Each percentile corresponds to a 25 km^2 grid cell which we will follow throughout the month to examine small scale evolution of a melt event. For example, our Siple Dome 2015 melt event peaked on 6 January 2015, from which we selected the grid cells from the 99^{th}, 60^{th}, 25^{th}, 10^{th}, and 5^{th} percentiles of T_b to track throughout the month. These selected grid cells are then used to create several time series to observe how the surface characteristics might change during melt conditions over a smaller scale. By tracing each grid cell (which corresponds to a percentile from the peak melt day), we can observe surface melt on smaller scales compared to continent-wide observations, which has been the dominant focus in past scientific queries. Looking at higher resolution data allows more

accurate quantification of surface melt that may be highly influenced by variability in surface topography.

2.2.2 Using AWARE Measurements to Analyze Accuracy of Reanalysis and Satellite Data

ERA5 often underestimates low-lying liquid water cloud presence most likely due to a lack of accurate cloud microphysics [Bennartz et al., 2013; Scott et al., 2019]. These inconsistencies may originate from the ERA5 algorithm which does not account for liquid cloud formation below -20^{o} C [Bennartz et al., 2013]. By comparing direct surface observations from the AWARE campaign in January 2016 with ERA5 data, we can assess the frequency of these discrepancies.

Comparisons between ERA5 and AWARE measurements show that ERA5 skin temperature tends to run a few degrees below AWARE measurements (Figure 2.1), sometimes by as much as 5 K. When comparing downwelling SW flux there is generally qualitative agreement between both AWARE and ERA5, with the exception of a few measurements that have a difference of up to almost 100 Wm^{-2} often near solar noon and midnight. Of the most concern is the inconsistency in the downwelling LW flux. ERA5 episodically fails to produce enough cloud cover. There are times when ERA5 LW flux is comparable with AWARE data, and other times when ERA5 LW fluxes are too low by tens of Wm^{-2}. Therefore, we cannot derive a simple correction for this discrepancy. Because this case study is heavily reliant on the accurate representation of cloud presence to understand local atmospheric conditions and synoptic meteorology, CERES data obtained from NASA's Atmospheric Science Data Center's (ASDC) was also considered.

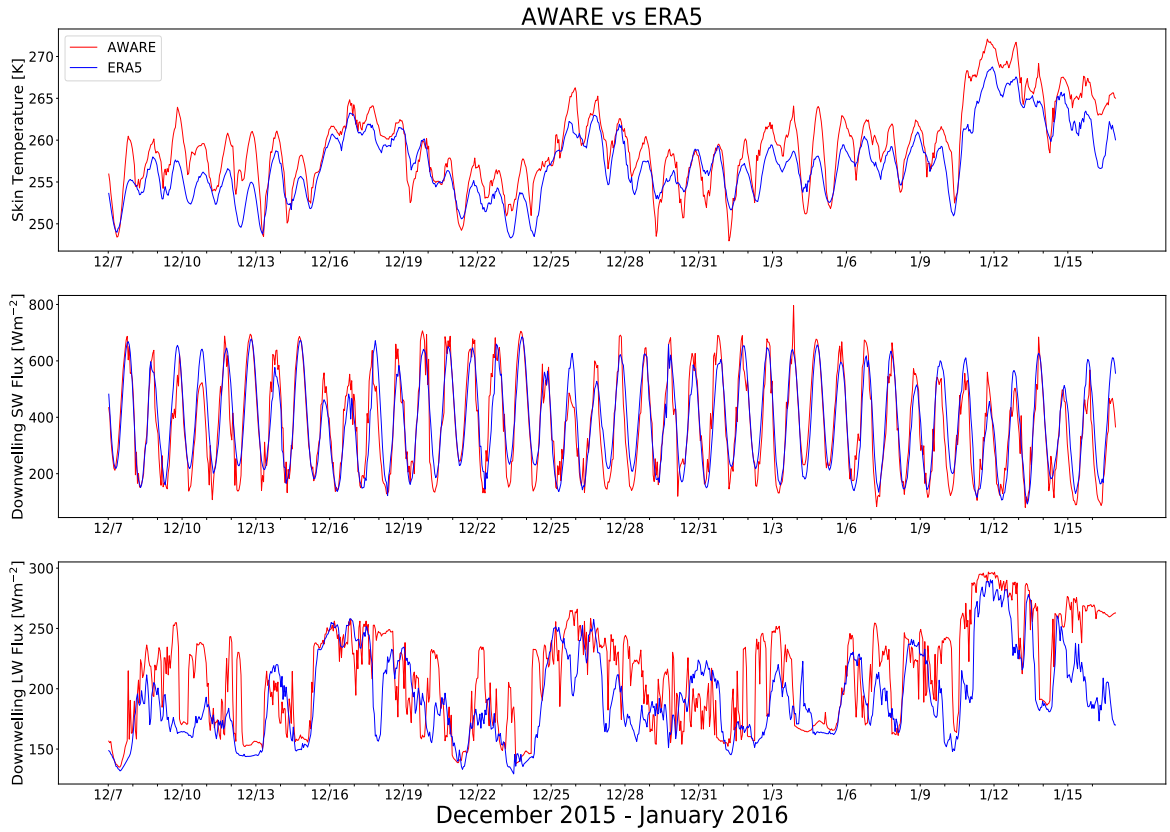

Figure 2.1: ERA5 and AWARE measurements of **(a)** skin temperature, **(b)** downwelling SW flux, and **(c)** downwelling LW flux from 7 December 2015 to 16 January 2016 over WAIS Divide.

The comparison between CERES and AWARE downwelling SW flux show that the largest discrepancy again occurs when the sun is closest to the horizon (Figure 2.2, top plot). The downwelling LW flux retrievals from CERES align with much greater consistency to the AWARE data and show more reliable identification of cloud presence, even if the CERES LW fluxes remain a little low compared with the observations (Figure 2.2, bottom plot). Based on these observations, we use the CERES *LWP* and *IWP* to assess cloud presence during our seven melt events in each case study, though *IWP* from both CERES and ERA5 is believed to be inaccurate because of the misrepresentation of mixed-phase clouds and abnormally high values during periods of time where liquid dominant clouds were known to be present (shown in

Results). We also attempt to make a second evaluation of the SEB by replacing the ERA5 radiative fluxes with those from CERES (Figure 2.3).

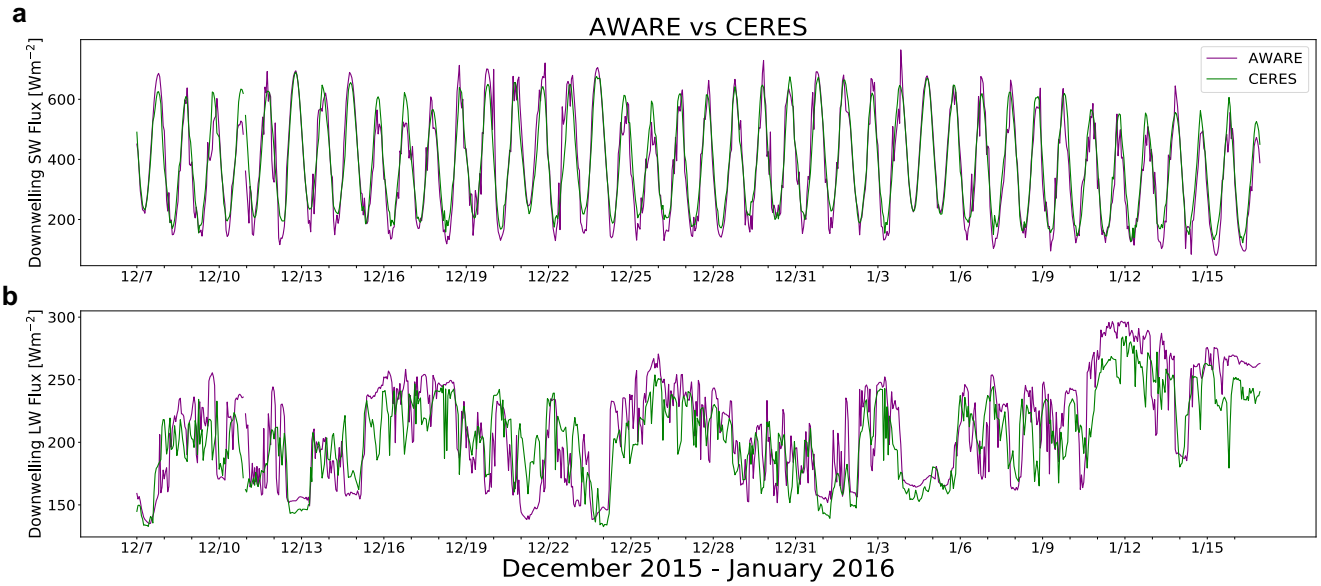

Figure 2.2: (a) CERES and AWARE measurements of **(a)** downwelling SW flux and **(b)** downwelling LW flux from 7 December 2015 to 16 January 2016 over WAIS Divide.

We then compare the ERA5 net radiation and *ME* with a second estimate using CERES radiative fluxes and ERA5 turbulent fluxes (Figure 2.3). The ERA5 *ME*, although possibly suffering from too little cloud *LWP*, shows a positive *ME* over several days at the start of the melt event, and a diurnal cycle in *ME* outside of the melt period, consistent with Nicolas et al. [2017]. The second *ME* estimate using CERES radiative fluxes show several periods of positive *ME* over numerous days throughout the month, including during climatologically normal conditions before the melt event. We conclude that a combination of *ME* components using satellite-derived and reanalysis-derived values does not give physically meaningful results, despite the better qualitative agreement between CERES LW fluxes and AWARE measurements

(Figure 2.3). For all subsequent new cases, we therefore evaluate *ME* using ERA5, and use the CERES cloud property retrievals to separately assess the realism of ERA5 model simulations of cloud properties.

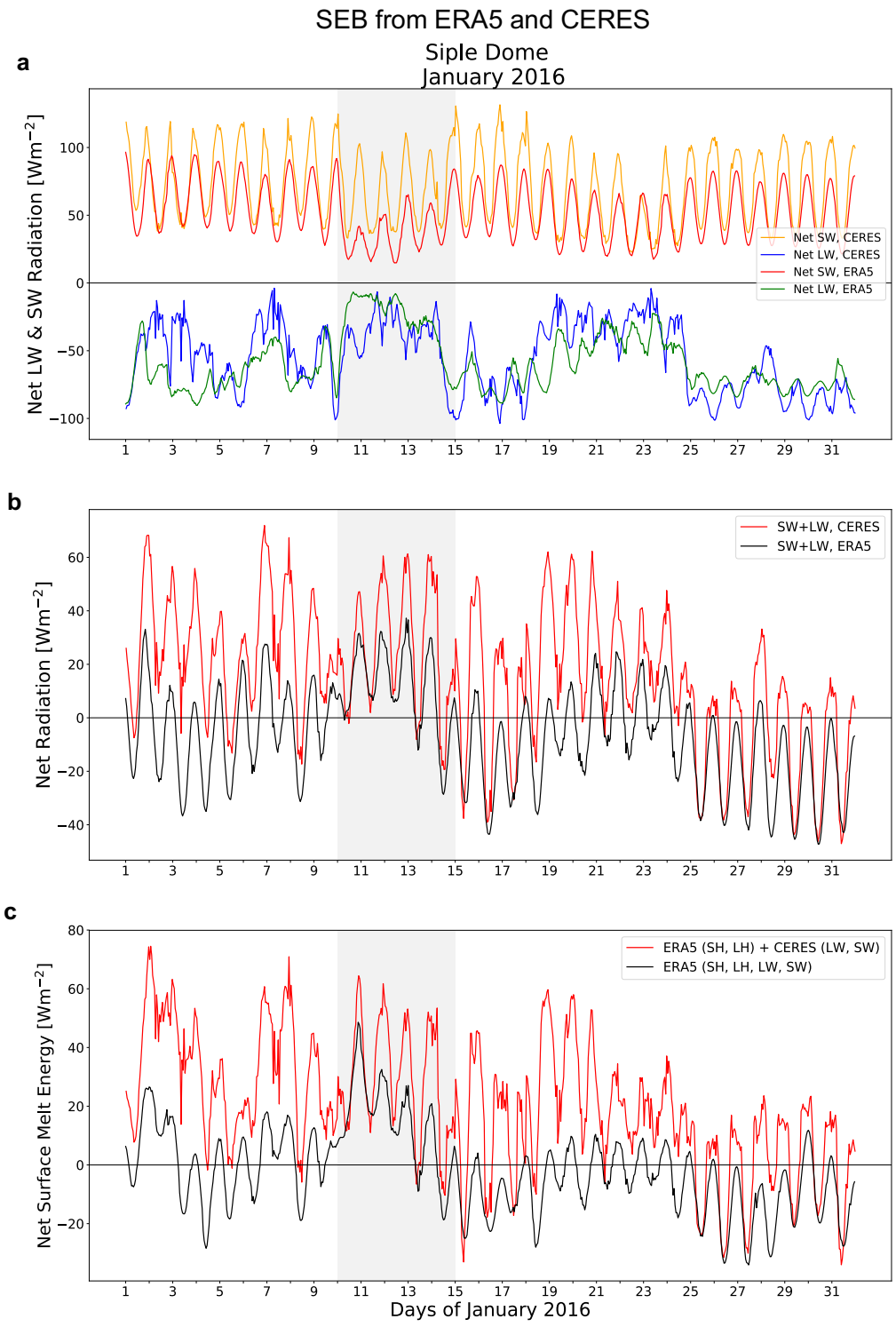

Figure 2.3: Hourly surface radiation components spatially averaged over the Siple Dome region during January 2016: **(a)** individual net surface radiation terms from ERA5 and CERES; **(b)** total surface radiation from ERA5 and CERES. Panel **(c)** shows the total *ME* using entirely the ERA5 fluxes (black) and using CERES for the radiation while retaining ERA5 for turbulent fluxes (red).

2.2.3 Radiative and Cloud Property Time Series from Reanalysis and Satellite Data

Using hourly values of radiative fluxes, turbulent fluxes, and cloud properties, we created multiple time series to assess the SEB and *ME*, as well as surface and atmospheric conditions over the entire month that each specific melt event occurred during. The time series were created by using the same grid cells (same area of 25 km^2 regions that correlate to a melt percentile) from the T_b time series. The location of each percentile grid cell was extracted from the ERA5 data, which was then plotted and observed over the month in question. By analyzing *ME* and surface and atmospheric properties on smaller scales, we are able to observe small changes in the ice surface and atmosphere that may drive be driving melt. The time series provided us with the most accurate assessment of climatological conditions occurring during each melt event. We also created spatially averaged time series of the same properties (SW+LW radiation, net radiation, surface + latent heat flux, net turbulent flux, net surface *ME*, and surface emissivity and 2 m and skin temperatures) to sum up each melt event.

Chapter 3

Results

The meteorological synopsis is first discussed to give climatological context for each of the seven melt cases. Moist, optically thick clouds from a strong advection from the Amundsen Sea sector were present in January 2016 (Siple Dome case), as well as in December 2011 and February 2013 at Pine Island and Thwaites Glaciers. These atmospheric conditions led to thermal blanketing driving surface melt. Thin, low-level clouds are seen enhancing surface radiation in January 2012 at Pine Island and Thwaites Glacier, as well as in January 2015 at Siple Dome. Upsurges in sensible heat flux that raise surface temperatures can be seen inducing melt in December 2011 at Siple Dome, as well as possibly extending the melt event at Pine Island and Thwaites Glacier in February 2013. Lastly, we look at föhn wind cases on the Ross Ice Shelf and the LCIS, both which confirm elevated wind speeds in conjunction with skin temperature just before the indicated melt.

3.1 Meteorological Synopsis

3.1.1 January 2016

In January 2016 WAIS Divide, Siple Dome, and a majority of the WAIS was covered by optically thick, liquid-bearing low-lying clouds that heated the surface through thermal blanketing and triggered a widespread melt event. The extent of this extreme event is linked to a strong advection of warm marine air over the WAIS [Nicolas et al., 2017]. This type of warming was seen driving large melt events in December 2011 and February 2013 around Pine Island

Glacier and Thwaites Glacier, and is typical of West Antarctica during the austral summer. Pine Island Glacier and Thwaites Glacier sit coastally along the Amundsen Sea Embayment, where marine air masses are often present. Large-scale modes of climate variability, such as SAM and El Niño, have an increasing impact on this region as the global climate changes [Bromwich et al., 2004; Fogt et al., 2011]. Observations of melt events of similar magnitude and atmospheric conditions as AWARE are key to improving the understanding of the cloud microphysics that influence melt regimes.

3.1.2 January 2015

January 2015 showed a low-pressure system over the Ross-Amundsen Seas that was blocked briefly by a weak ridge, resulting in a warm marine airmass to be driven up over the Marie Byrd Land ice cap (Figure 4.6). The airmass continued to descend over the Siple Coast, contributing to the observed föhn wind effect. Northerly winds during the event are consistent with strong descent and adiabatic warming. It is possible that this descent of dry air pushed any potentially optically thick clouds into *LWP* values within the Bennartz et al. [2017] thin cloud range. The water vapor in the column will still radiate to the surface more than clear skies in the absence of advection, thus a perfect environment for melt [Ryan Scott, NASA Langley Research Center, personal communication, March 2020].

Synoptic Analyses from 4 January – 8 January 2015

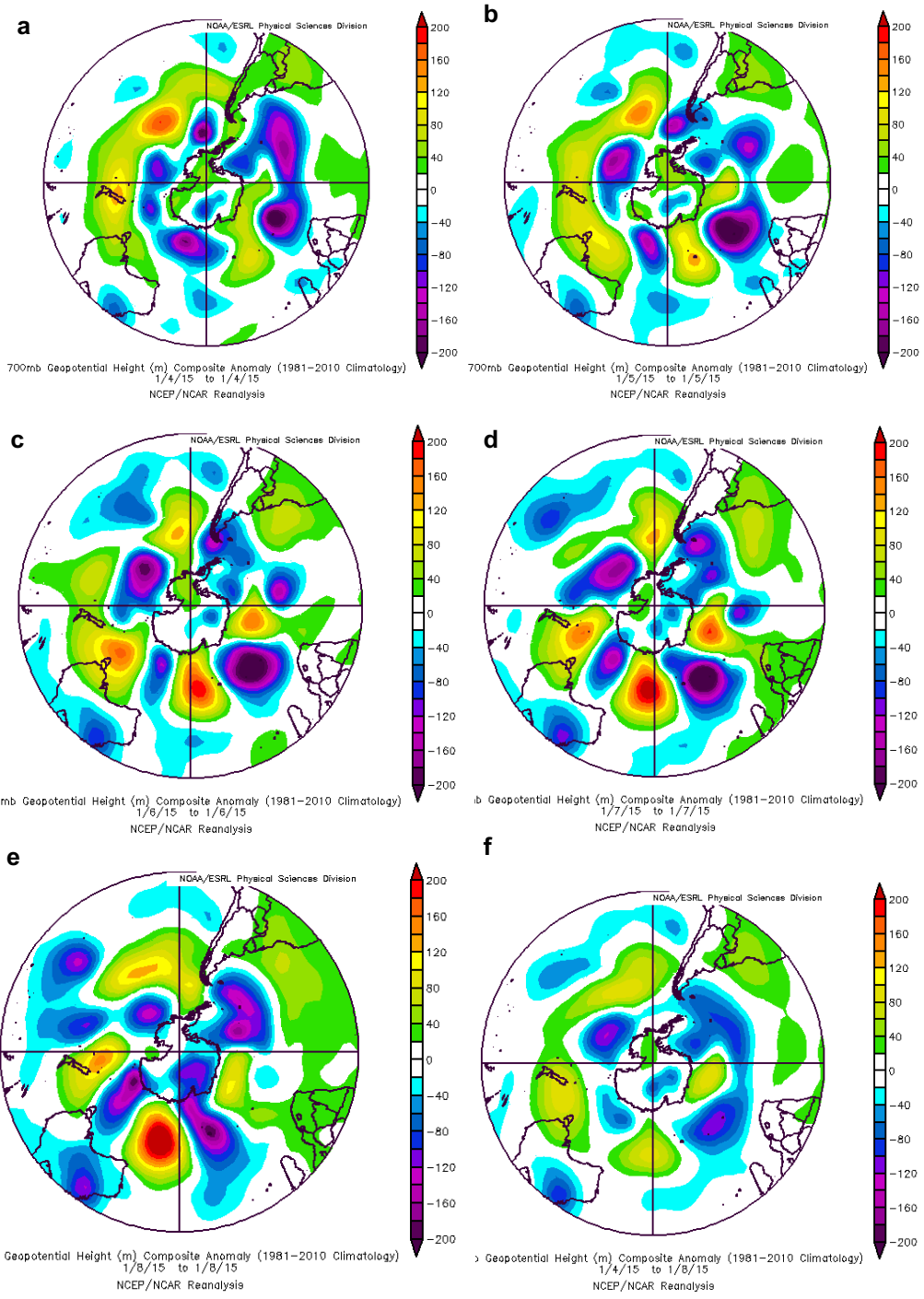

Figure 3.1: 700 mb Geopotential Height (m) Composite Anomaly (1981 – 2010 Climatology) spanning 4 January 2015 **(a)**, 5 January 2015 **(b)**, 6 January 2015 **(c)**, 7 January 2015 **(d)**, 8 January 2015 **(e)**, and the full period composite **(f)**.

3.1.3 February 2013

In February 2013, a strong pressure ridge built up and remained stationary over the Amundsen-Bellingshausen Sea region. The combination of this and the low-pressure system over the Ross Sea set up warming conditions for the Amundsen Sea Embayment, where an anomalously strong zonal pressure gradient facilitated meridional flow toward the area (Figure 4.2). This synoptic pattern is representative of frequent surface melting in the area [Ryan Scott, NASA Langley Research Center, personal communication, March 2020].

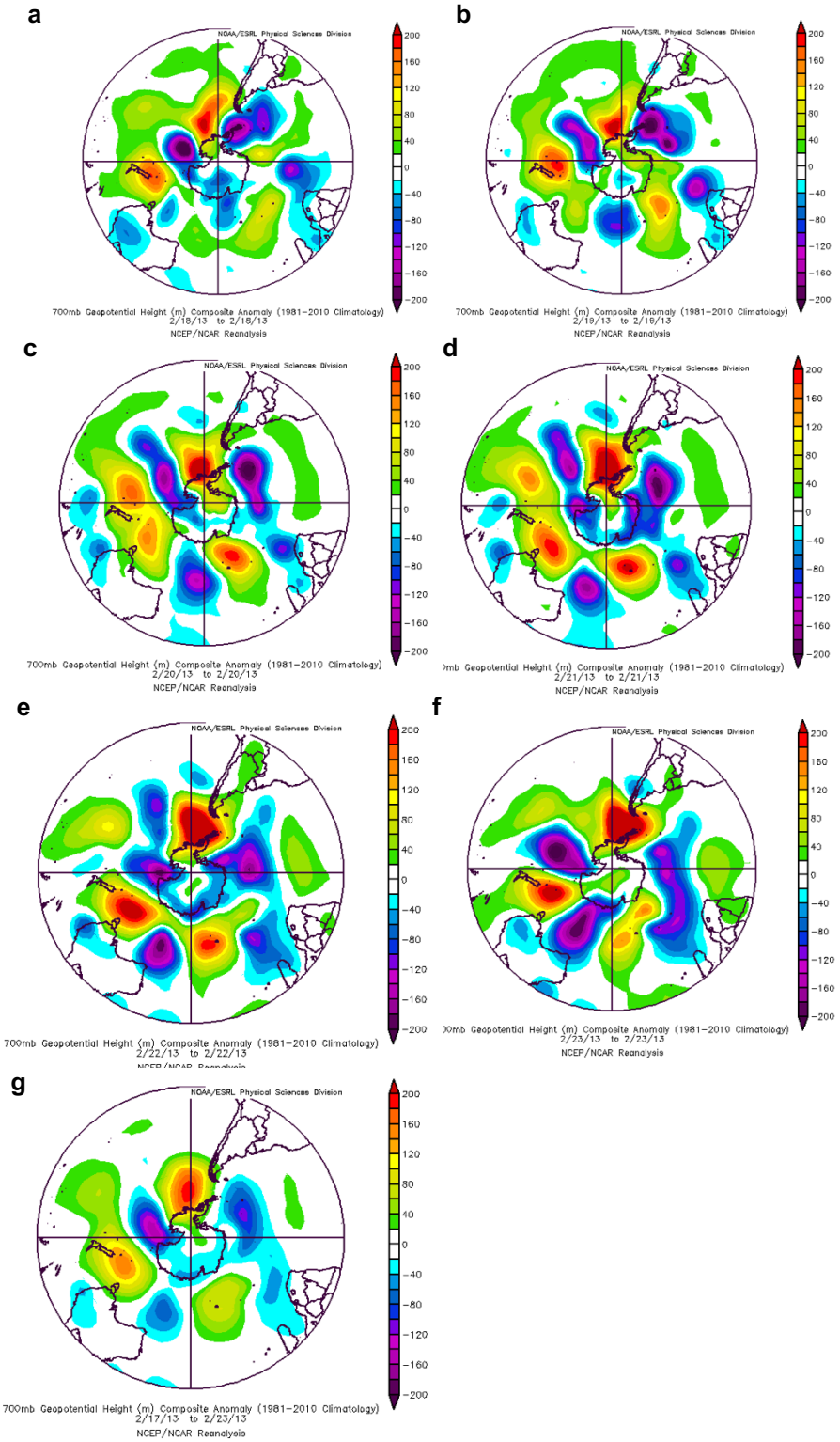

Figure 3.2: 700 mb Geopotential Height (m) Composite Anomaly (1981 – 2010 Climatology) spanning 18 February 2013 **(a)**, 19 February 2013 **(b)**, 20 February 2013 **(c)**, 21 February 2013 **(d)**, 22 February 2013 **(e)**, 23 February 2013 **(f)**, and the full period composite **(g)**.

3.1.4 January 2012

January 2012 saw strong positive SAM conditions in conjunction with a weak pressure ridge building off of the southern tip of South America, which briefly diverted the circumpolar westerly flow toward the Amundsen Sea Embayment region (Figure 4.5) [Ryan Scott, NASA Langley Research Center, personal communication, March 2020]. This is an example of melt occurring during a synoptic condition during which melt is not very frequent [Scott et al., 2019].

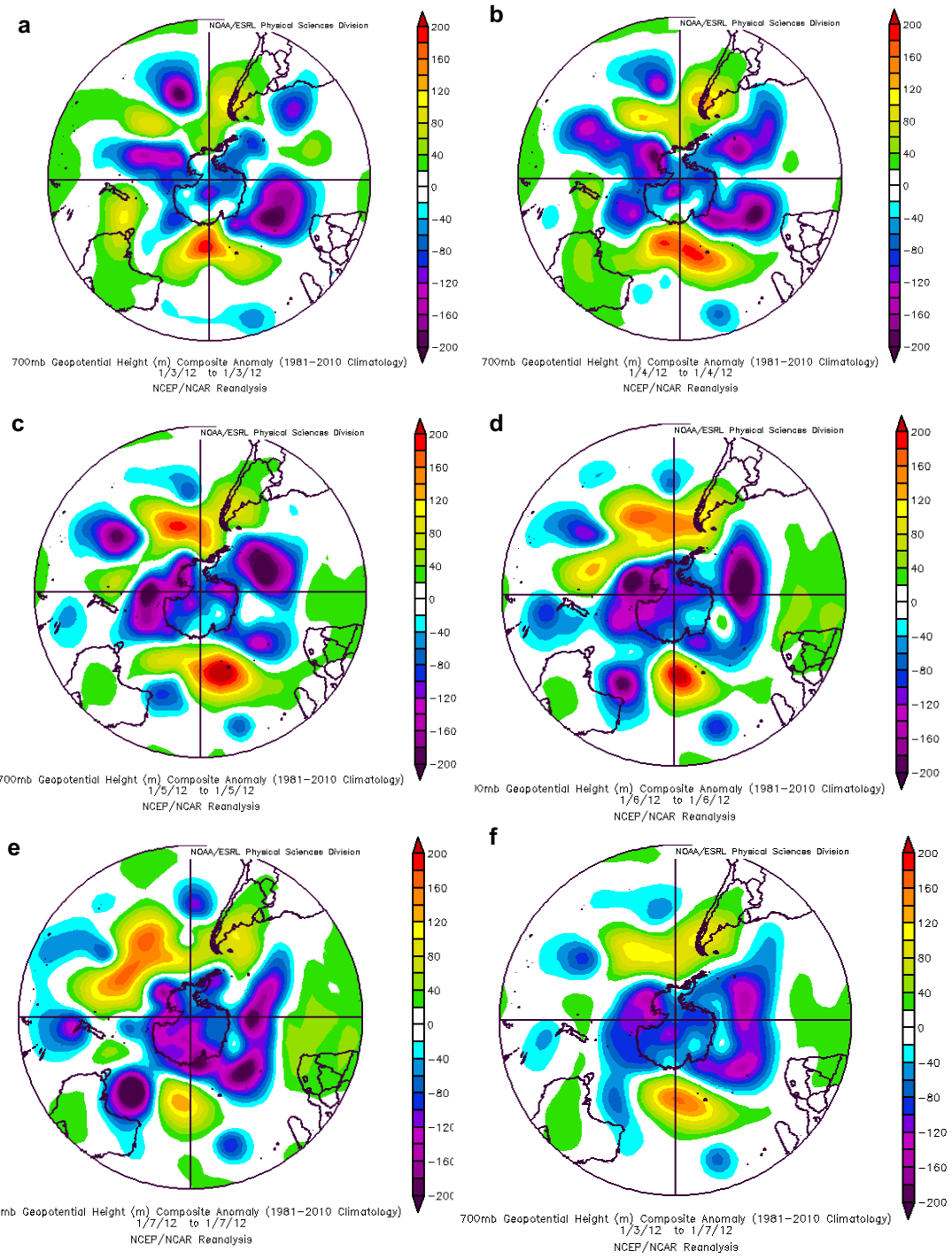

Figure 3.3: 700 mb Geopotential Height (m) Composite Anomaly (1981 – 2010 Climatology) spanning 3 January 2012 **(a)**, 4 January 2012 **(b)**, 5 January 2012 **(c)**, 6 January 2012 **(d)**, 7 January 2012 **(e)**, and the full period composite **(f)**.

3.1.5 December 2011

In December 2011, a deep low-pressure system slowly propagated eastward and drove a warm, moist airmass up over the WAIS (Figure 4.1). This airmass sat over the WAIS and resulted in optically thick, liquid cloud presence over the entire Amundsen Sea Embayment. This airmass subsequently descended and was funneled onto the southern Ross Ice Shelf, producing the föhn wind effect over the Siple Coast [Ryan Scott, NASA Langley Research Center, personal communication, March 2020].

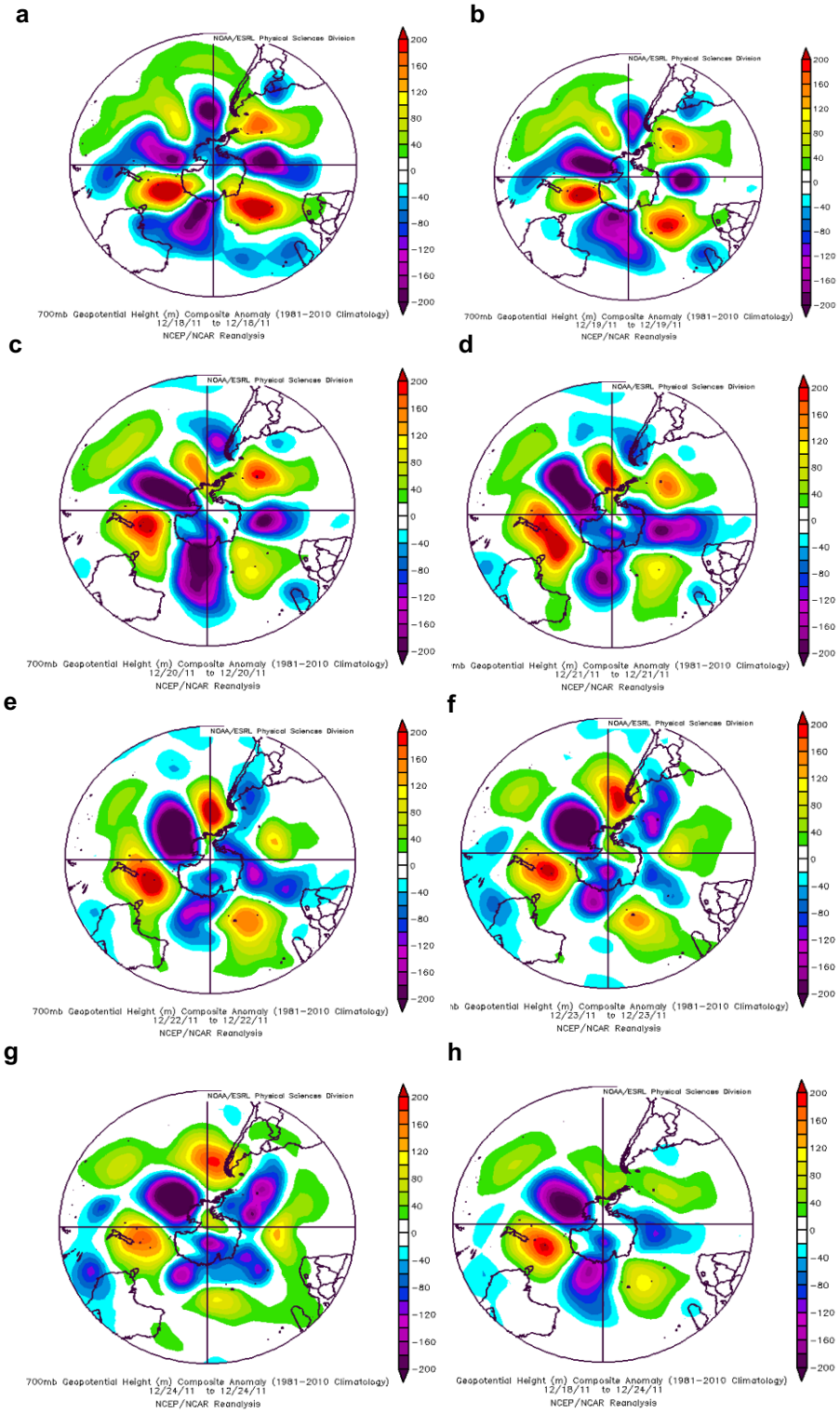

Figure 3.4: 700 mb Geopotential Height (m) Composite Anomaly (1981 – 2010 Climatology) spanning 18 December 2011 **(a)**, 19 December 2011 **(b)**, 20 December 2011 **(c)**, 21 December 2011 **(d)**, 22 December 2011 **(e)**, 23 December 2011 **(f)**, 24 December 2011 **(g)**, and the full period composite **(h)**.

3.2 Siple Dome

3.2.1 December 2016 (AWARE)

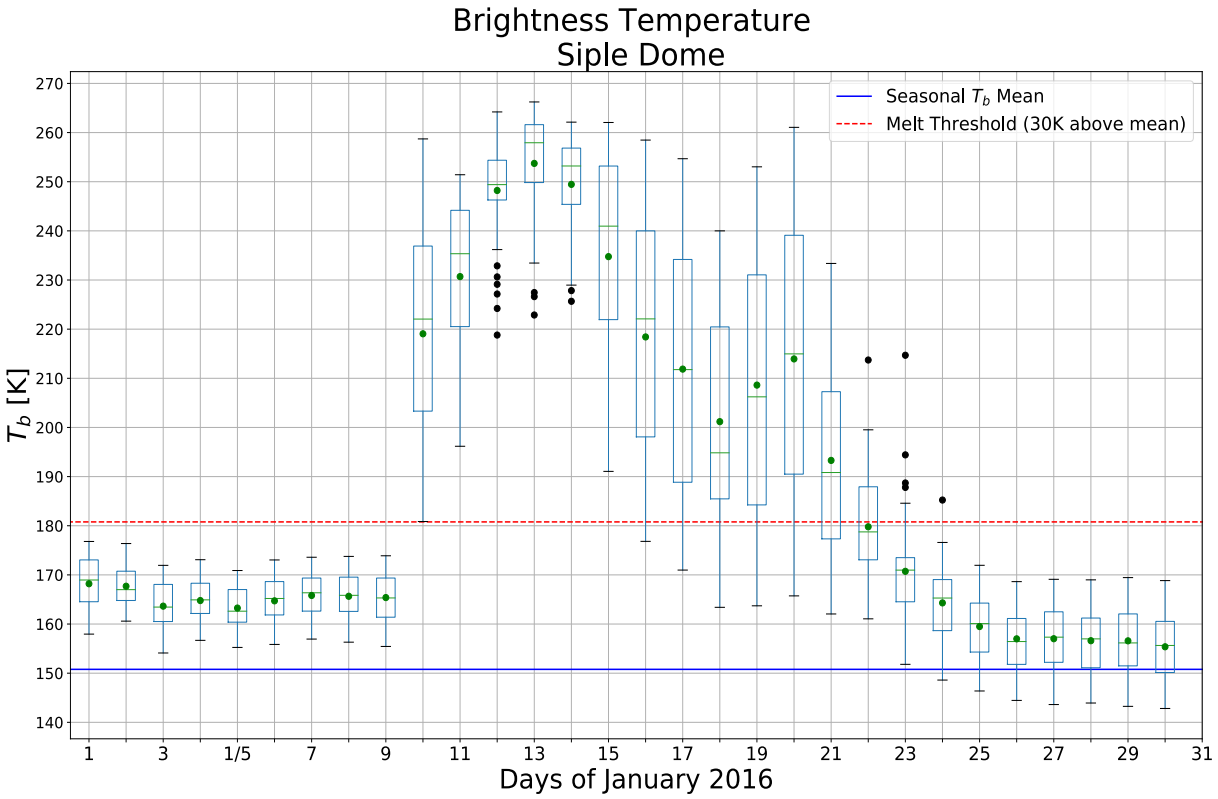

Figure 3.5: Box-and-whisker plot of daily 19 GHz-H T_b over the Siple Dome region over January 2016; with the prior year cold season mean and 30 K common melt detection threshold shown by the blue and red lines, respectively.

The T_b and emissivity time series at Siple Dome during the same time period of the AWARE event in January 2016 showed a melt event of similar timing and duration (onset timing 10 January and duration of 11 days to January 21; Figure 3.5). Looking at the spatial extent of the melt event, all grid cells show values of emissivity of close to 0.65 prior to 10 January (indicating a dry, homogenous ice sheet surface); after 10 January T_b values exceeded 180 K (indicating surface melt) (Figure 3.6). After 24 January there is a slightly greater range in the surface emissivity for the individual percentiles, suggesting that melt was not entirely uniform

over the region. Optically thick clouds, similar to those observed at WAIS Divide during this same time period are shown by the CERES *LWP* values peaking over 60 gm^{-2} (Figure 3.7 (a)). ERA5 also picks up on the clouds present during the melt event. Radiative fluxes at this site show comparable values to ground observations at WAIS Divide throughout January 2016 (Figure 3.8). Spatially averaging the data across the region summarizes the melt event's SEB components (Figure 3.8). During the melt period, net SW radiation decreases to around 20 Wm^{-2} as net LW radiation rises to just below 0 Wm^{-2}, indicating optically thick cloud presence (Figure 3.8 (a,b)). This drastic change in net radiation drives the net *ME* to remain positive for several days (10 – 13 January), even throughout the diurnal cycles (Figure 3.8 (e)). ERA5 skin temperature and 2 m temperature rise to above freezing on 10 January in conjunction with the radiation trends seen (Figure 3.8 (f)). As expected, this case generally reflects the AWARE measurements as the same air mass sat over the majority of the WAIS.

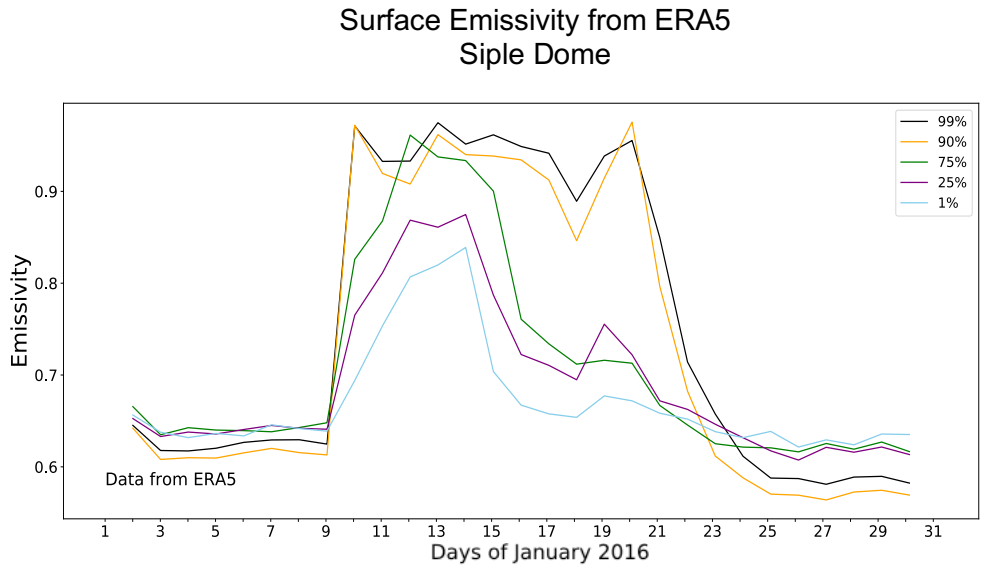

Figure 3.6: Surface emissivity calculated using ERA5 skin temperature for several individual grid cells corresponding to various individual percentiles from within the daily distributions shown at right. The percentiles specified in the legend are identified at the day of highest overall T_b (January 13).

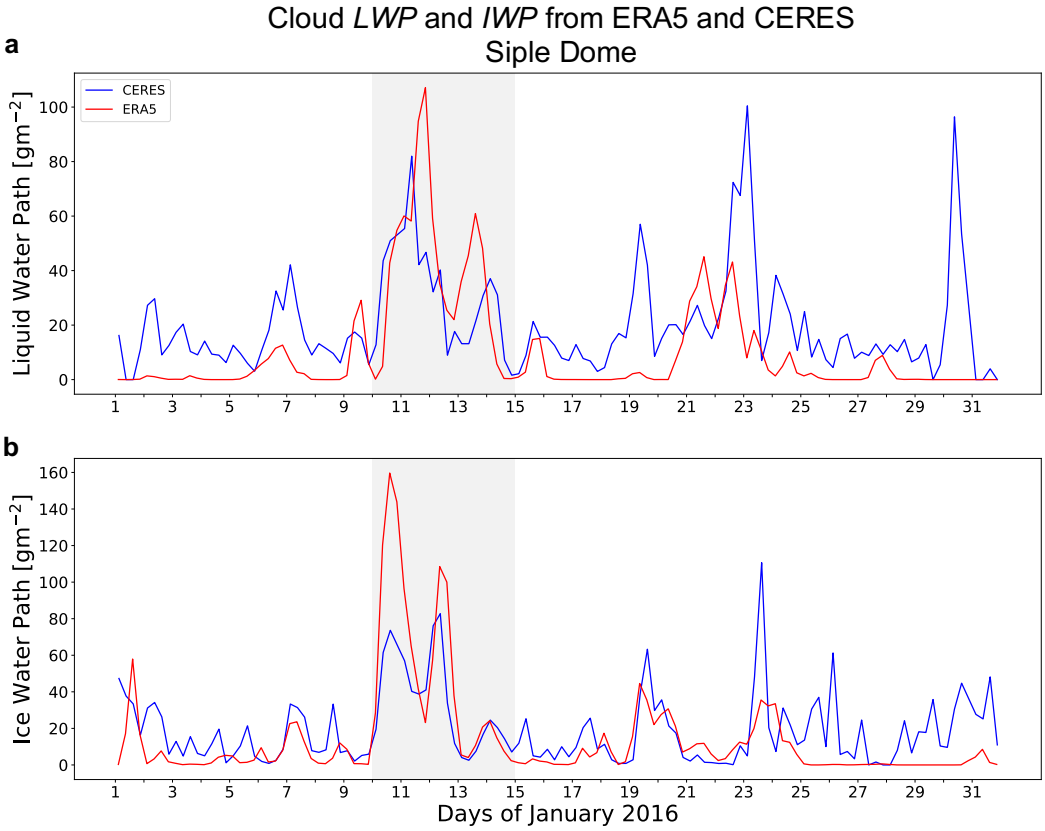

Figure 3.7: CERES retrievals over the Siple Dome region for January 2016 (blue) and **(a)** ERA5 model estimates (red) of cloud liquid water path and **(b)** cloud ice water path.

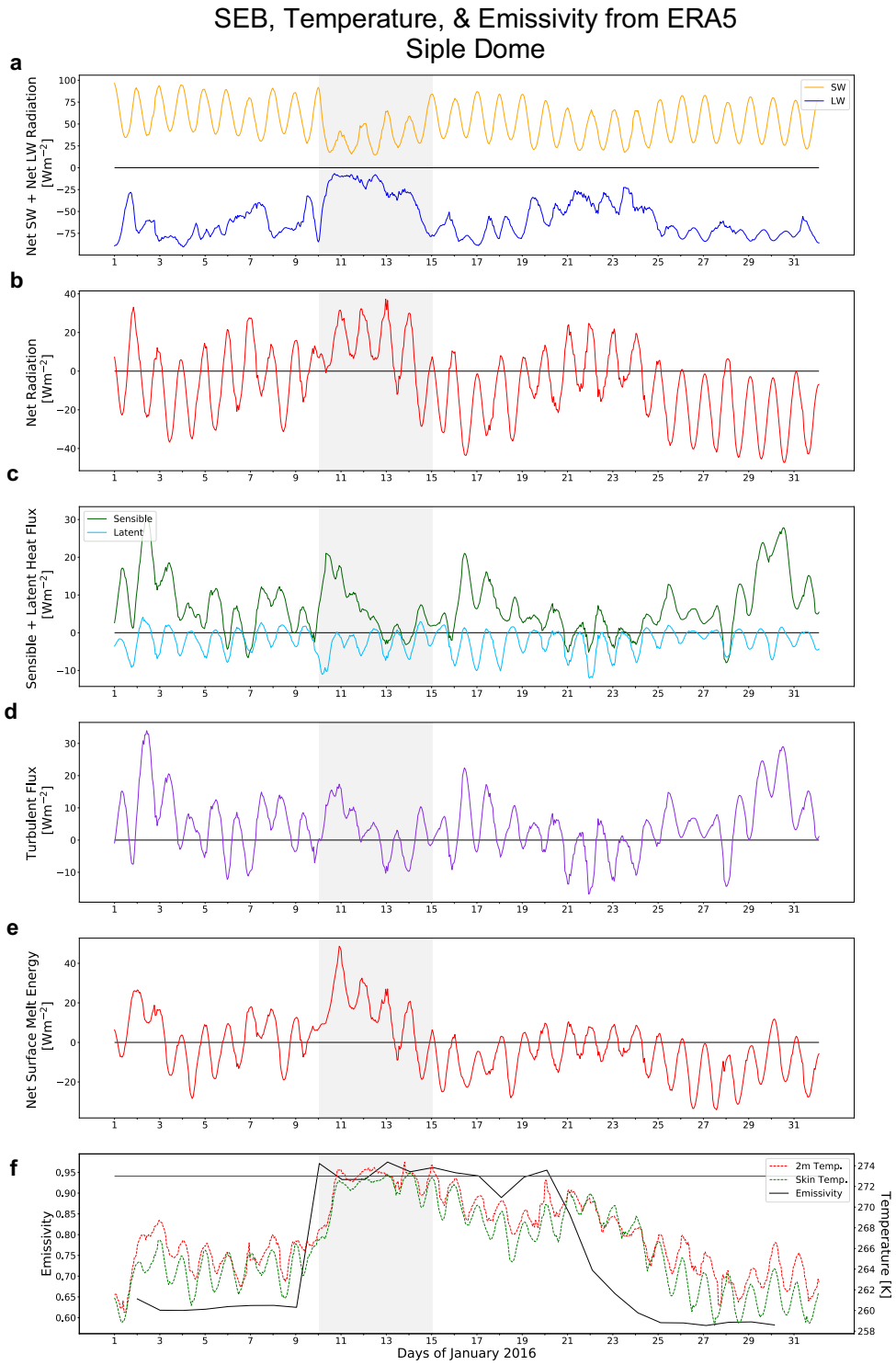

Figure 3.8: Spatially averaged time series of individual SEB components **(a-d)**, the total ME **(e)**, and the emissivity with 2 m temperature and skin temperature **(f)** over the Siple Dome region in January 2016. The red line in **(f)** is the melting point (273 K). The light grey shading denotes the melt event.

3.2.2 January 2015

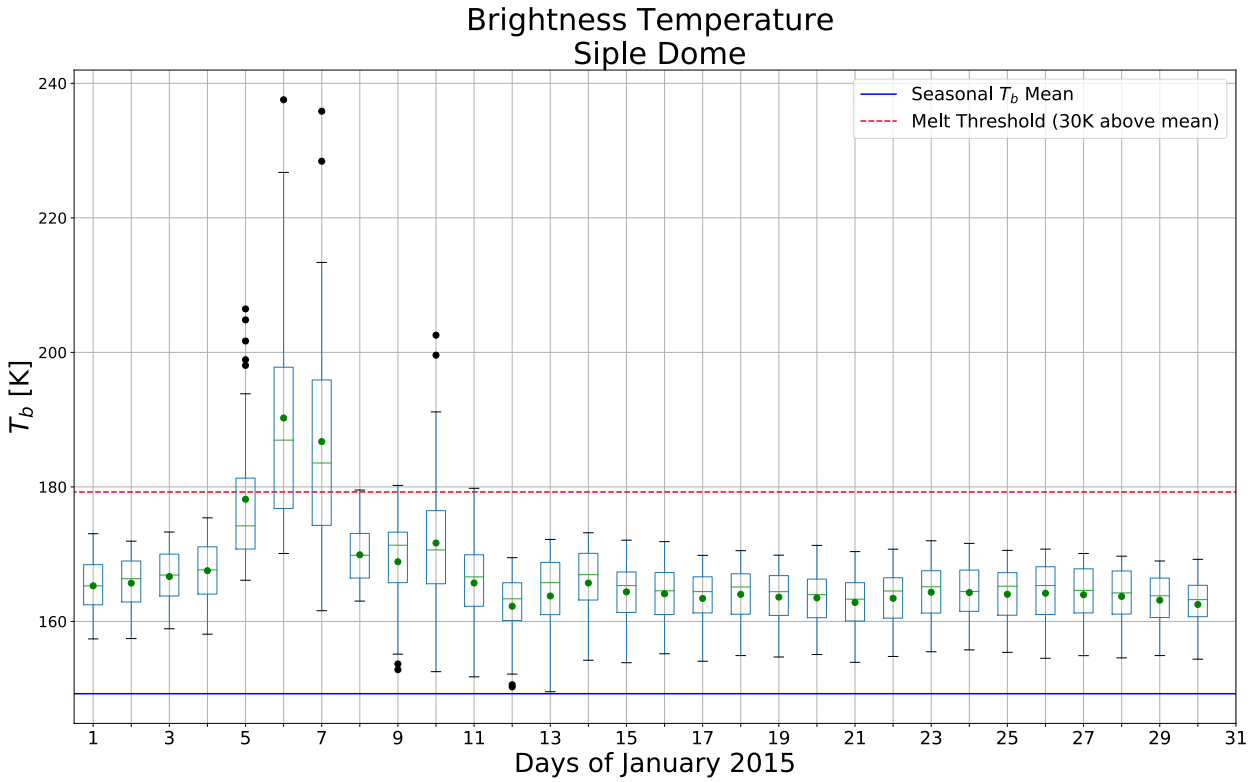

Figure 3.9: Box-and-whisker plot of daily 19 GHz-H T_b over the Siple Dome region over January 2015; with the prior year cold season mean and 30 K common melt detection threshold shown by the blue and red lines, respectively.

At Siple Dome in January 2015, the daily 19 GHz-H T_b peaked to about 235 K on 5 January and remained elevated above the melt threshold for 3 days (Figure. 3.9). Emissivity reaches 0.90 as T_b reaches its maximum value, indicating surface pooling (Figure 3.10). After the melt event, all percentiles return to a dry firn value of around 0.60. CERES *LWP* remains between 20 and 50 gm^{-2} during the melt, typical of optically thin clouds (Figure 3.11 (a)). Spatially averaging the data across the region summarizes the melt event's SEB components (Figure 3.12). During the melt, net LW radiation increases drastically from around -80 Wm^{-2} to -20 Wm^{-2} and net SW radiation is decreased to around 30 Wm^{-2} but not eliminated entirely

(Figure 3.12 (a,b)). There are no significant changes in turbulent flux observed (Figure 3.12 (c,d)). The net *ME* increases but does not remain entirely positive throughout the diurnal cycle (Figure 3.12 (e)). Skin and 2 m temperature rise to almost melting point but ERA5 did not record above 273 K, though we know ERA5 tends to run low (Figure 3.12 (f)). The CERES values of *LWP*, in combination with downwelling SW radiation that is largely attenuated but with some still reaching the surface, are suggestive of optically thin, liquid-bearing cloud presence over the region.

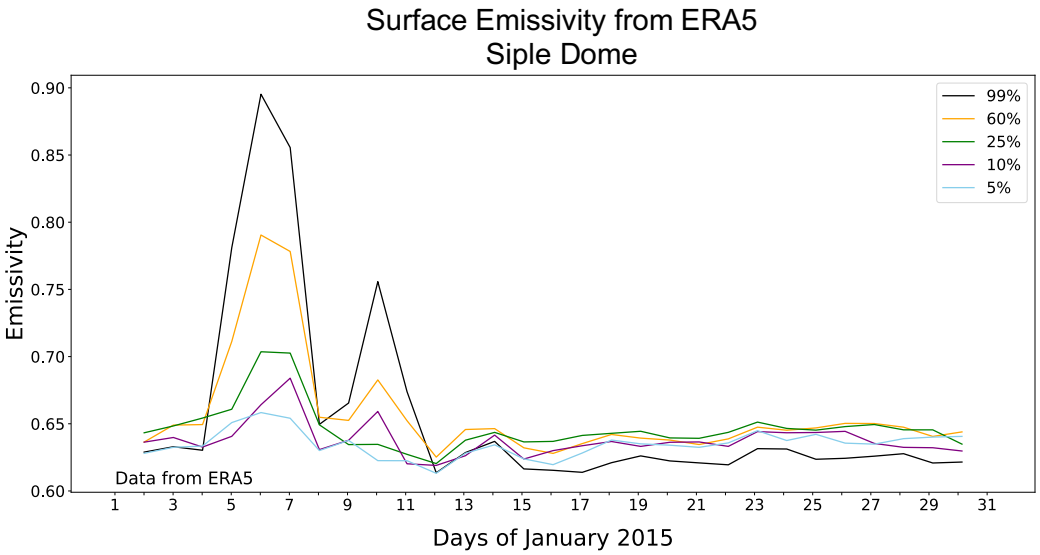

Figure 3.10: Surface emissivity calculated using ERA5 skin temperature for several individual grid cells corresponding to various individual percentiles from within the daily distributions shown at right. The percentiles specified in the legend are identified at the day of highest overall T_b (January 6).

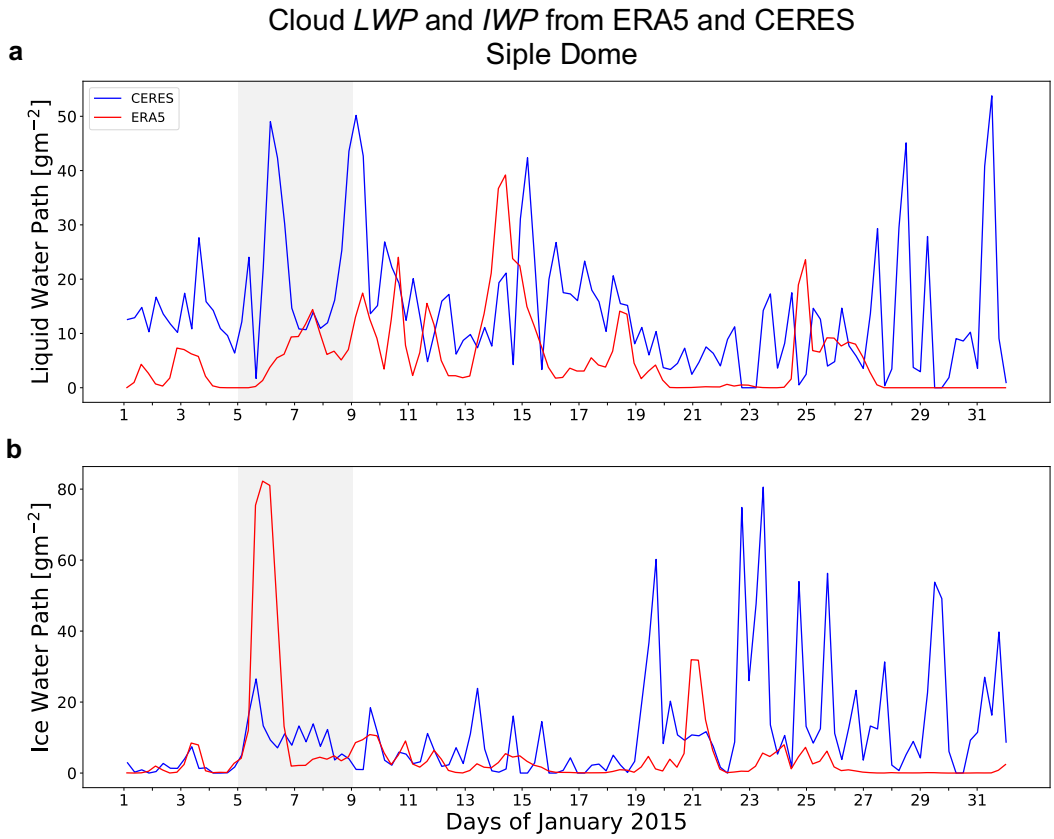

Figure 3.11: CERES retrievals over the Siple Dome region over January 2015 (blue) and **(a)** ERA5 model estimates (red) of cloud liquid water path and **(b)** cloud ice water path.

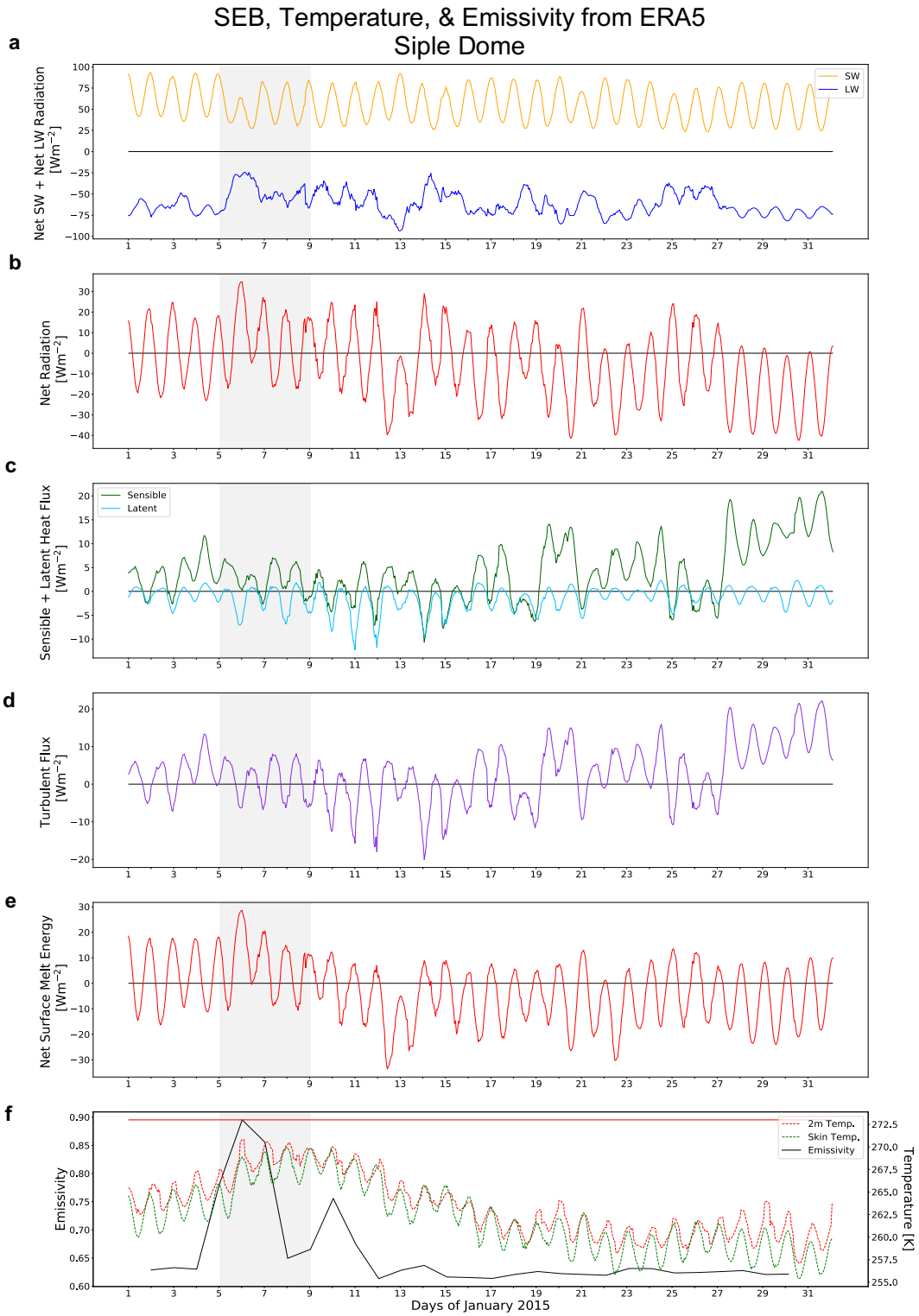

Figure 3.12: Spatially averaged time series of individual SEB components **(a-d)**, the total ME **(e)**, and the emissivity with 2 m temperature and skin temperature **(f)** over the Siple Dome region in January 2015. The red line in **(f)** is the melting point (273 K). The light grey shading denotes the melt event.

3.2.3 December 2011

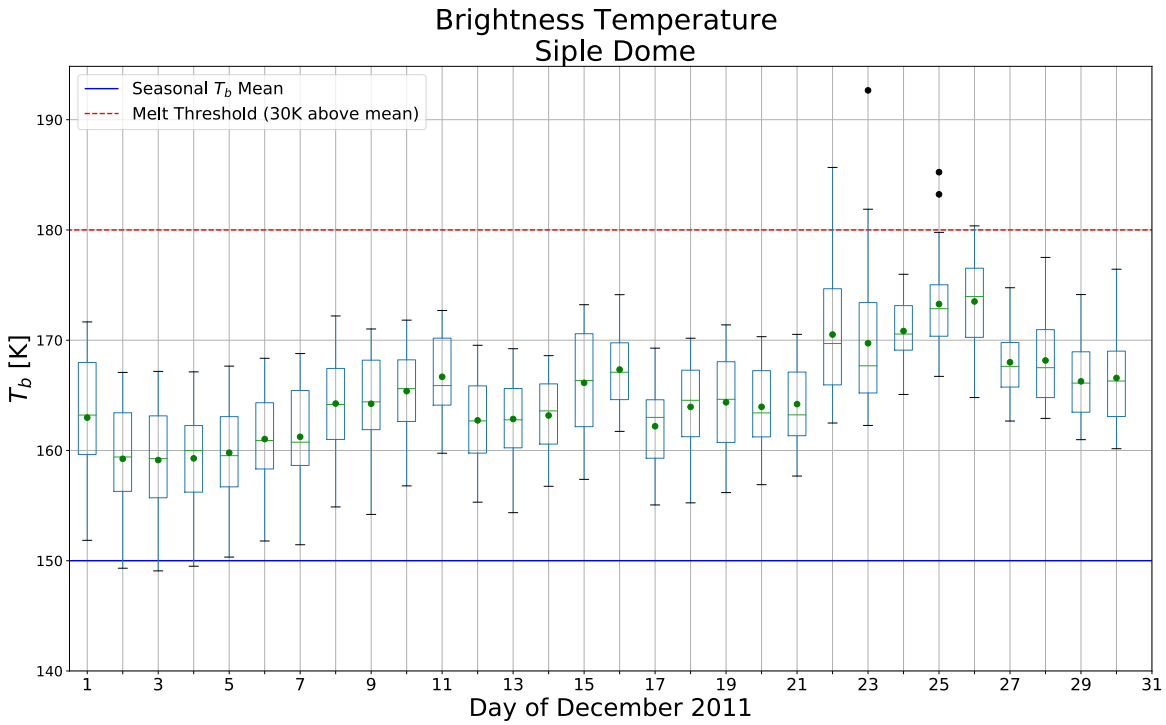

Figure 3.13: Box-and-whisker plot of daily 19 GHz-H T_b over the Siple Dome region over December 2011; with the prior year cold season mean and 30 K common melt detection threshold shown by the blue and red lines, respectively.

The melt observed at Siple Dome in December 2011 occurred on 22 December and sustained until around 27 December (Figure 3.13). As in all Siple Dome cases, the emissivity showed close distribution in the values of dry firn until the melt event when they increased to a maximum value of around 0.75 (Figure 3.14). The surface emissivity in the 99th percentile grid cell independently tracks this rise in surface temperatures, with values around 0.61 on 21 December to 0.69 on 26 December. This value of emissivity is relatively low for what is expected of wet snow surface, but there are measurement uncertainties in the satellite PMW data. CERES retrievals and ERA5 estimates for cloud *LWP* and *IWP* show that *LWP* remains below 20 gm^{-2} and varies until 25 December, when there is a large jump in value to about 85 gm^{-2}

(Figure 3.15). This indicates that there is inconsistent cloud cover until 25 December, when liquid-dominant, optically thick clouds move in to the region and elongate the surface melt. The time series of the spatially averaged SEB components, net *ME*, and skin and 2 m temperature, summarizes the melt event (Figure 3.16). Between 21-25 December, there are distinct diurnal cycles such that would present difficulty for the clouds to maintain any all-wave radiative enhancement. During this time, however, there is an impulse in sensible heat flux that rises rapidly to 27 Wm^{-2} on 21 December then gradually decays while remaining positive until 21 December (Figure 3.16 (c)). The net turbulent flux remaining mostly positive over this entire period, with a slight decrease below zero for several hours each day (Figure 3.16 (d)). The *ME* exhibits diurnal cycles ranging from positive to negative values from 21-27 December (Figure 3.16 (e)); however, *ME* is positive throughout two diurnal cycles from 19-20 December, just before the observed melt period. Skin and 2 m air temperatures rise steadily from maximum daily values around 270 K on 21 December to freezing by 26 December (Figure 3.16 (f)). The sensible heat flux appears to drive up skin temperatures enough to precondition the surface to melt, while optically thick, liquid clouds move into the region around 25 December and prolong the melt.

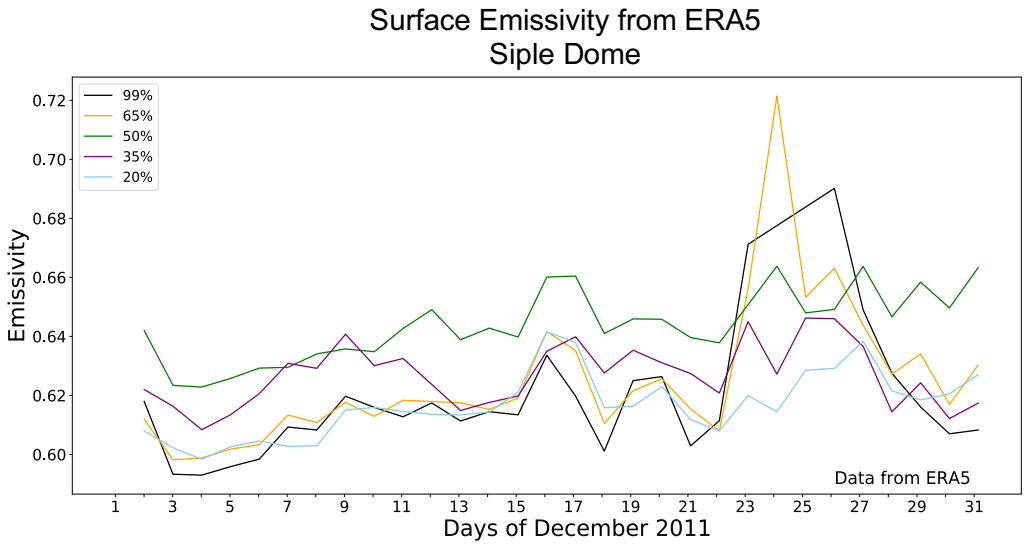

Figure 3.14: T_b Surface emissivity calculated using ERA5 skin for several individual grid cells corresponding to various individual percentiles from within the daily distributions shown at left. The percentiles specified in the legend are identified at the day of highest overall T_b (December 26).

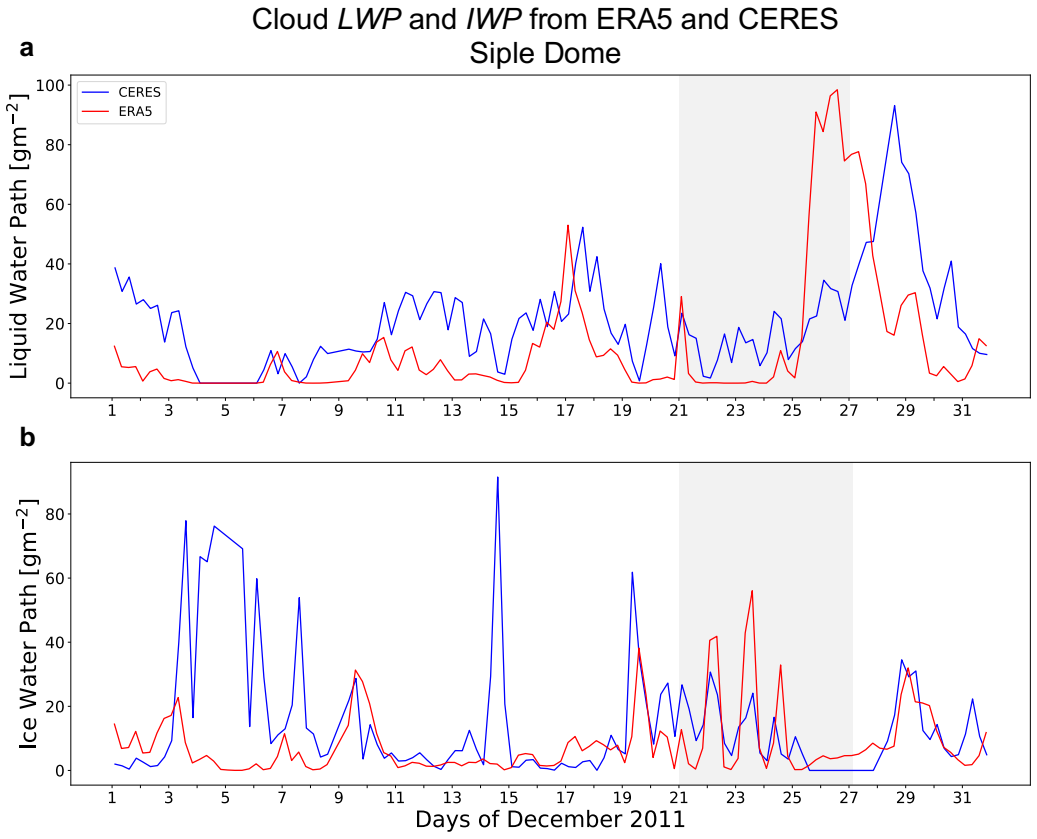

Figure 3.15: CERES retrievals over the Siple Dome region over December 2011 (blue) and **(a)** ERA5 model estimates (red) of cloud liquid water path and **(b)** cloud ice water path.

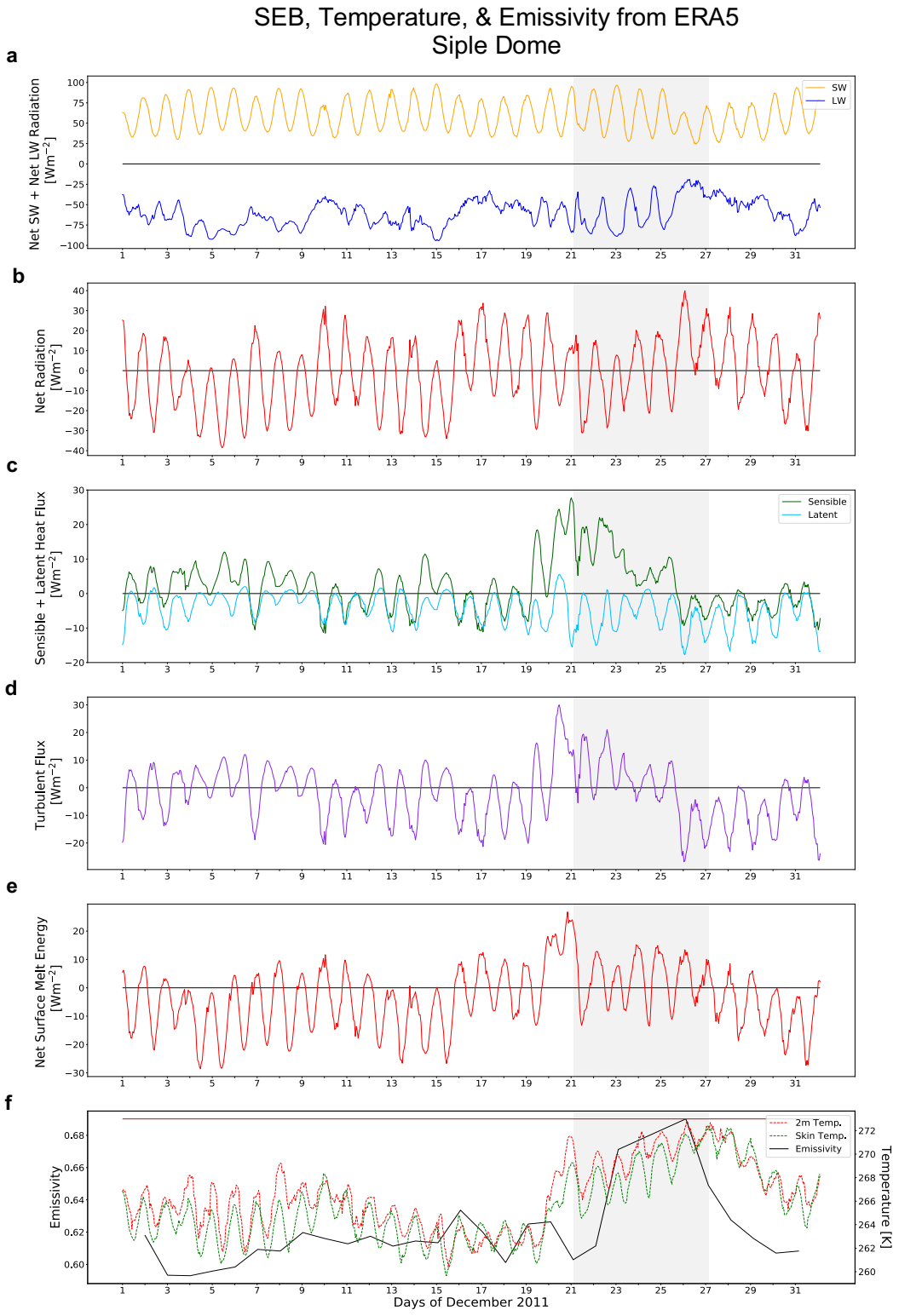

Figure 3.16: Spatially averaged time series of individual SEB components **(a-d)**, the total ME **(e)**, and the emissivity with 2 m temperature and skin temperature **(f)** over the Siple Dome region in December 2011. The red line in **(f)** is the melting point (273 K). The light grey shading denotes the melt event.

3.3 Pine Island & Thwaites Glacier

3.3.1 December 2011

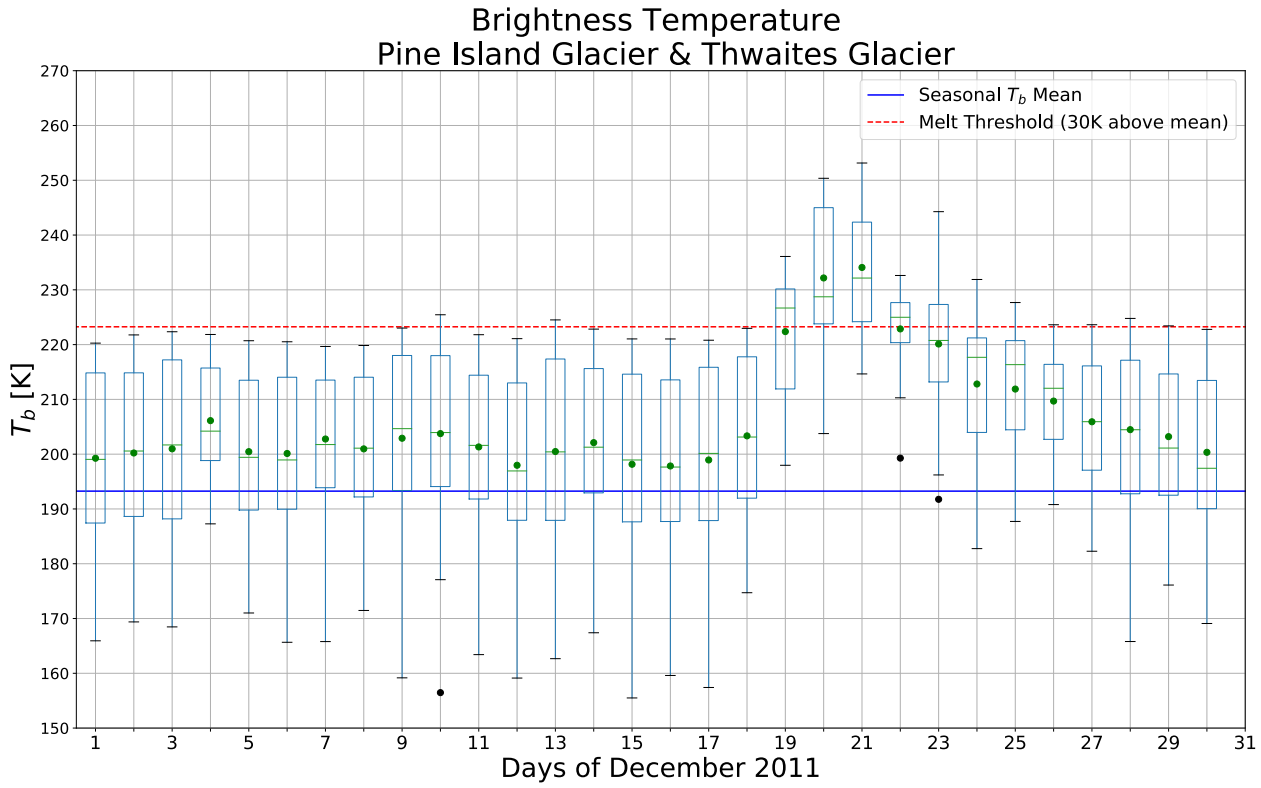

Figure 3.17: Box-and-whisker plot of daily 19 GHz-H T_b over the Pine Island Glacier and Thwaites Glacier region over December 2011; with the prior year cold season mean and 30 K common melt detection threshold shown by the blue and red lines, respectively.

Pine Island and Thwaites Glaciers experienced a melt event from 19 December through 25 December (Figure 3.17). Emissivity calculated from ERA5 for the individual grid cells relating to each percentile shows that the surface of Pine Island Glacier, Thwaites Glacier, and the surrounding region is significantly more inhomogeneous than that of WAIS Divide, Siple Dome, or the Ross Ice Shelf (Figure 3.18). Being exposed to the Amundsen Sea contributes to high rates of ice sheet instability from intrusions of warm, salty water and causes the edges of the

WAIS in this area to crevasse at higher frequencies than locations further inland. In addition to this, the proximity to the Hudson Mountains results in a larger variety in surface elevations through the region. This difference in surface homogeneity is shown through the emissivity percentiles. The highest melt percentile pixels of 95% and 75% were at 0.65 and 0.70 respectively until the melt event, where they then reached a value of just over 0.90 (Figure 3.18). The lowest percentile pixels (25%, 30%) remained around 0.80 and proceeded to rise meagerly during the event (to around 0.85). This indicates that areas that experiencing the greatest volume of melt began as dry firn, where areas that were already wet failed to melt significantly more than they were already experiencing. The significant variation in surface topography provides contrasts that must be observed at higher spatial resolutions when considering the impact of surface melt over the entire ice shelf.

The *LWP* spikes to around 100 gm^{-2}, suggestive of optically thick clouds thermally blanketing the region and driving melt (Figure 3.19). A large decrease in net SW radiation to a maximum daily value of around 25 Wm^{-2}, and an increase in net LW radiation to 0 Wm^{-2} occurs on the 20^{th} (Figure 3.20 (a,b)), driving the net *ME* positive for the following 3 days, even throughout the diurnal cycle (Figure 3.20 (e)). The skin temperature and 2 m temperature rise to above freezing during this time (Figure 3.20 (f)).

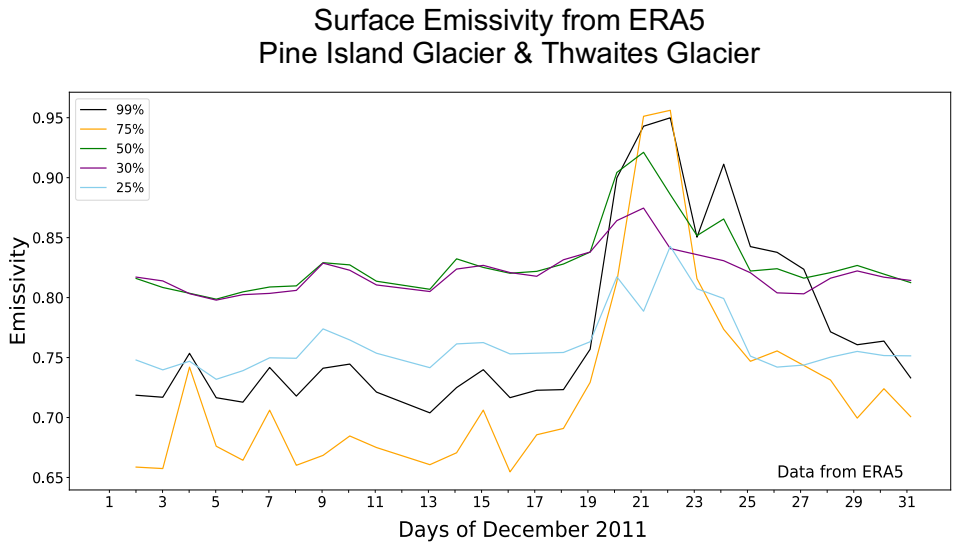

Figure 3.18: Surface emissivity calculated using ERA5 skin temperature for several individual grid cells corresponding to various individual percentiles from within the daily distributions shown at left. The percentiles specified in the legend are identified at the day of highest overall T_b (December 22).

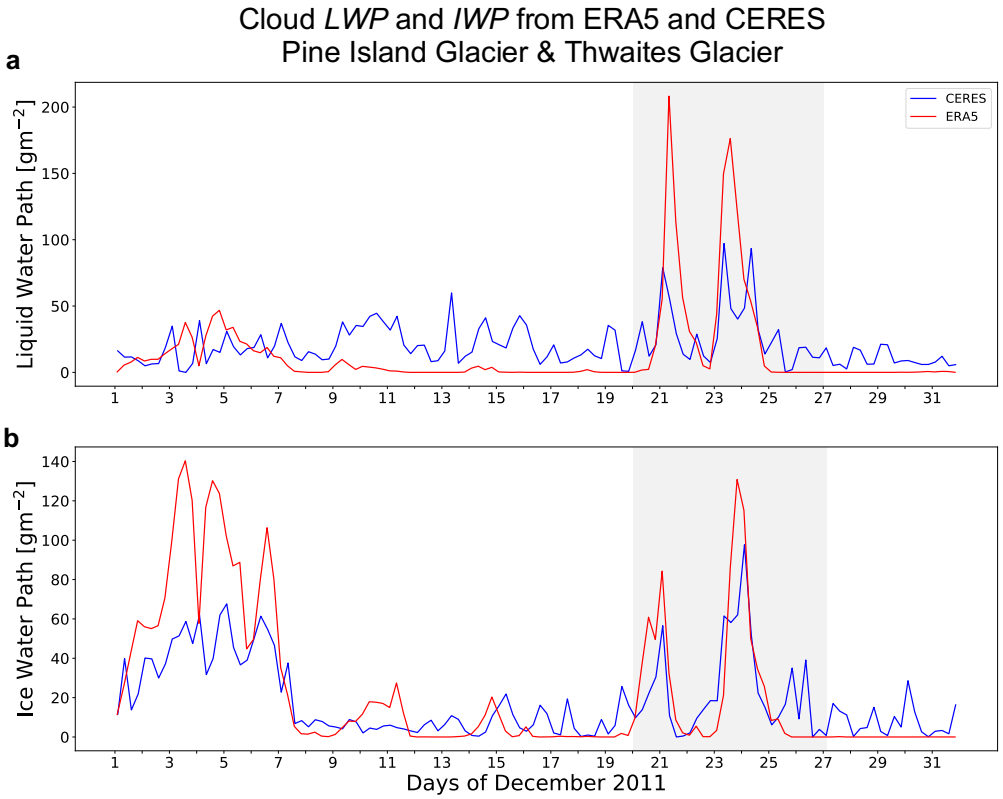

Figure 3.19: CERES retrievals over the Pine Island Glacier and Thwaites Glacier region over December 2011 (blue) and **(a)** ERA5 model estimates (red) of cloud liquid water path and **(b)** cloud ice water path.

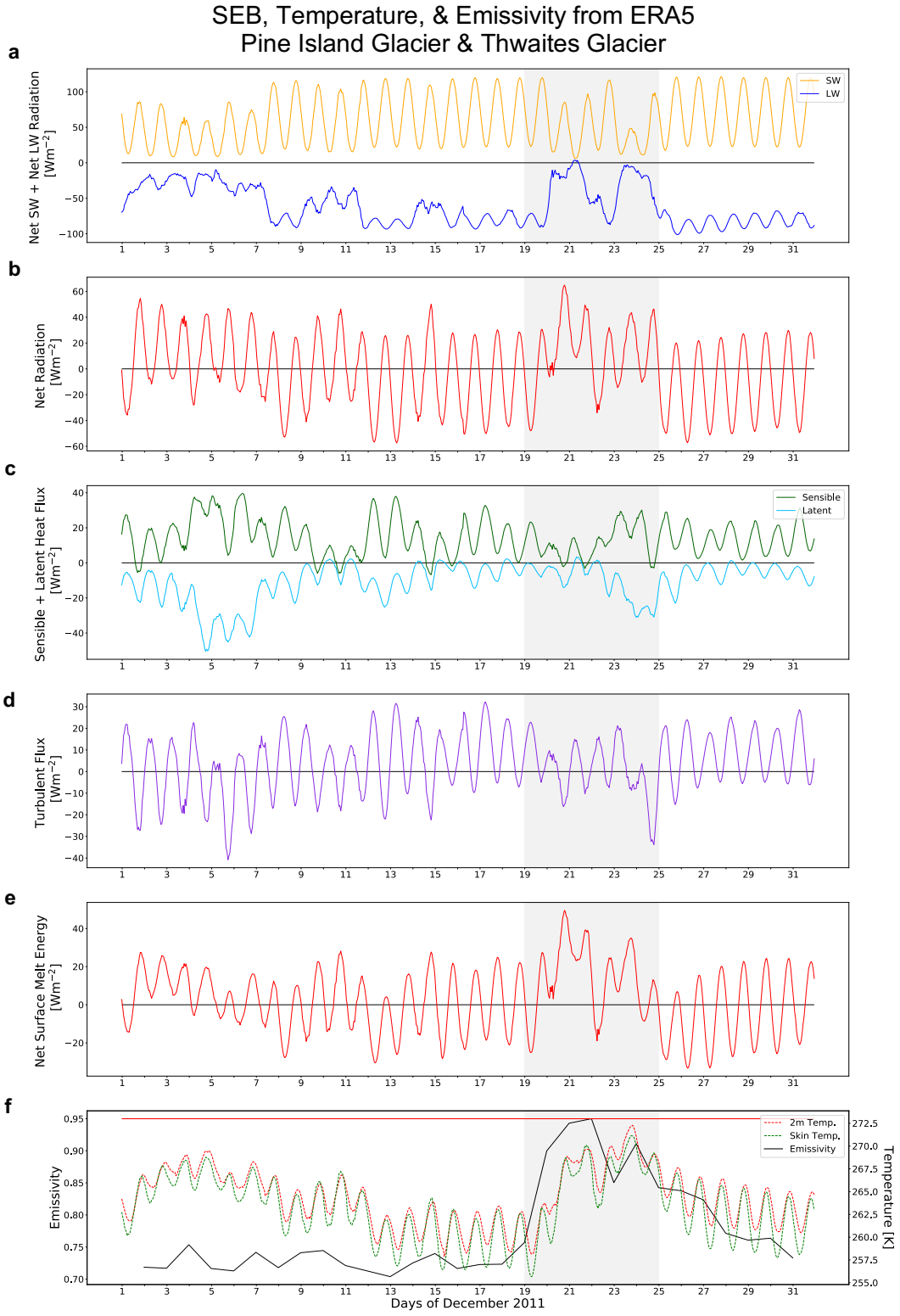

Figure 3.20: Spatially averaged time series of individual SEB components **(a-d)**, the total ME **(e)**, and the emissivity with 2 m temperature and skin temperature **(f)** over the Pine Island Glacier and Thwaites Glacier region in December 2011. The red line in **(f)** is the melting point (273 K). The light grey shading denotes the melt event.

3.3.2 January 2012

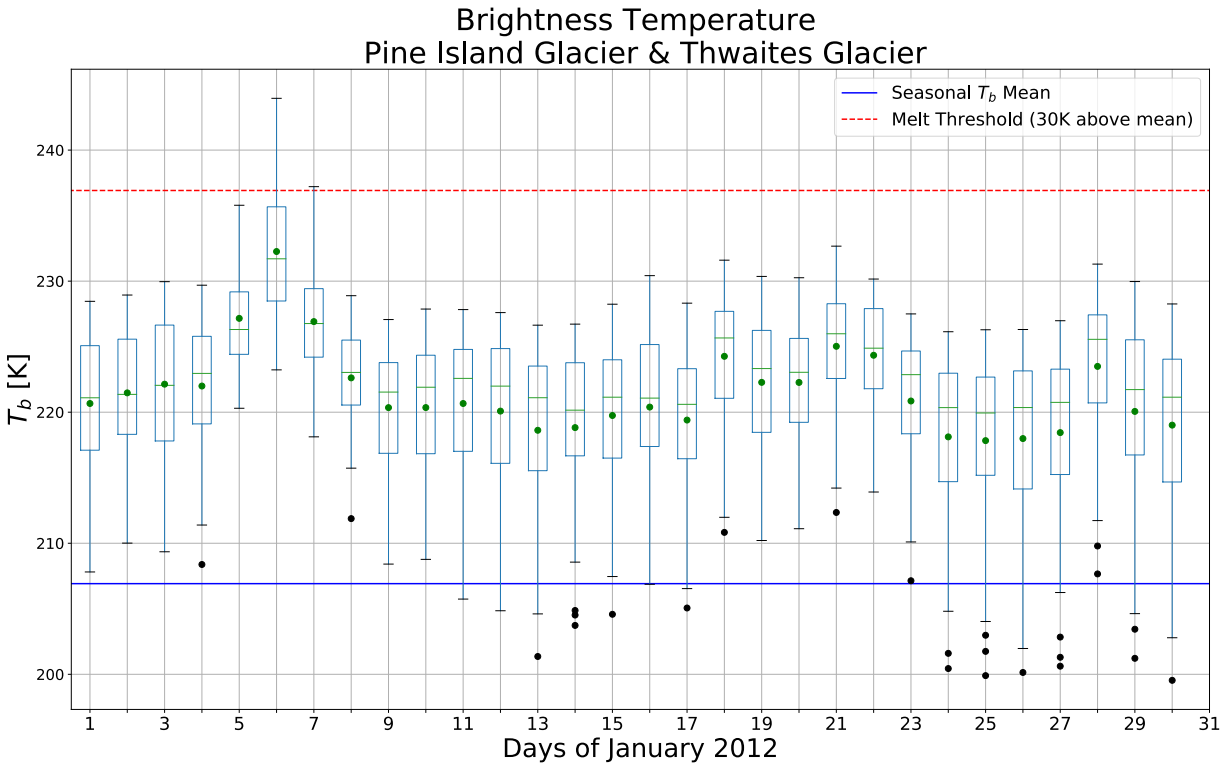

Figure 3.21: Box-and-whisker plot of daily 19 GHz-H T_b over the Pine Island Glacier and Thwaites Glacier region over January 2012; with the prior year cold season mean and 30 K common melt detection threshold shown by the blue and red lines, respectively.

The 19 GHz-H T_b indicates a melt event at Pine Island Glacier and Thwaites Glacier that peaks on 6 January 2012 and lasted about four days (Figure 3.21). Surface emissivity tends to be inhomogeneous and each gridded percentile varies by around 0.03 throughout the melt event as well as the entire month (Figure 3.22). Spatially-averaged time series of individual SEB components, net *ME*, and skin and 2 m temperature overlaid on the emissivity summarize the melt event (Figure 3.24). On 4 January, there is a drastic decrease in net SW radiation (diurnal cycle remains between 0 and 60 Wm^{-2}) (Figure 3.24 (a,b)). With this is a rapid increase in net LW radiation that sustains itself just below 0 Wm^{-2} for the entirety of the melt event (Figure 3.24

(a,b)). Turbulent fluxes during the time are mostly unchanging and the net melt radiation remains above 0 Wm^{-2} for the length of the melt period (Figure 3.24 (c,d)). There is an increase to almost above freezing temperatures in both skin and 2 m temperature (Figure 3.24 (f)). CERES *LWP* during this time from CERES shows values consistently below 50 gm^{-2} (Figure 3.23 (a)). CERES *IWP* increases during this period as well (Figure 3.23 (b)), although the representation of mixed-phase/ice clouds in both CERES and ERA5 has been questionable. It is likely that liquid-dominant and possibly mixed-phase thin clouds moved in from the northeast around 4 January when we see a peak in *LWP* values to possibly simulate a warming event similar to the Bennartz et al. [2013] thin cloud all-wave radiative effect observed at Siple Dome in January 2015.

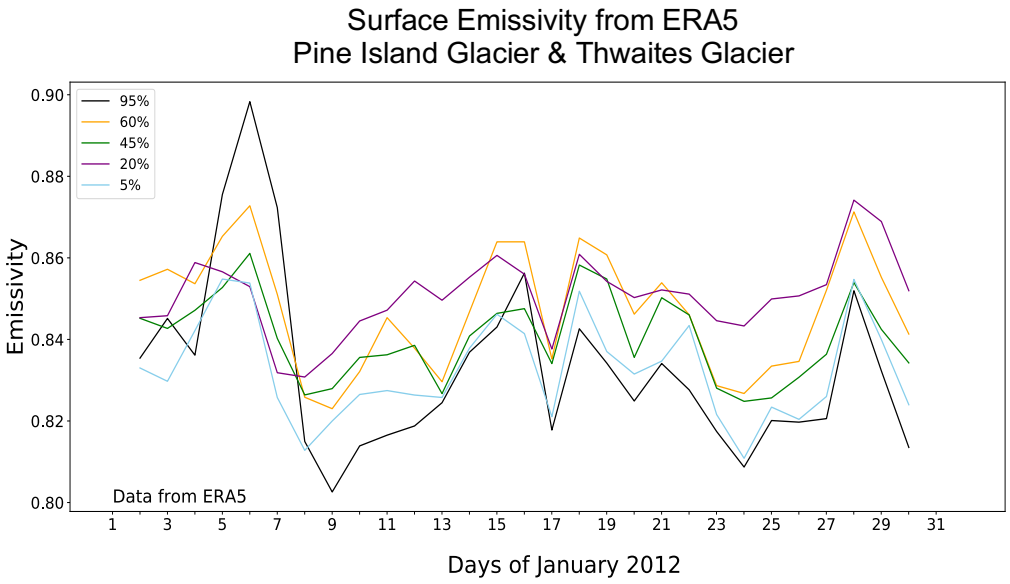

Figure 3.22: Surface emissivity calculated using ERA5 skin temperature for several individual grid cells corresponding to various individual percentiles from within the daily distributions shown at left. The percentiles specified in the legend are identified at the day of highest overall T_b (January 6).

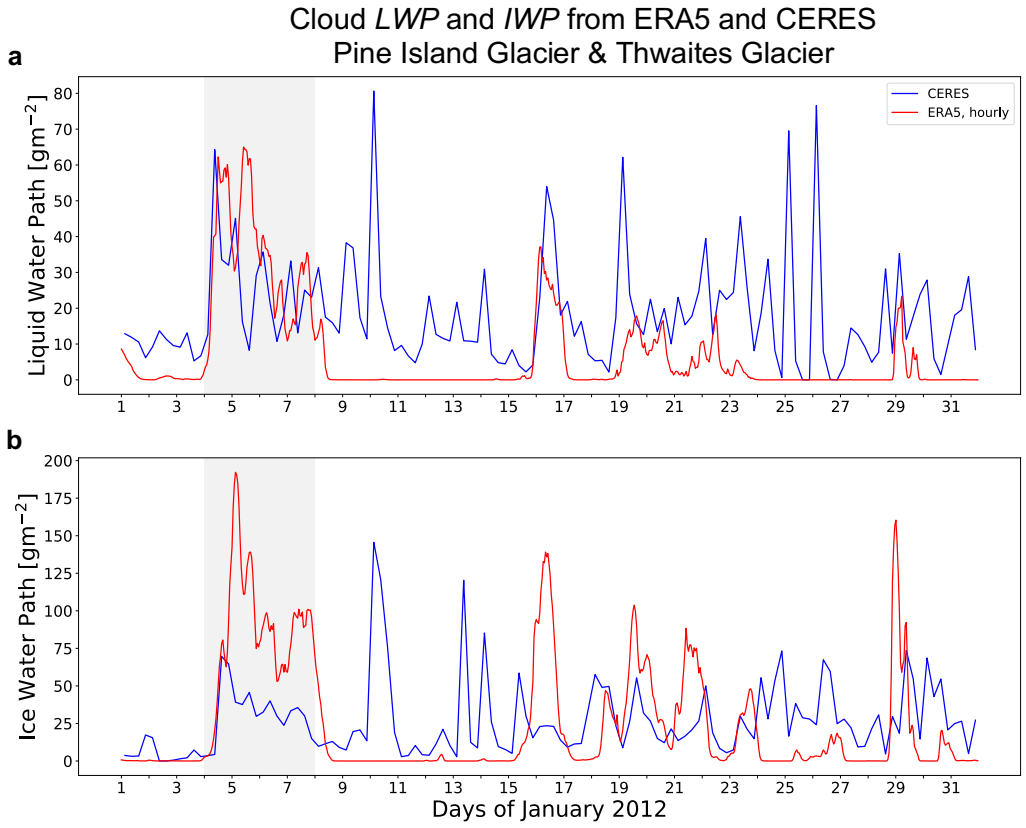

Figure 3.23: CERES retrievals over the Pine Island Glacier and Thwaites Glacier region over January 2012 (blue) and **(a)** ERA5 model estimates (red) of cloud liquid water path and **(b)** cloud ice water path over the Pine Island.

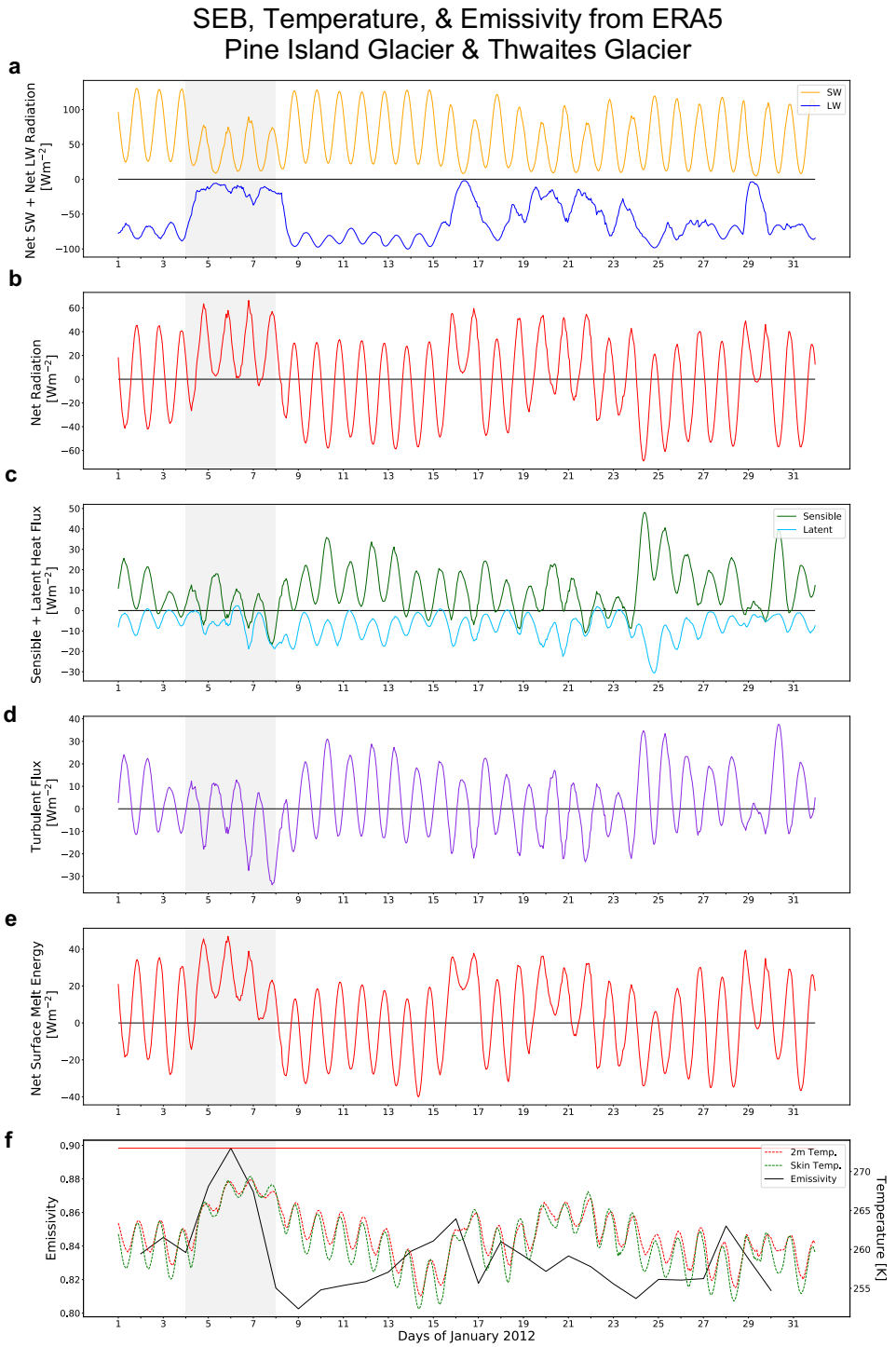

Figure 3.24: Spatially averaged time series of individual SEB components **(a-d)**, the total ME **(e)**, and the emissivity with 2 m temperature and skin temperature **(f)** over the Pine Island Glacier and Thwaites Glacier region in January 2012. The red line in **(f)** is the melting point (273 K). The light grey shading denotes the melt event.

3.3.3 February 2013

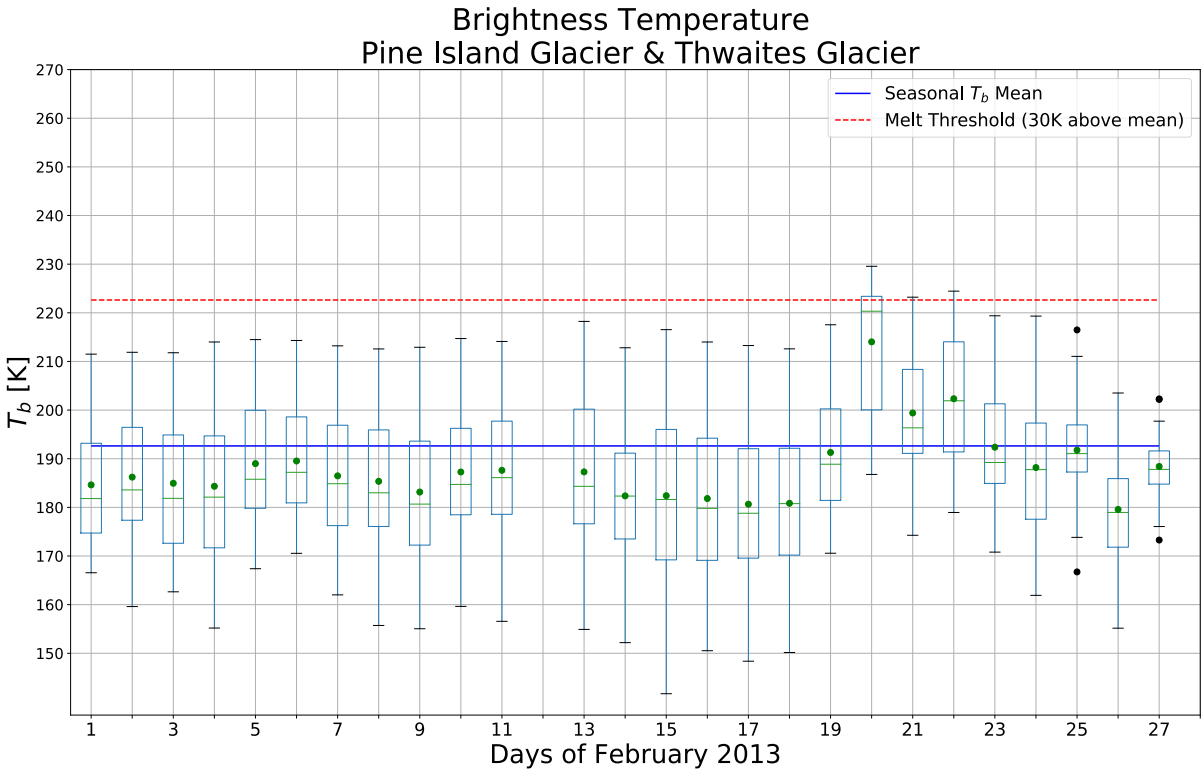

Figure 3.25: Box-and-whisker plot of daily 19 GHz-H T_b over the Pine Island Glacier and Thwaites Glacier region over February 2013; with the prior year cold season mean and 30 K common melt detection threshold shown by the blue and red lines, respectively.

The Pine Island and Thwaites Glacier region experienced melt late in austral summer 2013 (19 February through 23 February; Figure 3.25). As seen in the other Pine Island Glacier and Thwaites Glacier cases, the difference in emissivity for each percentile represents the inconsistency in the topographical surface (Figure 3.26). Around 20 February, the CERES *LWP* rises to around 50 gm^{-2}, indicating some cloud presence, which most likely initiated the melt (Figure 3.27 (a)). On 19 February, net SW radiation decreases to a consistent value of 20 Wm^{-2} and net LW radiation reached positive values of about 18 Wm^{-2} over the melt period (Figure 3.28

(a,b)). Surface sensible heat flux increased significantly to between 80 and 100 Wm^{-2} on February 19 (Figure 3.28 (c,d)), pushing the net surface *ME* to sustain a positive value through the diurnal cycle for 3 days (Figure 3.28 (e)). It is probable that optically thick, moist clouds sustained presence over the region, inciting the melt, and it was lengthened by the indicated sensible heat impulse. During the large increase in sensible heat flux, surface temperatures increased from around 250 K to about 272 K over 18 hours (Figure 3.28 (f)).

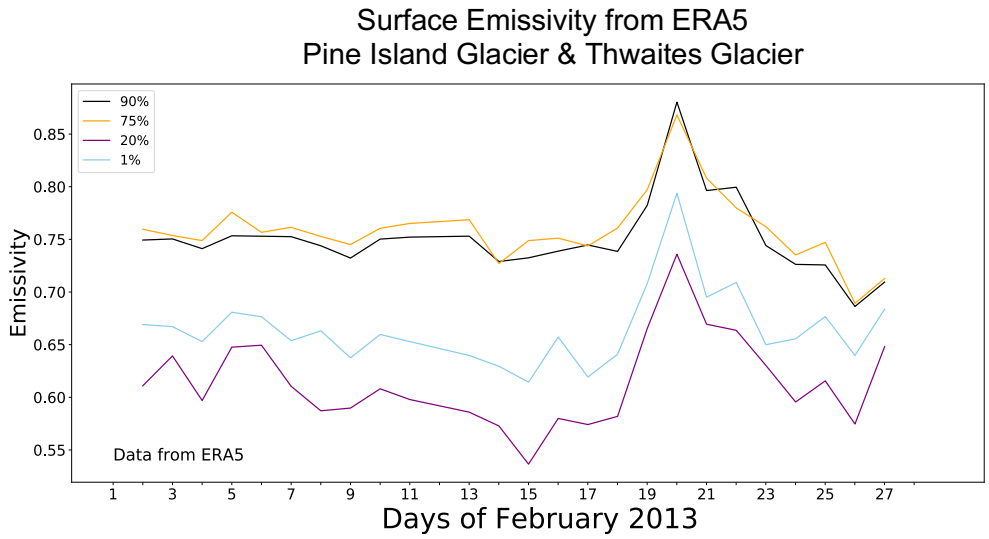

Figure 3.26: Surface emissivity calculated using ERA5 skin temperature for several individual grid cells corresponding to various individual percentiles from within the daily distributions shown at left. The percentiles specified in the legend are identified at the day of highest overall T_b (February 20).

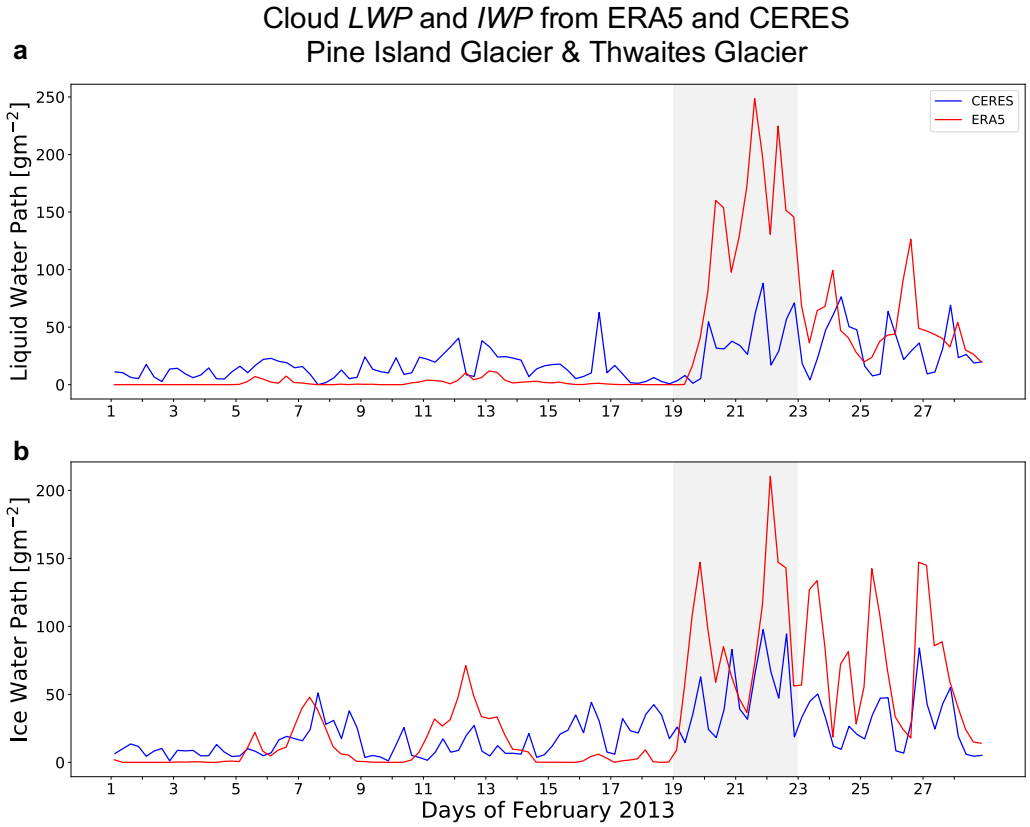

Figure 3.27: CERES retrievals over the Pine Island Glacier and Thwaites Glacier region for February 2013 (blue) and **(a)** ERA5 model estimates (red) of cloud liquid water path and **(b)** cloud ice water path.

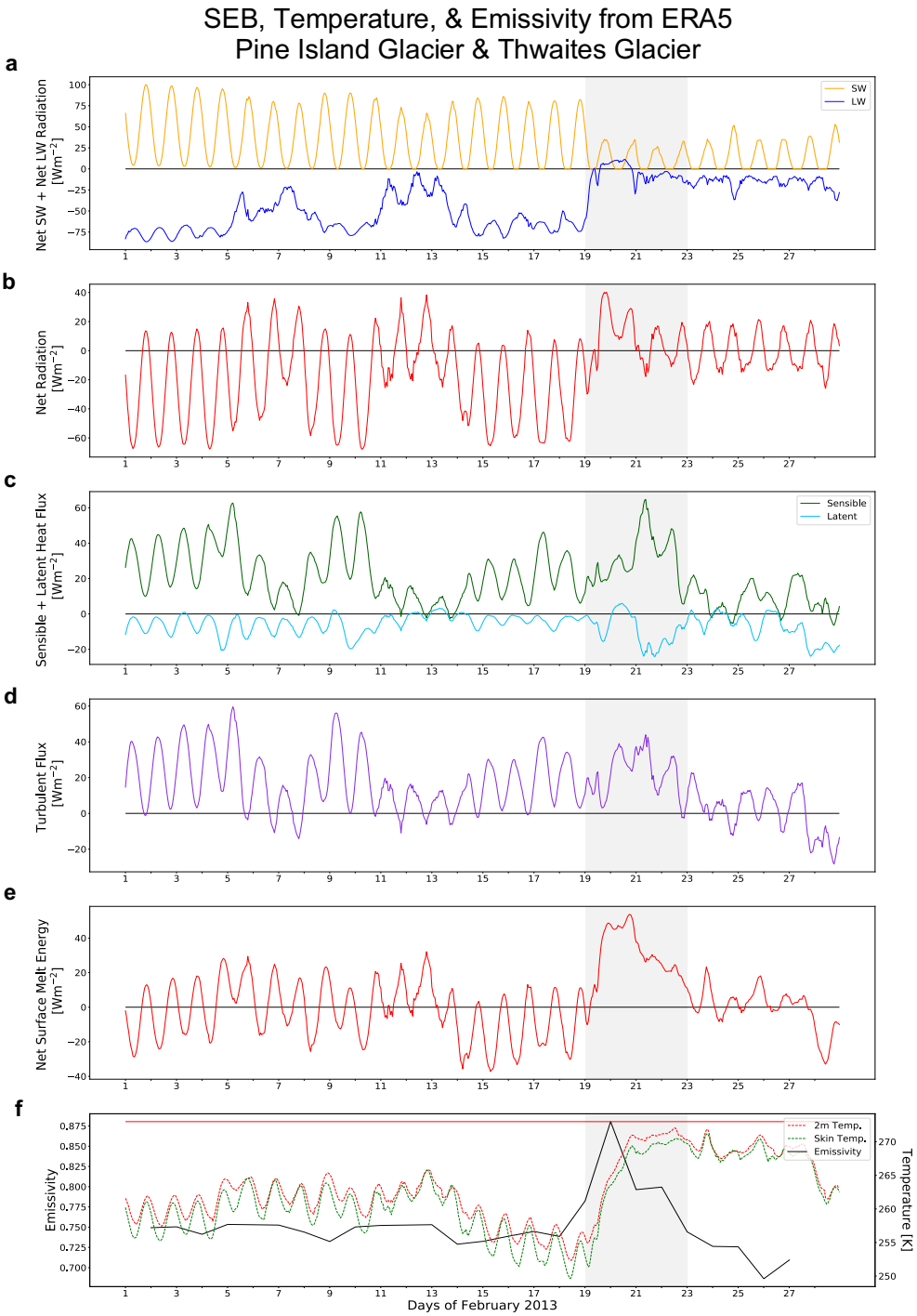

Figure 3.28: Spatially averaged time series of individual SEB components **(a-d)**, the total ME **(e)**, and the emissivity with 2 m temperature and skin temperature **(f)** over the Pine Island Glacier and Thwaites Glacier region in February 2013. The red line in **(f)** is the melting point (273 K). The light grey shading denotes the melt event.

3.4 Ross Ice Shelf

3.4.1 December 2011

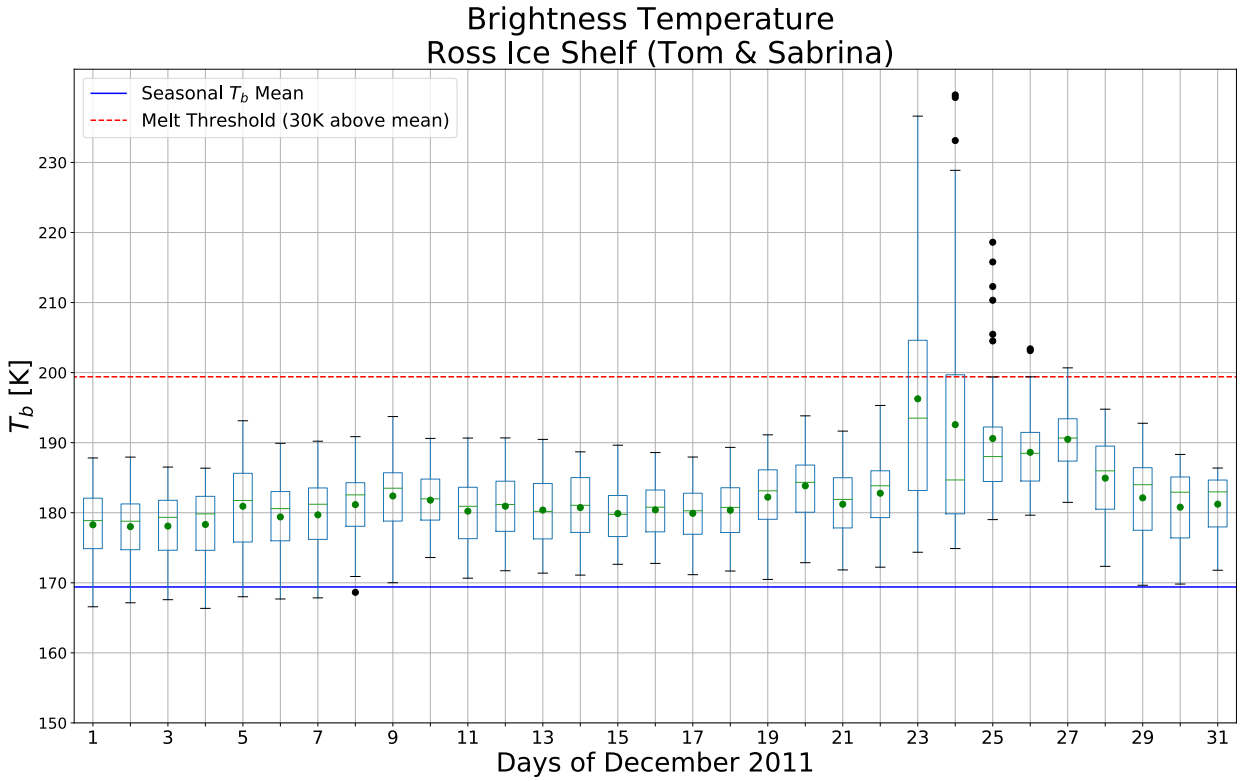

Figure 3.29: Box-and-whisker plot of daily 19 GHz-H T_b over Ross Ice Shelf region over December 2011; with the prior year cold season mean and 30 K common melt detection threshold shown by the blue and red lines, respectively.

The southern Ross Ice Shelf, along the base of the Transantarctic Mountains, experienced melt from 19 December 2011 to 23 December 2011 (Figure 3.29). The emissivity seen here shows less disparity between the percentiles (all percentiles are between 0.64 and 0.72, pre-melt) suggesting this is a more uniform surface (Figure 3.30). Spatially-averaged time series of individual SEB components, total *ME*, and skin and 2 m temperature summarize the melt event (Figure 3.32). A decrease in the amplitude of net SW radiation (minimum diurnal value shifts from around 40 Wm^{-2} to 20 Wm^{-2} during the predicted melt; maximum diurnal value shifts from

95 Wm^{-2} to around 70 Wm^{-2}) is evident during this period, as well as an increase in net LW radiation to about -10 Wm^{-2} (Figure 3.32 (a,b)). Surface sensible heat flux rises on 19 December in conjunction with skin temperature and wind speed (Figure 3.32 (c,d)). In addition to this, the latent heat flux experiences large positive impulses (Figure 3.32 (c,d)). Starting the day before melt is observed, winds originating in the southeast rise from a trivial speed of around 2 ms^{-1} to about 14 ms^{-1} (Figure 3.31). Wind originating from this direction must first pass over the Transantarctic Mountains and descend on the leeward side of the mountain range, representative of a föhn wind event that drove up surface temperatures and ultimately resulted in surface melting. From the CERES *LWP*, there does not appear to be any consistent cloud presence during the time (Figure 3.33 (a)). To completely resolve this case, higher resolution data would be useful for interpreting the exact drivers and surface conditions, as it appears ERA5 is missing small-scale terrain forcing and underestimating certain values like the sensible heat flux.

To corroborate the ERA5 and CERES data, we used observations from the Tom and Sabrina AWSs (Figure 3.34; Figure 3.35). Both Tom and Sabrina AWSs show surface temperatures elevating to above the melting point. This occurred just after wind speed is increases to above 15 ms^{-1}. The AWSs show a southeast origin of wind direction.

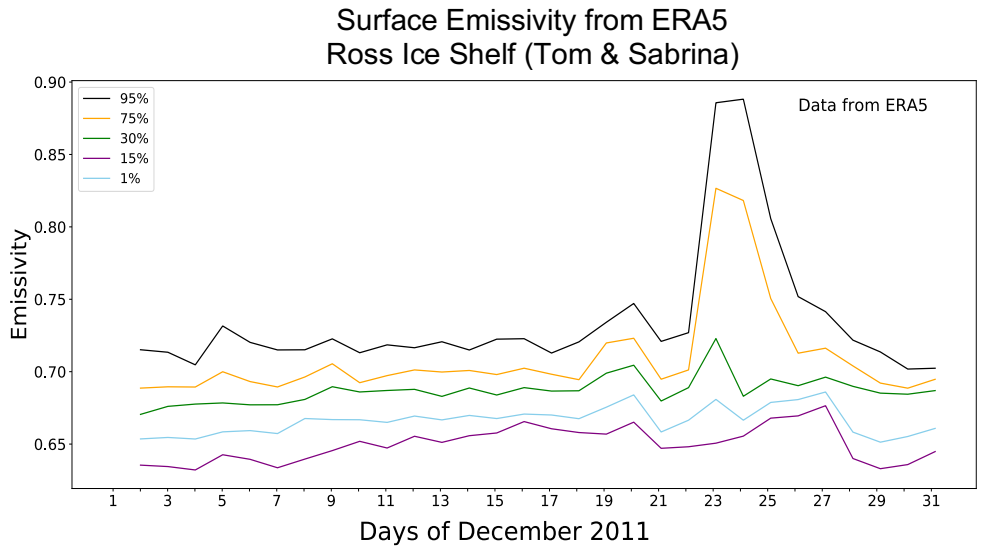

Figure 3.30: Surface emissivity calculated using ERA5 skin temperature for several individual grid cells corresponding to various individual percentiles from within the daily distributions shown at left. The percentiles specified in the legend are identified at the day of highest overall T_b (December 23).

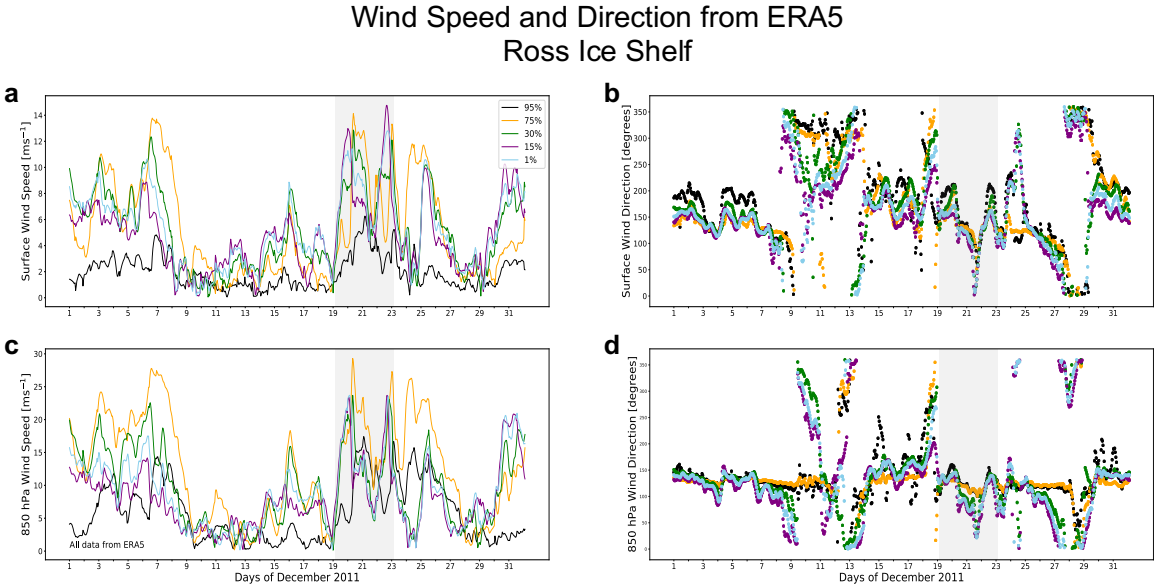

Figure 3.31: ERA5 meteorological output over the Ross Ice Shelf region for December 2011, for the individual grid cells identified in Figure 3.26: (a) Surface wind speeds, (b) surface wind direction (origin of wind), (c) 850 hPa wind speed, and (d) 850 hPa wind direction. Light grey shading indicates the timing of the melt event.

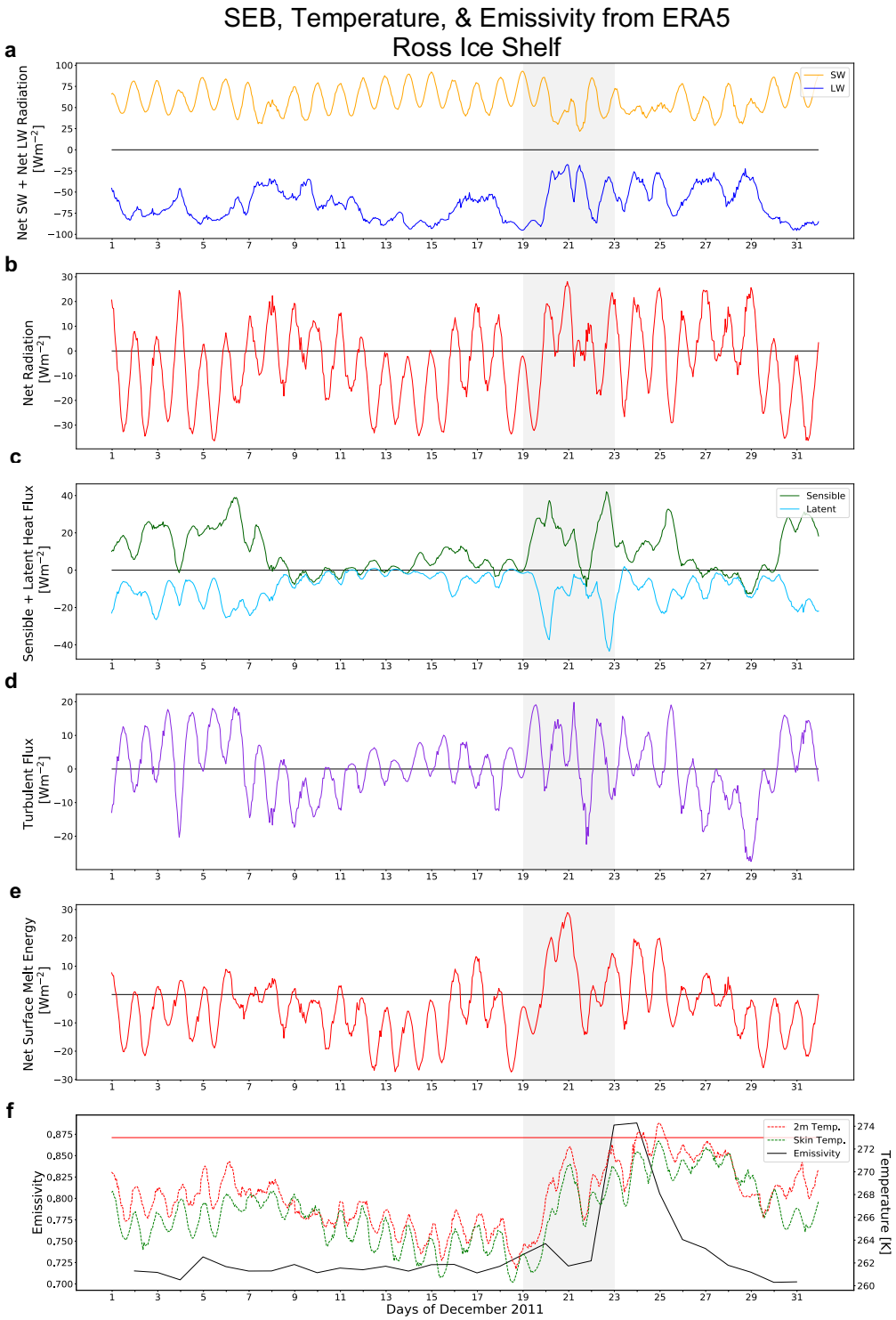

Figure 3.32: Spatially averaged time series of individual SEB components **(a-d)**, the total ME **(e)**, and the emissivity with 2 m temperature and skin temperature **(f)** over the Ross Ice Shelf region in December 2011. The red line in **(f)** is the melting point (273 K). The light grey shading denotes the melt event.

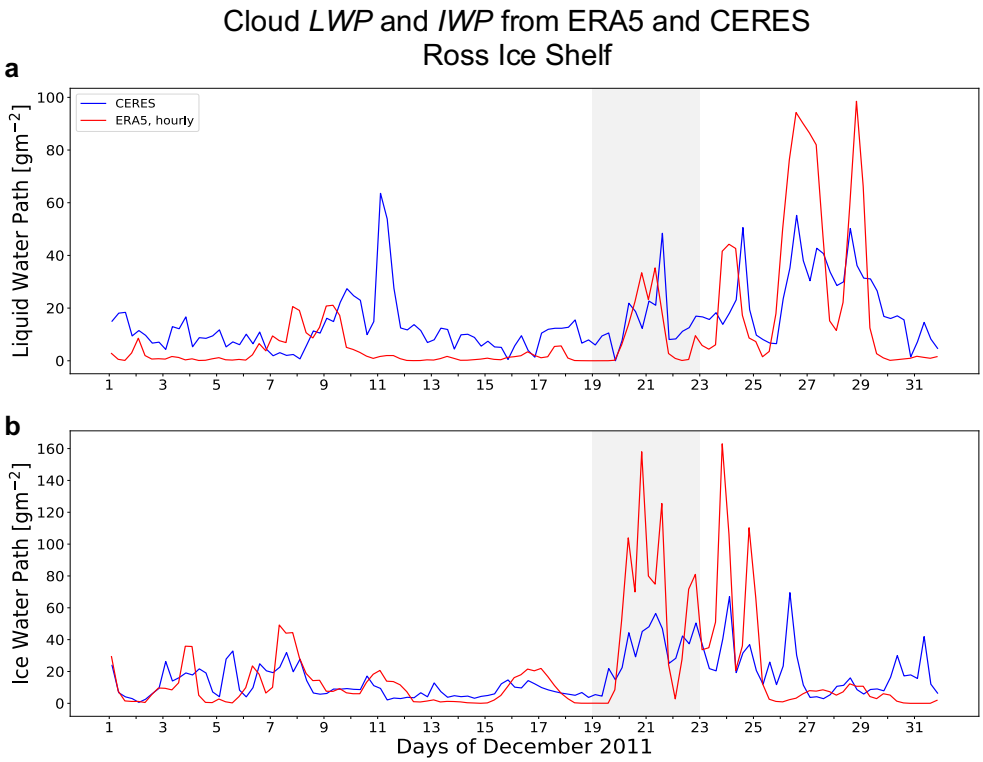

Figure 3.33: CERES retrievals over the Ross Ice Shelf region for December 2011 (blue) and **(a)** ERA5 model estimates (red) of cloud liquid water path and **(b)** cloud ice water path.

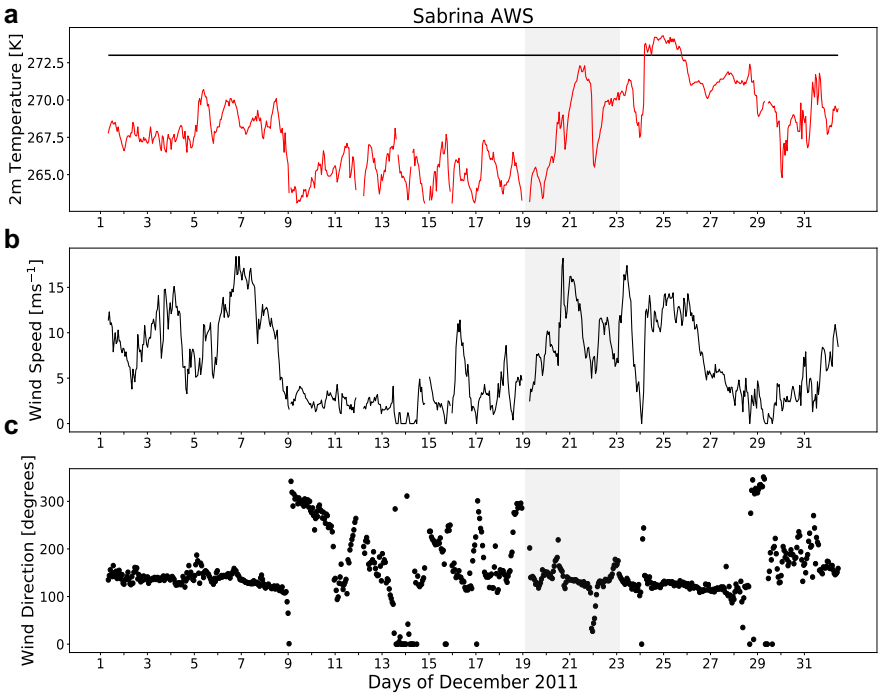

Figure 3.34: *AWS-14 data recorded over December 2011*: (a) Hourly 2 m temperature, (b) surface wind speed, and (c) surface wind direction. Light grey shading indicates the melt event.

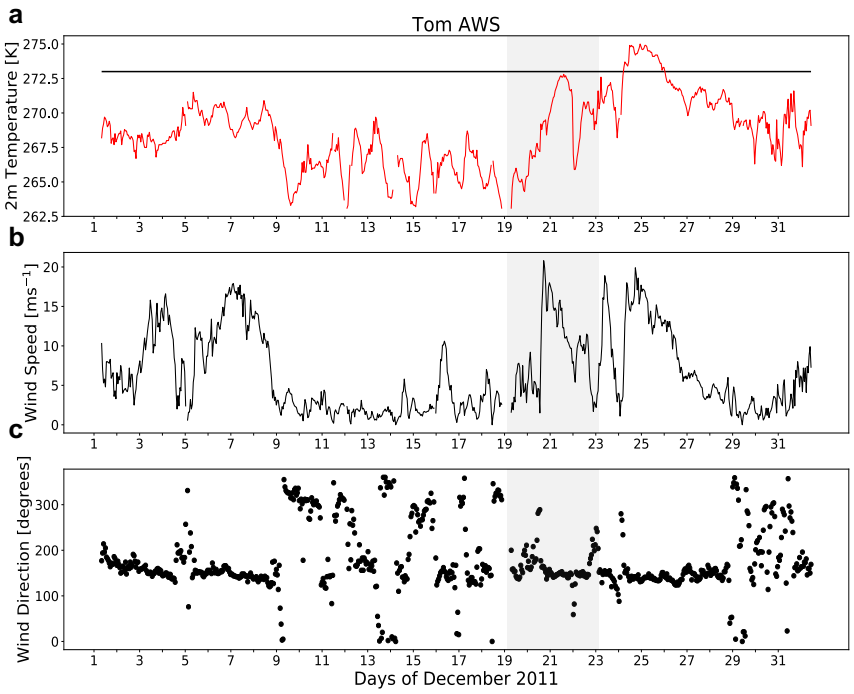

Figure 3.35: *AWS-14 data recorded over December 2000*: **(a)** Hourly 2 m temperature, **(b)** surface wind speed, and **(c)** surface wind direction (**c)** from the Tom AWS in December 2011. Light grey shading denotes the melt event.

3.5 Larsen C Ice Shelf

3.5.1 December 2000

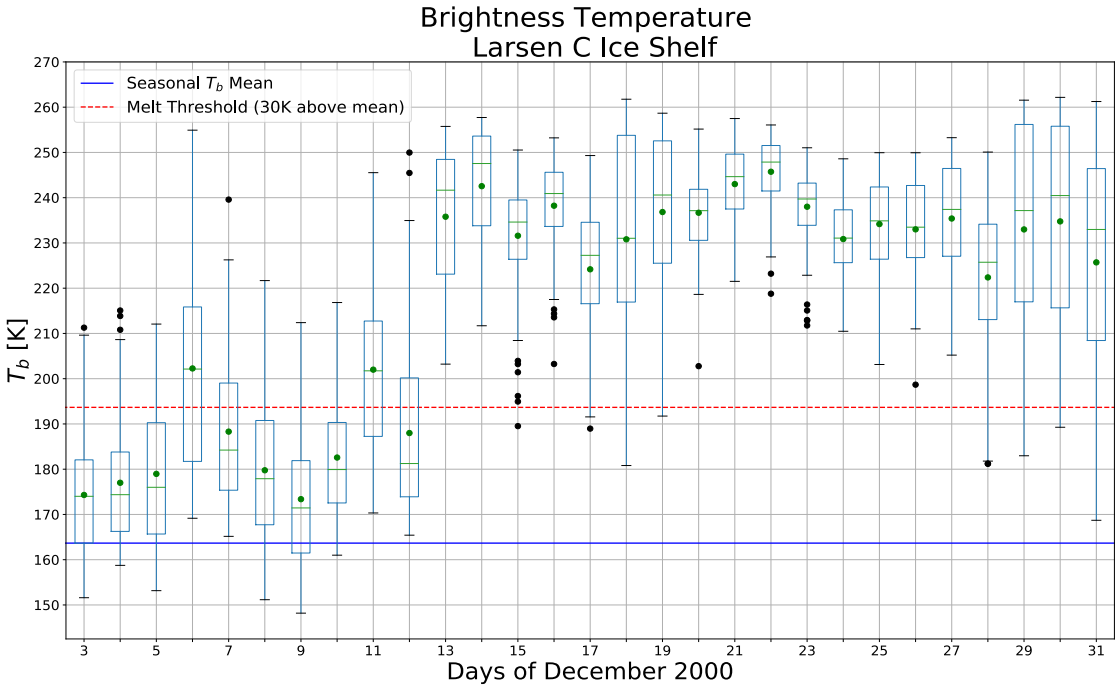

Figure 3.36: Box-and-whisker plot of daily 19 GHz-H T_b over the Larsen C Ice Shelf region over December 2000; with the prior year cold season mean and 30 K common melt detection threshold shown by the blue and red lines, respectively.

On the LCIS elevated T_b indicated significant surface melt from 16 December 2000 to 20 December 2000 (Figure 3.36). The LCIS melts consistently throughout most of the austral summer, but it may not always be driven by thermal blanketing incited by cloud presence. In this case we will look at a possible föhn wind event, when cloud *LWP* indicates almost no cloud coverage while melt is occurring in conjunction with elevated wind speeds originating from the western side of the AP.

The distribution of melt on the LCIS and is evidence that elevated T_b is concentrated at the base of the mountains (Figure 3.37). Starting on 16 December, net SW radiation decreases

slightly, but not significantly (maximum diurnal SW value decreases to 120 Wm^{-2} from about 180 Wm^{-2}) (Figure 3.40 (a,b)). Net LW radiation rises to just below 0 Wm^{-2} over this period (Figure 3.40 (a,b)). The net surface radiation is brought closer to 0 Wm^{-2} and the net surface melt energy is positive from the 16 to 19 December (Figure 3.40 (a,b)). The skin and 2 m temperatures rise to above freezing on 16 December and remain in that range for the entirety of the melt period (Figure 3.40 (f)). Surface wind speeds peak to around 8 ms^{-1} on 16 December and stay elevated until 19 December (Figure 3.39). During this time, the wind direction shifted from easterly to north/northwest. The direction of wind origin shows the wind would be passing over the AP mountain range and descending down onto the LCIS. Cloud *LWP* from ERA5 and CERES show varied and little liquid cloud presence with values ranging from just under 20 gm^{-2} to 0 gm^{-2} (Figure 3.41).

AWS-14 data recorded over December 2000 corroborates ERA5 data discussed in this section (Figure 3.42). The wind speed peaks to about 8 ms^{-1}, while the origin direction is predominantly northerly. The 2 m temperature remains consistently above the melting point throughout the month, and during the suggested föhn wind event.

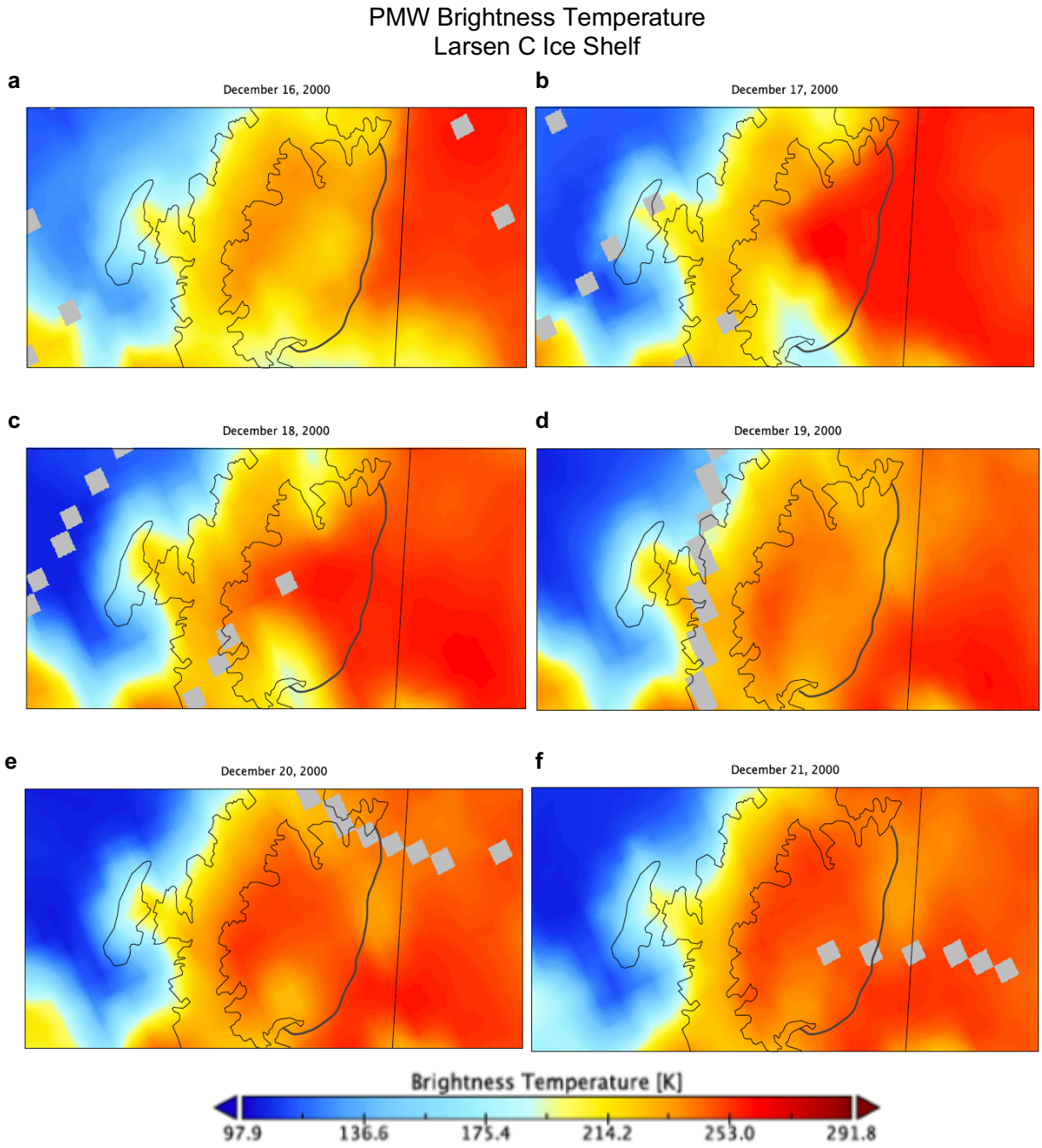

Figure 3.37: Progression of PMW-derived T_b over Larsen C Ice Shelf from 16 to 21 December 2000.

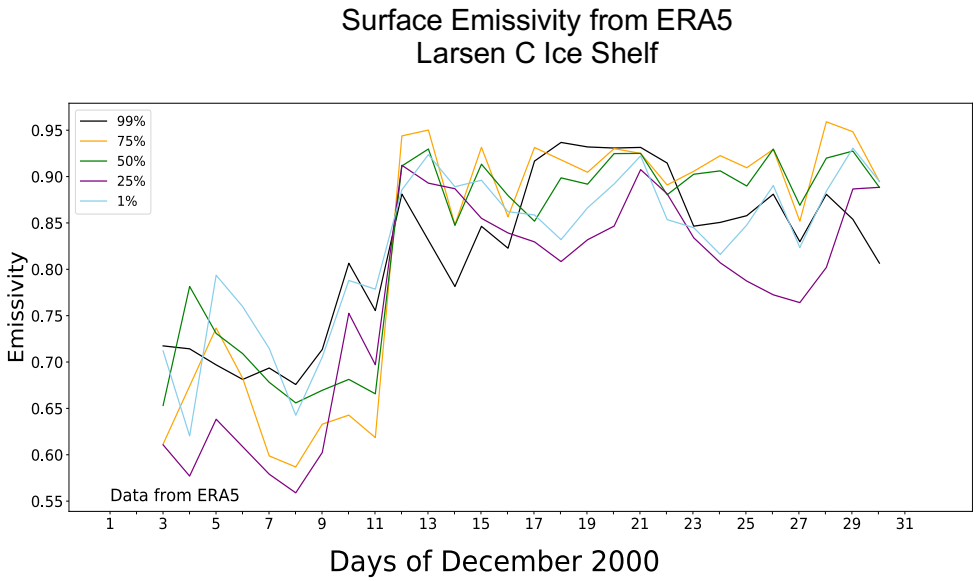

Figure 3.38: Surface emissivity calculated using ERA5 skin temperature for several individual grid cells corresponding to various individual percentiles from within the daily distributions shown at left. The percentiles specified in the legend are identified at the day of highest overall T_b (December 19).

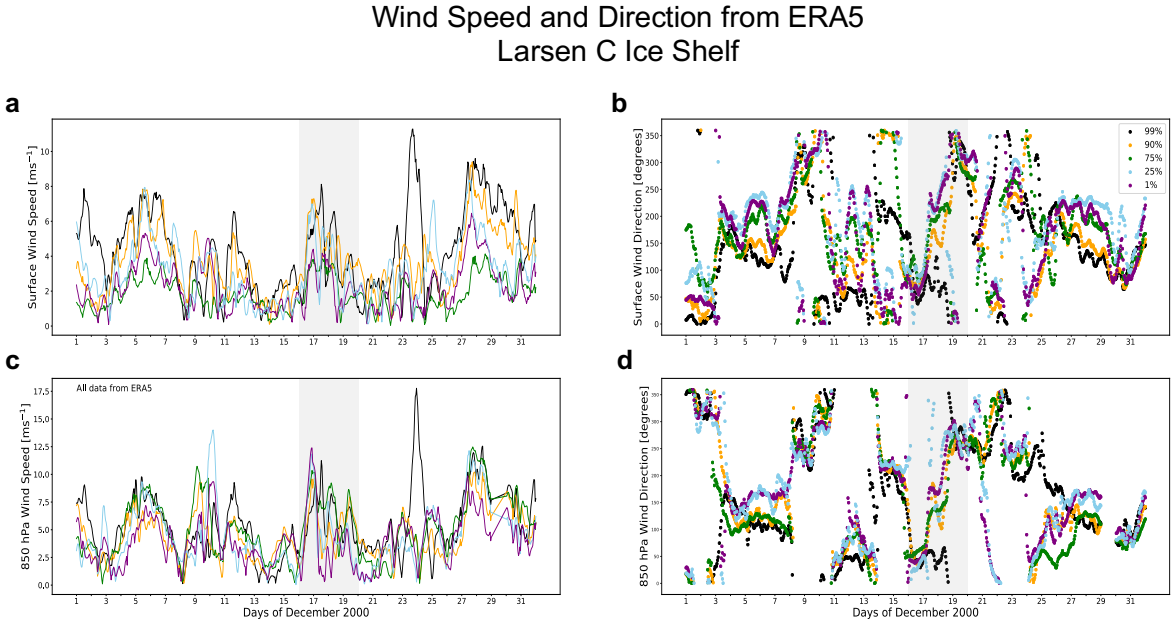

Figure 3.39: ERA5 meteorological output over the Larsen C Ice Shelf region for December 2011, for the individual grid cells identified in Figure 3.34: **(a)** Surface wind speeds, **(b)** surface wind direction (origin of wind), **(c)** 850 hPa wind speed, and **(d)** 850 hPa wind direction. Light grey shading indicates the timing of the melt event.

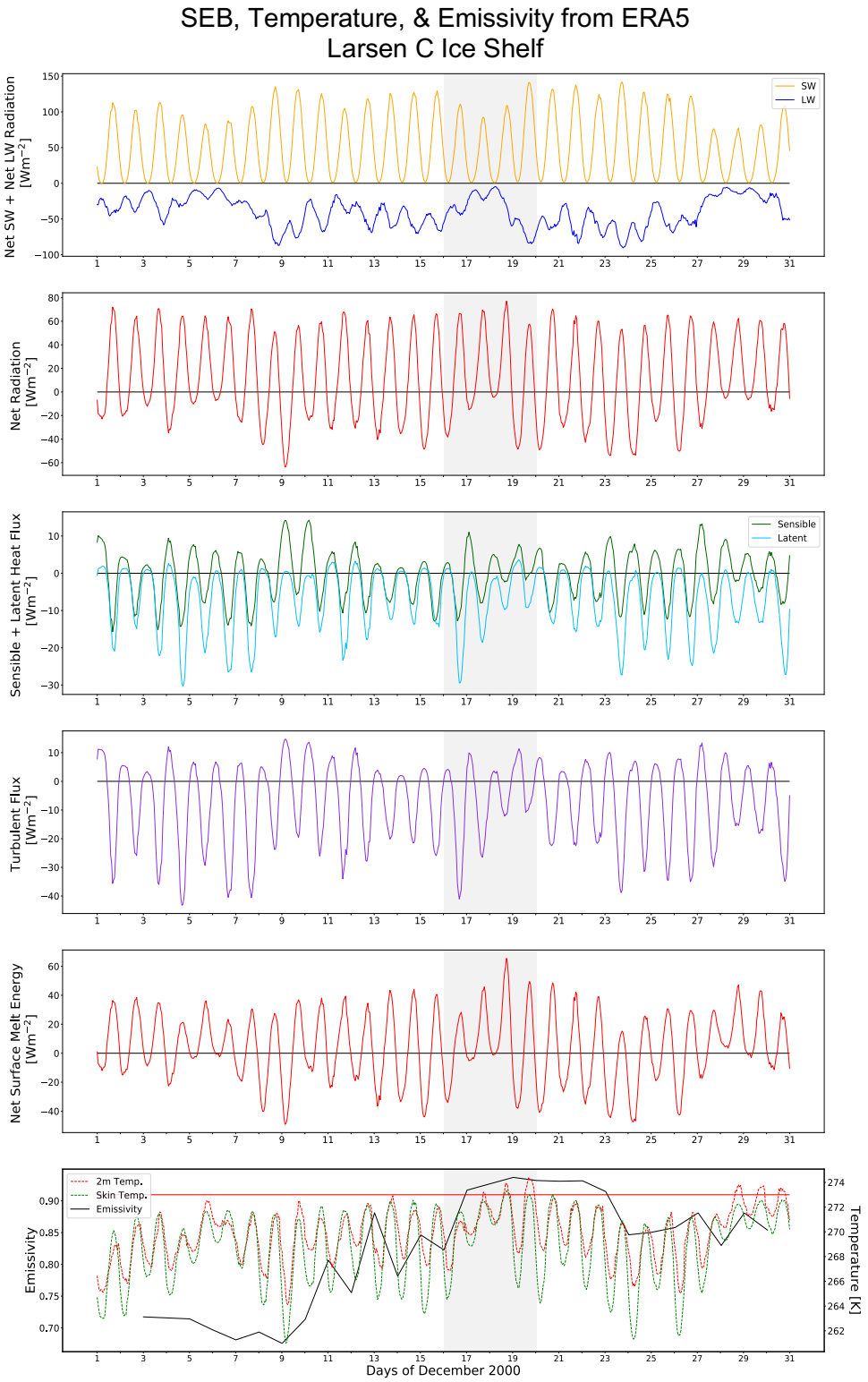

Figure 3.40: Spatially averaged time series of individual SEB components **(a-d)**, the total ME **(e)**, and the emissivity with 2 m temperature and skin temperature **(f)** over the LCIS in December 2000. The red line in **(f)** is the melting point (273 K). The light grey shading denotes the melt event in this case.

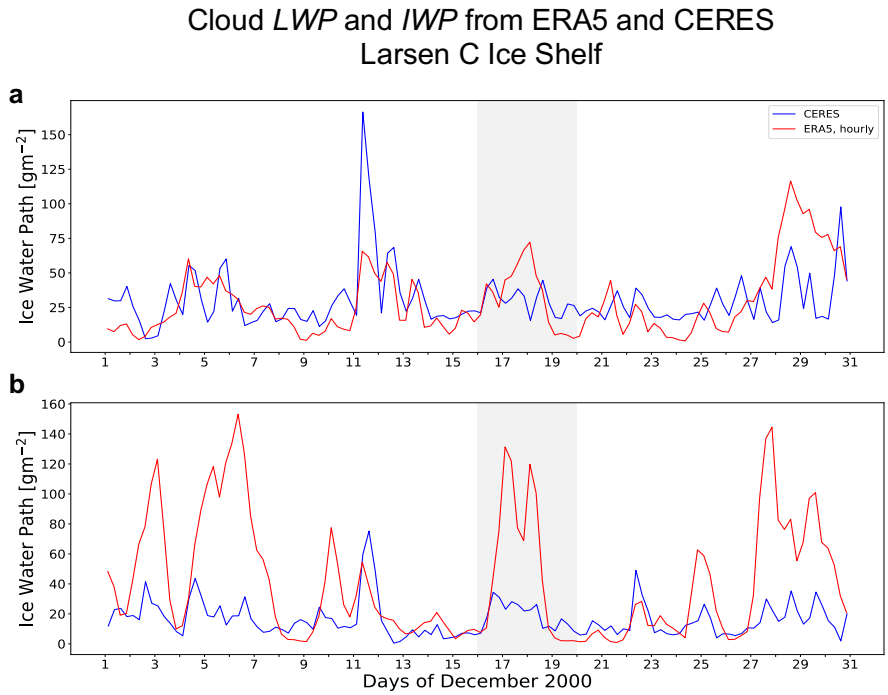

Figure 3.41: CERES retrievals over the Larsen C Ice Shelf region for December 2000 (blue) and **(a)** ERA5 model estimates (red) of cloud liquid water path and **(b)** cloud ice

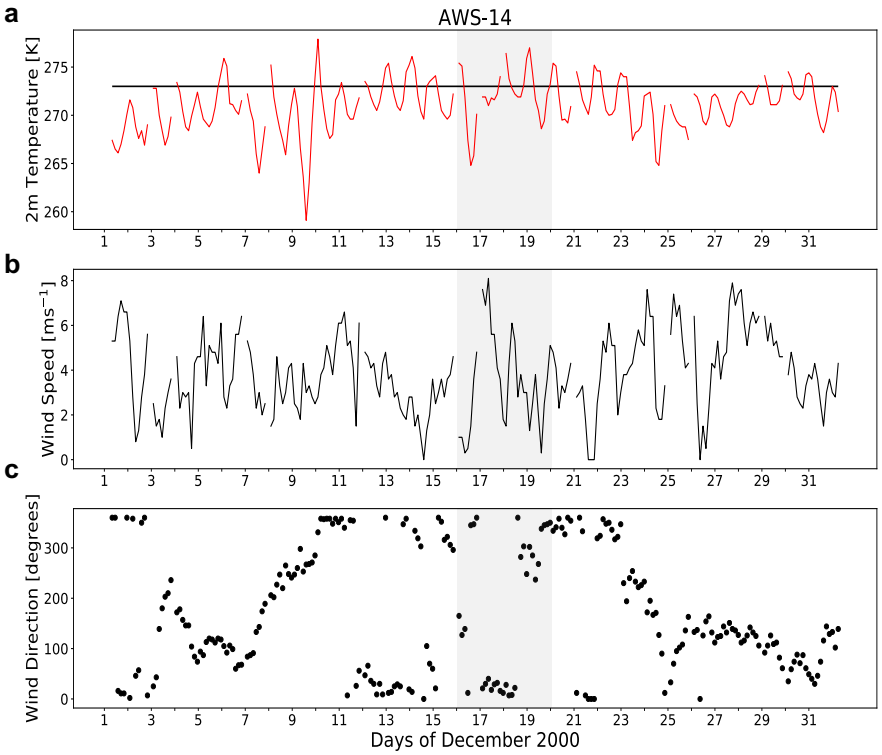

Figure 3.42: *AWS-14 data recorded over December 2000*: **(a)** Hourly 2 m temperature, (**b)** surface wind speed, and **(c)** surface wind direction. Light grey shading indicates the timing of the suspected föhn wind event.

Chapter 4

Discussion

The discussion is categorized by the four main melt drivers that we observed influencing surface melt in our case studies. We first discuss thermal blanketing as a result from optically thick clouds. This type of melt regime was seen in January 2016 as a result of a more extreme atmospheric river event, as well as in more normal climatological conditions that also produced optically thick clouds in Pine Island Glacier and Thwaites Glacier in December 2011 and February 2013. We then move on to discuss thin, low-lying liquid dominant clouds driving surface melt in cases at Siple Dome in January 2015 and Pine Island and Thwaites Glacier in January 2012. We then look at sensible heat flux preconditioning the ice surface for surface melting. We saw evidence of this in the Siple Dome 2011 case, and potentially aiding melt in the Pine Island Glacier and Thwaites Glacier case in February 2013. Lastly, we discuss föhn wind events causing surface melt observed on the Ross Ice Shelf in December 2011 and the Larsen C Ice Shelf in December 2000.

4.1 Thermal Blanketing from Optically Thick Clouds

During the AWARE campaign in January 2016 at WAIS Divide, a large atmospheric river event pushed a warm, moist airmass over the WAIS [Nicolas et al., 2017]. This was observed driving surface melt across WAIS Divide. By looking at the same time period at lower elevation, data from the similarly homogenous surface (low surface variability) of Siple Dome

confirms that this airmass composed of liquid dominant, optically thick clouds drove extreme melt observed elsewhere on the WAIS. The three consequences of optically thick clouds, as they impact surface melt, are: (i) a large decrease in SW radiation such that very little reaches the surface; (ii) a large increase in LW downwelling radiation, with the net surface LW radiation very near zero, as the optically thick clouds act essentially as a blackbody emitting radiation towards the surface; (iii) and an increase in *LWP* above 50 gm^{-2}. Siple Dome in January 2016 saw all three of these components, as well as extremely elevated T_b. This case validates our reanalysis and satellite data, as it shows the same airmass we knew to be present over a majority of the WAIS during this time.

Pine Island and Thwaites Glacier in December 2011 and February 2013 experienced similar climatological conditions as in January 2016, though most likely not as extreme. The Amundsen Sea Embayment often experiences these warm airmass intrusions from low-pressure systems driving air eastward over the WAIS, first reaching the Amundsen Sea Embayment [Turner et al., 2016]. Pine Island and Thwaites Glacier in December 2011 saw net LW radiation reach positive values on 21 December that occurred as net SW radiation saw a decrease in amplitude, though it was not totally extinguished. *LWP* during the melt event peaked to values greater than 50 gm^{-2} for the entirety of the melt event, indicating optically thick, liquid cloud presence.

In February 2013, Pine Island and Thwaites Glacier saw a slightly more prominent rise in T_b that is uncharacteristically large so late in the melt season. Similar to the case of December 2011, a decrease in net SW radiation and rise in net LW radiation were shown, along with a *LWP* value that remains above 50 gm^{-2} for the melt period. Most notable for this case is that there is an increase in sensible heat flux on 21 February. The melt in this case was initiated by the presence

of optically thick, liquid dominant clouds, but may have been prolonged by this increase in sensible heat driving up surface temperatures.

In comparing both the Siple Dome and Pine Island and Thwaites Glacier cases, it is important to note the differences in emissivity in both geographically distinct regions. The surface emissivity at Siple Dome is consistent with a homogenous surface and generally melts uniformly. At Pine Island and Thwaites Glacier, the horizontal surface inhomogeneity is evident in the vaster differences in surface emissivity prior to and after the melt events, and the melt therefore is not uniform across the ice surface. Because of these differences in surface homogeneity, it is important to acknowledge the impact that small-scale surface forcing can have on detectability of melt and melt drivers.

4.2 Thin, Low-Level Liquid Clouds

Thin, low-level, liquid dominant clouds are often observed driving surface melt in Greenland, as shown by Bennartz et al. [2013]. Low-lying clouds that are optically thick enough to enhance downwelling LW radiation, yet thin enough to allow downwelling SW radiation to reach the surface, often raise surface temperatures significantly enough to incite sustained surface melting [Bennartz et al., 2013]. During AWARE in January 2016, Nicolas et al. [2017] suggested it was possible that this type of cloud presence in Antarctica could drive surface melt as it does in Greenland, even though optically thick clouds were the main cause of melt observed at the time of AWARE [Nicolas et al., 2017]. At Siple Dome in January 2015 and at Pine Island Glacier and Thwaites Glacier in January 2012, there is evidence that the melt in both cases may be driven by optically thin, liquid, low-lying clouds heating the surface. Cloud *LWP* values between 10 and 50 gm^{-2} indicate thin, liquid water cloud presence. In the Siple Dome case, just

before the melt on the 4th of January, the *LWP* from CERES increases to almost 50 gm^{-2} but mostly remains between 10 and 50 gm^{-2} for the extent of the melt. These clouds aided in increasing the LW radiation while simultaneously allowing SW radiation to raise surface temperatures to further incite melt. Since climate models often underrepresent and under-predict optically thin liquid clouds [Cesana et al., 2012], it is important to improve the resolution and microphysics of these models to accurately represent cloud presence in the Antarctic.

4.3 Surface Melt Preconditioning from Sensible Heat Flux

Siple Dome in December 2011 saw a large increase in sensible heat flux just before the surface melt event. The meteorological synopsis of the region supports this, as the airmass sitting over the Amundsen Sea Embayment was subsequently funneled inland and over Siple Dome and the Ross Ice Shelf, potentially drying the air through descent. An increase in skin temperature just before the melt event occurs as the sensible heat flux rises. The clear diurnal cycles shown in Figure 3.16 indicate that it would be difficult for any cloud presence to incite enough all-wave radiative enhancement or thermal blanketing in the region to result in surface melt. We therefore conclude that the positive impulse of sensible heat flux beginning 20-21 December preconditions the surface for a subsequent rise in emissivity and possible melt detection several days later.

4.4 Föhn Winds

By combining both ERA5 reanalysis data with satellite data from CERES, we have attempted to identify and isolate two suspected föhn wind events over the Ross Ice Shelf at the base of the Transantarctic Mountains, and on the LCIS. In both cases, wind speeds increased just

at the start of the melt event or just prior and the winds originated from the opposite side of the mountain range. Cloud *LWP* and *IWP* were generally low and varying at the times of melt, indicating a small and changing cloud presence which agrees with typical dry, warm air and clear sky conditions typical of föhn wind events.

Tom and Sabrina AWS sit at the base of the Transantarctic Mountains on the Ross Ice Shelf (Figure 1.4) and recorded a large rise in 2 m temperature along with a distinct change in wind speed and direction. Southeastern originating winds reached up to over 15 ms^{-1} just before the recorded T_b indicated melt. These observations agree with the synoptic analysis of the region discussed in Chapter 3.1.5. The large warm airmass that sat over the Amundsen Sea Embayment and the coastal WAIS and resulted in thermal blanketing at Pine Island Glacier and Thwaites Glacier, descended inland over the Siple Coast. This air was funneled over the southern Ross Ice Shelf, drying the region and resulting in an additional föhn wind drying effect.

The slight decrease in net SW and increase in net LW indicated there is a contribution to the changing SEB from cloud presence, perhaps on the borderline between thin cloud all-wave effect and thermal blanketing by optically thick clouds. Large positive impulses in latent heat flux are consistent with warm air just above the surface. The surface emissivity remains consistent with a mostly dry surface throughout the month until 22 December, and then between 23-24 December rises to values consistent with wet surface and PMW melt detection. This is another example where the PMW melt detection signal lags an impulse of positive sensible heat flux.

During summer months, melt on the LCIS is often observed increasing with volume, intensity, and extent as you travel north and west [King et al., 2017]. High quantities of melt on the western portion of the LCIS are indicative of these dry winds descending on the ice surface

and increasing near-surface temperatures. AWS-14 (located on the northwestern part of the LCIS; Figure 1.5) recorded elevated surface temperatures throughout most of the month with a slightly more significant peak during the melt event in question. It also recorded an increase in wind speed to 8 ms^{-1} with a shift in wind direction to northwesterly. These measurements coincide with ERA5 wind and temperature observations, and support the suggestion of föhn wind presence. Elevated surface temperatures in concurrence with this wind and lack of sustained cloud presence gives evidence for the cause of this melting to be föhn winds traversing the ice surface and driving temperatures up. In addition to this, distribution of T_b in this December 2000 case is consistent with conclusions from King et al. [2017]. On the LCIS, it is often difficult to isolate melt events driven by föhn wind events due to the high volume of melt that occurs during the months of December and January. With consistent surface melting on the ice shelf, it can be problematic to distinguish the drivers. Because these föhn wind events are so difficult to identify without direct observation, a wider spread of higher resolution data is needed to analyze surface and atmospheric conditions surrounding them.

Chapter 5

Conclusions

This study has investigated several cases of surface melt under climatologically typical conditions on the WAIS. Our results show that several days of melt can be induced by a variety of mechanisms whenever certain typical summertime meteorological conditions occur that elevate the total *ME*. A common factor among all the cases is a *ME* that remains positive through at least two diurnal cycles, either during or just outside the time interval when satellite PMW detects elevated surface T_b consistent with melt onset.

We identified two cases during which optically thick clouds created a thermal blanketing effect that induced surface melt. These clouds radiated essentially as blackbodies near the surface, bringing the net LW flux close to zero while attenuating the net SW flux. Extended periods of positive *ME* were the result of the combination between the total radiative flux and the mostly positive net turbulent fluxes. Also recognized were two cases in which the clouds were optically thinner, with *LWP* less than 50 gm^{-2}. These are potential examples of the all-wave radiative enhancement mechanism of Bennartz et al. [2013]. The thin liquid clouds cause substantial warming of the surface and drive the net LW flux up to around -25 Wm^{-2}, while allowing enough SW radiation to reach the surface such that the net SW flux is well above 50 Wm^{-2} at maximum solar elevation. This scenario can lead to sustained periods of positive *ME*.

In two other cases we identified a contribution of positive sensible heat flux to the surface melt that acted independently of the cloud radiative effects. Independently, elevated sensible heat flux does not appear to increase the surface emissivity as rapidly or as effectively as the cloud radiative effects. But strong impulses of sensible heat flux can either precondition an Antarctic snow surface toward melt onset or extend a melt period. We also discovered a föhn wind effect on the Ross Ice Shelf, demonstrating that this alternative mechanism for inducing surface melt can be detected in reanalysis data combined with satellite remote sensing. In addition to looking at föhn wind effects on the Ross Ice Shelf, we looked at a possible föhn wind event on the LCIS to observe the effects of these wind patterns on a larger scale, but conclusions with this case are not as conclusive because of the sheer amount of melt present that lasted throughout that month.

This study also highlights the need for various improvements in the methods and data sets used to quantify the time variation and climatology of surface melt throughout West Antarctica. The ERA5 reanalysis contains one of the most sophisticated cloud physics parameterizations used with numerical weather prediction models, but frequently and episodically underpredicts cloud *LWP* and hence surface LW radiation, while often making spuriously large estimates of cloud *IWP*. Hines et al. [2019] show that double-moment cloud microphysical parameterizations of the type used in global climate models improve the simulation of *LWP* over the WAIS. Future studies should perhaps adopt this more rigorous cloud physics. The NASA A-Train cloud property retrievals are more reliable than ERA5 at identifying cloud presence during melt events, and are likely more realistic than ERA5 in their estimates of *LWP*. However, like ERA5, their *IWP* estimates may be occasionally too large. The datasets used in these case studies are adequate enough to confidently identify changes in SEB components that can lead to extended positive *ME* and surface melt onset, but more accuracy and reliability, as well as higher

resolution data, would allow great improvements in long-term climatological analysis throughout Antarctica.

Finally, examination of individual grid cells corresponding to different T_b percentiles within a region shows that small-scale variability can have a noticeable impact on satellite remote sensing evaluation of surface melt. We generally find that the radiative fluxes related to clouds are spatially uniform over each of the case study regions. Surface emissivity tends to be spatially uniform outside of melt events in areas such as Siple Dome, which sits at a higher altitude on the WAIS than other case study sites. Of greatest interest to sea level rise are the Pine Island and Thwaites Glaciers, whose surface emissivity has considerable spatial variability both outside and during melt events. A prior melt event or localized precipitation might have altered the surface morphology before any given melt event is detected and analyzed. Results of this study therefore suggest that when investigating surface melt, and its potential for hydrofracturing, over the most vulnerable WAIS ice shelves, the highest available spatial resolution should be considered.

The need for improved data precision and dependability over polar regions becomes more pronounced, particularly in regions where direct observations are sparse, when looking to apply this information to improve the accuracy of global climate models. It is with these improvements that more concrete conclusions can be made about the drivers of surface melt in Antarctica. Looking forward, it is important to understand surface melt to determine whether its occurrence is increasing, and therefore if global sea level rise will begin to see more of an impact from it.

Bibliography

[Banwell et al., 2013] Banwell, A. F., MacAyeal, D. R., & Sergienko, O. V. (2013). Breakup of the Larsen B Ice Shelf triggered by chain reaction drainage of supraglacial lakes. *Geophysical Research Letters*, *40*(22), 5872–5876. https://doi.org/10.1002/2013GL057694

[Bennartz et al., 2013] Bennartz, R., Shupe, M. D., Turner, D. D., Walden, V. P., Steffen, K., Cox, C. J., Kulie, M. S., Miller, N. B., & Pettersen, C. (2013). July 2012 Greenland melt extent enhanced by low-level liquid clouds. *Nature*, *496*(7443), 83–86. https://doi.org/10.1038/nature12002

[Brodzik et al., 2016] Brodzik, M. J., D. G. Long, M. A. Hardman, A. Paget, and R. Armstrong. 2016, Updated 2018. *MEaSUREs Calibrated Enhanced-Resolution Passive Microwave Daily EASE-Grid 2.0 Brightness Temperature ESDR, Version 1*. [April to March 1999 to 2016]. Boulder, Colorado USA. NASA National Snow and Ice Data Center Distributed Active Archive Center. doi: https://doi.org/10.5067/MEASURES/CRYOSPHERE/NSIDC 0630.001. [October 10, 2019].

[Bromwich et al., 2004] Bromwich, D. H., Monaghan, A. J., & Guo, Z. (2004). Modeling the ENSO Modulation of Antarctic Climate in the Late 1990s with the Polar MM5. *Journal of Climate*, *17*(1), 109–132. https://doi.org/10.1175/1520-0442(2004)017<0109:MTEMOA>2.0.CO;2

[Bromwich et al., 2012] Bromwich, D. H., Nicolas, J. P., Hines, K. M., Kay, J. E., Key, E. L., Lazzara, M. A., Lubin, D., McFarquhar, G. M., Gorodetskaya, I. V, Grosvenor, D. P., Lachlan-Cope, T., & van Lipzig, N. P. M. (2012). *Tropospheric clouds in Antarctica - Bromwich - 2012 - Reviews of Geophysics - Wiley Online Library*. *50*(1), RG1004. https://doi.org/10.1029/2011RG000363.1.INTRODUCTION

[Cai et al., 2014] Cai, W. et al. Increasing frequency of extreme El Niño events due to greenhouse warming. *Nat. Clim. Change* **4**, 111–116 (2014).

[Cape et al., 2015] Cape, M. R., Vernet, M., Skvarca, P., Marinsek, S., Scambos, T., & Domack, E. (2015). Foehn winds link climate-driven warming to ice shelf evolution in Antarctica. *Journal of Geophysical Research*, *120*(21), 11,037-11,057. https://doi.org/10.1002/2015JD023465

[Cesana et al., 2012] Cesana, G., Kay, J. E., Chepfer, H., English, J. M., & De Boer, G. (2012). Ubiquitous low-level liquid-containing Arctic clouds: New observations and climate model constraints from CALIPSO-GOCCP. *Geophysical Research Letters*, *39*(20), 1–6. https://doi.org/10.1029/2012GL053385

[Christianson et al., 2016] Christianson, K., Bushuk, M., Dutrieux, P., Parizek, B. R., Joughin, I. R., Alley, R. B., Shean, D. E., Abrahamsen, E. P., Anandakrishnan, S., Heywood, K. J., Kim, T. W., Lee, S. H., Nicholls, K., Stanton, T., Truffer, M., Webber, B. G. M., Jenkins, A., Jacobs, S., Bindschadler, R., & Holland, D. M. (2016). Sensitivity of Pine Island Glacier to observed ocean forcing. *Geophysical Research Letters*, *43*(20), 10,817-10,825. https://doi.org/10.1002/2016GL070500

[DeConto and Pollard, 2016] DeConto, R.M., Pollard, D., 2016. Contribution of Antarctica to past and future sea-level rise. Nature 531 (7596), 591–597. http://dx.doi.org/10.1038/nature17145.

[Dee et al., 2011] Dee, D. P., Uppala, S. M., Simmons, A. J., Berrisford, P., Poli, P., Kobayashi, S., Andrae, U., Balmaseda, M. A., Balsamo, G., Bauer, P., Bechtold, P., Beljaars, A. C. M., van de Berg, L., Bidlot, J., Bormann, N., Delsol, C., Dragani, R., Fuentes, M., Geer, A. J., Haimberger, L., Healy, S., Hersbach, H., Hòlm, E., Isaksen, L., Kållberg, P., Köhler, M., Matricardi, M., Mcnally, A., Monge-Sanz, B., Morcrette, J., Park, B., Peubey, C., de Rosnay, P., Tavolato, C., Thépaut, J., Vitart, F. (2011). The ERA-Interim reanalysis: Configuration and performance of the data assimilation system. *Quarterly Journal of the Royal Meteorological Society*, *137*(656), 553–597. https://doi.org/10.1002/qj.828

[Ding et al, 2013] Ding, Q., and E. J. Steig (2013), Temperature change on the Antarctic Peninsula linked to the Tropical Pacific, J. Clim., 26(19), 7570–7585, doi:10.1175/JCLI-D-12-00729.1.

[Dupont et al., 2005] Dupont, T. K., & Alley, R. B. (2005). Assessment of the importance of ice-shelf buttressing to ice-sheet flow. *Geophysical Research Letters*, *32*(4), 1–4. https://doi.org/10.1029/2004GL022024

[ECMWF-IFS, 2008] ECMWF-IFS (2008). Part IV: Physical processes (CY33R1). Technical Report. European Centre for Medium-Range Weather Forecasts (ECMWF)

[Elvidge et al., 2015] Elvidge, A. D., Renfrew, I. A., King, J. C., Orr, A., Lachlan-Cope, T. A., Weeks, M., & Gray, S. L. (2015). Foehn jets over the Larsen C Ice Shelf, Antarctica. *Quarterly Journal of the Royal Meteorological Society*, *141*(688), 698–713. https://doi.org/10.1002/qj.2382

[Elvidge et al., 2016] Elvidge, A. D., Renfrew, I. A., King, J. C., Orr, A., & Lachlan-Cope, T. A. (2016). Foehn warming distributions in nonlinear and linear flow regimes: A focus on the Antarctic Peninsula. *Quarterly Journal of the Royal Meteorological Society*, *142*(695), 618–631. https://doi.org/10.1002/qj.2489

[Fisher et al., 2015] Fisher, A. T., Mankoff, K. D., Tulaczyk, S. M., Tyler, S. W., & Foley, N. (2015). High geothermal heat flux measured below the West Antarctic Ice Sheet. *Science Advances*, *1*(6), 1–9. https://doi.org/10.1126/sciadv.1500093

[Fogt et al., 2011] Fogt, R. L., Bromwich, D. H., & Hines, K. M. (2011). Erratum to: Understanding the SAM influence on the South Pacific ENSO teleconnection (Clim Dyn, (2011), 36, (1555-1576), 10.1007/s00382-010-0905-0). *Climate Dynamics*, *37*(9–10), 2127–2128. https://doi.org/10.1007/s00382-011-1201-3

[Fürst et al., 2016] Fürst, J. J., Durand, G., Gillet-Chaulet, F., Tavard, L., Rankl, M., Braun, M., & Gagliardini, O. (2016). The safety band of Antarctic ice shelves. *Nature Climate Change*, *6*(5), 479–482. https://doi.org/10.1038/nclimate2912

[Graeter et al., 2018] Graeter, K. A., Osterberg, E. C., Ferris, D. G., Hawley, R. L., Marshall, H. P., Lewis, G., Meehan, T., McCarthy, F., Overly, T., & Birkel, S. D. (2018). Ice Core Records of West Greenland Melt and Climate Forcing. *Geophysical Research Letters*, *45*(7), 3164–3172. https://doi.org/10.1002/2017GL076641

[Hines et al., 2019] Hines, K. M., Bromwich, D. H., Wang, S.-H., Silber, I., Verlinde, J., & Lubin, D. (2019). Microphysics of summer clouds in central West Antarctica simulated by the Polar Weather Research and Forecasting Model (WRF) and the Antarctic Mesoscale Prediction System (AMPS). *Atmos. Chem. Phys.*, *19*(19), 12431–12454. https://doi.org/10.5194/acp-19-12431-2019

[Hoffman et al., 2019] Hoffman, M. J., Asay-Davis, X., Price, S. F., Fyke, J., & Perego, M. (2019). Effect of Subshelf Melt Variability on Sea Level Rise Contribution From Thwaites Glacier, Antarctica. *Journal of Geophysical Research: Earth Surface*, *124*(12), 2798–2822. https://doi.org/10.1029/2019JF005155

[Hogg and Gudmundsson, 2017] Hogg, A. E., & Gudmundsson, G. H. (2017). Commentary: Impacts of the Larsen-C Ice Shelf calving event. *Nature Climate Change*, *7*(8), 540–542. https://doi.org/10.1038/nclimate3359

[Humphrey et al., 2012] Humphrey, N. F., Harper, J. T., & Pfeffer, W. T. (2012). Thermal tracking of meltwater retention in Greenland's accumulation area. *Journal of Geophysical Research: Earth Surface*, *117*(1), 1–11. https://doi.org/10.1029/2011JF002083

[King et al., 2017] King, J. C., Kirchgaessner, A., Bevan, S., Elvidge, A. D., Kuipers Munneke, P., Luckman, A., Orr, A., Renfrew, I. A., & van den Broeke, M. R. (2017). The Impact of Föhn Winds on Surface Energy Balance During the 2010–2011 Melt Season Over Larsen C Ice Shelf, Antarctica. *Journal of Geophysical Research: Atmospheres*, *122*(22), 12,062-12,076. https://doi.org/10.1002/2017JD026809

[Kingslake et al., 2017] Kingslake, J., Ely, J. C., Das, I., & Bell, R. E. (2017). Widespread movement of meltwater onto and across Antarctic ice shelves. *Nature*, *544*(7650), 349–352. https://doi.org/10.1038/nature22049

[Lazzara et al., 2012] Lazzara, M. A., Weidner, G. A., Keller, L. M., Thom, J. E., & Cassano, J. J. (2012). Antarctic automatic weather station program: 30 years of polar observations.

Bulletin of the American Meteorological Society, *93*(10), 1519–1537. https://doi.org/10.1175/BAMS-D-11-00015.1

[Nakayama et al., 2018] Nakayama, Y., Menemenlis, D., Zhang, H., Schodlok, M., & Rignot, E. (2018). Origin of Circumpolar Deep Water intruding onto the Amundsen and Bellingshausen Sea continental shelves. *Nature Communications*, *9*(1), 1–9. https://doi.org/10.1038/s41467-018-05813-1

[Nicolas et al., 2017] Nicolas, J. P., Vogelmann, A. M., Scott, R. C., Wilson, A. B., Cadeddu, M. P., Bromwich, D. H., Verlinde, J., Lubin, D., Russell, L. M., Jenkinson, C., Powers, H. H., Ryczek, M., Stone, G., & Wille, J. D. (2017). January 2016 extensive summer melt in West Antarctica favoured by strong El Niño. *Nature Communications*, *8*(May), 1–10. https://doi.org/10.1038/ncomms15799

[Paolo et al., 2018] Paolo, F.S., Padman, L., Fricker, H.A. *et al.* Response of Pacific-sector Antarctic ice shelves to the El Niño/Southern Oscillation. *Nature Geosci* **11,** 121–126 (2018). https://doi.org/10.1038/s41561-017-0033-0

[Paolo et al., 2015] Paolo, F. S., Fricker, H. A., & Padman, L. (2015). Volume loss from Antarctic ice shelves is accelerating. *Science*, *348*(6232), 327–331. https://doi.org/10.1126/science.aaa0940

[Phillips et al., 1998] Phillips, H. A. (1998). Surface meltstreams on the Amery Ice Shelf, East Antarctica. *Annals of Glaciology*, *27*, 177-181. https://doi.org/10.31.3189/1998AoG27-1-177-181

[Pollard et al., 2015] Pollard, D., DeConto, R. M., & Alley, R. B. (2015). Potential Antarctic Ice Sheet retreat driven by hydrofracturing and ice cliff failure. *Earth and Planetary Science Letters*, *412*, 112–121. https://doi.org/10.1016/j.epsl.2014.12.035

[Ridley, 1993] Ridley, J.K., Surface melting on Antarctic Peninsula ice shelves detected by passive microwave sensors, *Geophysical Research Letters*, 1993, *20*(23), 2638–2642. https://doi.org/10.1029/93GL02611

[Rignot et al., 2004] Rignot, E., Casassa, G., Gogineni, P., Krabill, W., Rivera, A., & Thomas, R. (2004). Accelerated ice discharge from the Antarctic Peninsula following the collapse of Larsen B ice shelf. *Geophysical Research Letters*, *31*(18), 2–5. https://doi.org/10.1029/2004GL020697

[Rignot et al., 2013] Rignot, E., Jacobs, S., Mouginot, J., & Scheuchl, B. (2013). Ice-shelf melting around Antarctica. *Science*, *341*(6143), 266–270. https://doi.org/10.1126/science.1235798

[Rott et al., 2002] Rott, H., Rack, W., Skvarca, P., & De Angelis, H. (2002). Northern Larsen Ice Shelf, Antarctica: Further retreat after collapse. *Annals of Glaciology*, *34*, 277–282. https://doi.org/10.3189/172756402781817716

[Scambos et al., 2000] Scambos, T. A., Hulbe, C., Fahnestock, M., & Bohlander, J. (2000). The link between climate warming and break-up of ice shelves in the Antarctic Peninsula. *Journal of Glaciology*, *46*(154), 516–530. https://doi.org/10.3189/172756500781833043

[Scambos et al., 2004] Scambos, T. A., Bohlander, J. A., Shuman, C. A., & Skvarca, P. (2004). Glacier acceleration and thinning after ice shelf collapse in the Larsen B embayment, Antarctica. *Geophysical Research Letters*, *31*(18), 2001–2004. https://doi.org/10.1029/2004GL020670

[Scambos et al., 2007] Scambos, T. A., Haran, T. M., Fahnestock, M. A., Painter, T. H., & Bohlander, J. (2007). MODIS-based Mosaic of Antarctica (MOA) data sets: Continent-wide surface morphology and snow grain size. *Remote Sensing of Environment*, *111*(2-3), 242-257.

[Scambos et al., 2017] Scambos, T. A., Bell, R. E., Alley, R. B., Anandakrishnan, S., Bromwich, D. H., Brunt, K., Christianson, K., Creyts, T., Das, S. B., DeConto, R., Dutrieux, P., Fricker, H. A., Holland, D., MacGregor, J., Medley, B., Nicolas, J. P., Pollard, D., Siegfried, M. R., Smith, A. M., Steig, E.J., Trusel, L.D., Vaughn, D.G., Yager, P. L. (2017). How much, how fast?: A science review and outlook for research on the instability of Antarctica's Thwaites Glacier in the 21st century. *Global and Planetary Change*, *153*(November 2016), 16–34. https://doi.org/10.1016/j.gloplacha.2017.04.008

[Scott et al., 2019] Scott, R. C., Nicolas, J. P., Bromwich, D. H., Norris, J. R., & Lubin, D. (2019). Meteorological drivers and large-scale climate forcing of West Antarctic surface melt. *Journal of Climate*, *32*(3), 665–684. https://doi.org/10.1175/JCLI-D-18-0233.1

[Scott and Lubin, 2016] Scott, R. C., & Lubin, D. (2016). Unique manifestations of mixed-phase cloud microphysics over Ross Island and the Ross Ice Shelf, Antarctica. *Geophysical Research Letters*, *43*(6), 2936–2945. https://doi.org/10.1002/2015GL067246

[Shepherd et al., 2012] Shepherd, A., & Ivins, E. (2012). Review research articles. *Science*, *338*(November), 1183–1190. https://doi.org/5b0143 [pii]

[Smith et al., 2020] Smith, B., Fricker, H. A., Gardner, A. S., Medley, B., Nilsson, J., Paolo, F. S., Holschuh, N., Adusumilli, S., Brunt, K., Csatho, B., Harbeck, K., Markus, T., Neumann, T., Siegfried, M. R., & Zwally, H. J. (2020). Pervasive ice sheet mass loss reflects competing ocean and atmosphere processes. *The American Journal of Physiology*, *275*(275), 1092. https://doi.org/10.220.32.247

[Tedesco, 2009] Tedesco, M. (2009). Assessment and development of snowmelt retrieval algorithms over Antarctica from K-band spaceborne brightness temperature (1979-2008). *Remote Sensing of Environment*, *113*(5), 979–997. https://doi.org/10.1016/j.rse.2009.01.009

[Thomas et al., 1979] Thomas, R. H., Sanderson, T. J. O. & Rose, K. E. (1979). Effect of climatic warming on the West Antarctic ice sheet. *Nature* 277, 355–358.

[Trusel et al., 2018] Trusel, L. D., Das, S. B., Osman, M. B., Evans, M. J., Smith, B. E., Fettweis, X., McConnell, J. R., Noël, B. P. Y., & van den Broeke, M. R. (2018). Nonlinear rise in Greenland runoff in response to post-industrial Arctic warming. *Nature*, *564*(7734), 104–108. https://doi.org/10.1038/s41586-018-0752-4

[Turner et al., 2016] Turner, J., Lu, H., White, I., King, John C., Phillips, T., Hosking, J. S., Bracegirdle, T. J., Marshall, G. J., Mulvaney, R., Deb, P. (2016). Absence of 21st century warming on Antarctic Peninsula consistent with natural variability. *Nature* **535,** 411–415. https://doi.org/10.1038/nature18645

[Van Tricht et al., 2016] Van Tricht, K., Lhermitte, S., Lenaerts, J. T. M., Gorodetskaya, I. V., L'Ecuyer, T. S., Noël, B., Van Den Broeke, M. R., Turner, D. D., & Van Lipzig, N. P. M. (2016). Clouds enhance Greenland ice sheet meltwater runoff. *Nature Communications*, *7*(May 2015). https://doi.org/10.1038/ncomms10266

[van den Broeke, 2005] van den Broeke, M. (2005). Strong surface melting preceded collapse of Antarctic Peninsula ice shelf. *Geophysical Research Letters*, *32*(12), 1–4. https://doi.org/10.1029/2005GL023247

[Wille et al., 2019] Wille, J., Favier, V., Dufour, A., Gorodetskaya, I., Turner, J., Agosta, C., & Codron, F. (2019). West Antarctic surface melt triggered by atmospheric rivers. *Nature Geoscience*, *12*. https://doi.org/10.1038/s41561-019-0460-1

[Zwally and Fiegles ,1994] Zwally, H. J., & Fiegles, S. (1994). Extent and duration of Antarctic surface melting. *Journal of Glaciology*, *40*(136), 463–476. https://doi.org/10.3189/s0022143000012338

[Zwally and Gloerson, 1977] Zwally, H.J. and P. Gloerson, 1977. "Passive Microwave Images of the Polar Regions and Research Applications," *Polar Record. 18*(116), 431-450. https://doi.org/10.1017/S0032247400000930